MAPPING EVAPOTRANSPIRATION TO DISAGGREGATE EDDY-COVARIANCE FOOTPRINTS

A thesis submitted to the College of Graduate and Postdoctoral studies

in partial fulfillment of the requirements

for the degree of Master of Science

in the Department of Civil, Geological,

and Environmental Engineering

University of Saskatchewan

Saskatoon, SK, Canada

By

ANDERS HUNTER

PERMISSION TO USE

In presenting this thesis in partial fulfillment of the requirements for a Postgraduate degree from the University of Saskatchewan, I agree that the Libraries of this University may make it freely available for inspection. I further agree that permission for copying of this thesis in any manner, in whole or in part, for scholarly purposes may be granted by the professor or professors who supervised my thesis work or, in their absence, by the Head of the Department or the Dean of the College in which my thesis work was done. It is understood that any copying or publication or use of this thesis or parts thereof for financial gain shall not be allowed without my written permission. It is also understood that due recognition shall be given to me and to the University of Saskatchewan in any scholarly use that may be made of any material in my thesis. Requests for permission to copy or to make other uses of materials in this thesis, in whole or part, should be addressed to:

Dean, College of Graduate and Postdoctoral Studies
University of Saskatchewan
116 Thorvaldson Building, 110 Science Place
Saskatoon, Saskatchewan Canada
S7N 5C9

Head, Department of Civil, Geological, and Environmental Engineering
University of Saskatchewan
51 Campus Dr.
Saskatoon, SK
Canada, S7N 5A

DISCLAIMER

Reference in this thesis to any specific commercial product, process, or service by trade name, trademark, manufacturer, or otherwise, does not constitute or imply its endorsement, recommendation, or favouring by the University of Saskatchewan. The views and opinions of the author expressed herein do not state or reflect those of the University of Saskatchewan and shall not be used for advertising or product endorsement purposes.

ABSTRACT

Land-atmosphere interactions are commonly quantified using eddy-covariance (EC) equipment. This technique provides fluxes which are attributed to an area-averaged two-dimensional flux footprint. Although source flux heterogeneity is present within these footprints, current EC footprint models are unable to distinguish the variable flux contributions (although they are incorporated into the bulk EC flux). A disaggregation method would increase the value of EC data by allowing users to isolate individual fluxes from features within the flux footprint; furthermore, this may extend the useability of the EC method to more complex terrain of mixed land classifications. It remains unexplored how high-resolution surface energy balance (SEB) models can be used to disaggregate these EC footprints. This thesis presents a SEB workflow using Unoccupied Aerial Vehicles (UAVs) to generate high-resolution patterns of evapotranspiration (ET) to disaggregate EC footprints in a novel disaggregated flux footprint prediction (disFFP) method.

This workflow begins by using novel UAV Light Ranging And Detection (LiDAR) techniques to derive detailed maps of canopy height (h), effective leaf area index (LAI_e), and canopy viewing fraction (f_c), consistent with known vegetation patterns and field-average observations ($LAI_e\ RMSE = 0.08 - 0.81\ m^2 m^{-2}$). It then follows an atmospheric correction (path transmissivity and upward-welling radiance) and an ensemble emissivity adjustment (brightness to radiometric temperature), testing these with UAV thermal data to determine their absolute (magnitude) and relative (spatial pattern) effects on temperature. A modified t-test - considering autocorrelation - showed that a raw brightness temperature has similar spatial patterns ($r > .99$, $p_{val} \gg 0.001$) to brightness and radiometric temperatures. Combining these thermal and LiDAR UAV inputs with a high-resolution SEB model (HRMET), the model performance was then compared against EC fluxes. It followed that HRMET tended to overestimate latent heat over full canopies when surface-air temperature differences exceed $4 - 5°C$. Overall, HRMET succeeded at replicating EC latent heat flux within $RMSE$ of $79 - 136\ W\ m^{-2}$ using raw brightness and ensemble emissivity corrected (observed radiometric) temperatures. The resultant relative ET maps (ET_R) provided a coherent chronology of the changing flux landscape. Furthermore, the ET_R trials using corrected temperatures (brightness, radiometric, and observed radiometric) had similar spatial patterns to those found using just raw brightness

temperature ($r > .93$, $p_{val} \gg 0.001$). This implies that a raw brightness temperature is sufficient for determining relative patterns of evapotranspiration.

The next part of the workflow uses ET_R to disaggregate a well-known parameterization of a backwards-Lagrangian flux footprint model. The proposed disaggregation method (disFFP) uses the concept of ET period to describe an interval of time (day scale) where the EC flux environment remains relatively constant (constant-rate cumulative ET rate). ET periods were determined using a piece-wise regression of the cumulative day-over-day EC latent flux rate. Each season was divided into five ET periods and compared with the two other seasons to discover potential metrics for further classifying ET periods. It was found that ET rates were consistent across comparable ET periods, $2 - 38\,\%$ (standard deviation as a percentage of sample mean), and that additional metrics (plant phenology, growing degree day, standard precipitation index) played an important role in characterizing ET periods for inter-seasonal work. Eddy-covariance and UAV data were coupled using climatology footprints of ET periods and the coinciding ET patterns (ET_R and coefficient of variation). The disFFP combination of these two products (footprint-weighted factoring) provided disaggregated footprints (EC bulk ET of $144\,mm$) that reflected increased contributions ($180 - 200\,mm$) over high ET areas and diminished values ($90 - 100\,mm$) over lower ET areas. These preliminary findings present an exciting new opportunity to connect discrete UAV data with continuous EC flux monitoring.

ACKNOWLEDGMENTS

This research was supported by the Agricultural Water Futures project of the Global Water Futures Program, funded by the Canada First Research Excellence Fund. We also thank our field supports for their integral contributions: Bruce Johnson, Alistair Wallace, Dong Zhao, Erika Beaumann, Bosse, and Eddie Lyu.

TABLE OF CONTENTS

LIST OF TABLES

LIST OF FIGURES

LIST OF ABBREVIATIONS

Acronym	Meaning
ASL	Atmospheric Surface Layer
ABL	Atmospheric Boundary LAYER
disFFP	Disaggregated Flux Footprint Prediction
EC	Eddy-Covariance
ER	Environmental Respiration
ET	EvapoTranspiration
ET_R	Relative EvapoTranspiration
EVI	Enhanced Vegetation Index
FFP	Flux Footprint Prediction
GPP	Gross Primary Production
HRMET	High-Resolution Mapping of EvapoTranspiration
LAI	Leaf Area Index
LCC	Land Classification Characterization
LiDAR	Light Detection and Ranging
NDVI	Normalized Difference Vegetation Index
NEE	Net Ecosystem Exchange (CO_2)
OS	One Source Model
PAR	Photosynthetically Active Radiation
SEB	Surface Energy Balance
SEBAL	Surface Energy Balance Algorithm for Land
SVAT	Soil-Vegetation-Atmosphere-Transfer model
TS	Two Source Energy Balance
UAV	Unoccupied Aerial Vehicle

LIST OF VARIABLES

Variable	Meaning
κ_c	Canopy extinction coefficient
Φ	Field of view
θ	disFFP scaling fraction for LE and ET allocation
ψ_h	atmospheric stability correction for sensible heat
ψ_m	atmospheric stability correction for momentum
ζ	Atmospheric stability
σ	Stefan-Boltzmann constant
χ_f	Footprint-weighted bulk SEB component value
$\chi_{i,j}$	SEB component value at pixel level
a	Area of pixel
c	Speed of light
C_s	Soil thermal conductivity
cv_{ET}	Coefficient of variation for spatial ET(remote sensing SEB model)
$ET_{R_{i,j}}$	Relative evapotranspiration values at pixel level
ET_e	Effective evapotranspiration
$\widehat{ET}$	Eddy-covariance bulk evapotranspiration
f	Disaggregated footprint values (as fraction of footprint domain sum)
f_c	Canopy viewing fraction
$F_{i,j}$	Footprint function value at pixel level
F_D	Disaggregated footprint values
$F_{D_{i,j}}$	Disaggregated footprint values at pixel level
G	Soil heat flux
G_{obs}	Soil heat flux from heat flux plate (at depth)
H	Sensible heat flux
h	Canopy height model
h_P	Planck's constant
k_B	Boltzmann constant
LAI_e	Effective LAI (Beers-lambert approach)
$\widehat{LE}$	Eddy-covariance bulk latent heat flux
$LE_{i,j}$	Landscape latent heat flux at pixel level
L_B	Apparent target surface radiance (or spectral radiance)
L_D	Reflected radiance (or spectral radiance) off of target surface
L_U	Upwelling radiance (or spectral radiance) from the atmosphere
n_g	Number of ground-classified points
n_c	Number of canopy-classified points
r_{ah}	Aerodynamic resistance of sensible heat
r_{am}	Aerodynamic resistance of momentum
R_n	Net radiation
r_s	Soil roughness resistance
RES	Residual (unaccounted for) energy
R_s	Sensor radiance
R_u	Upward solar irradiance
T	Temperature
T_g	Actual targe surface temperature
T_{ah}	Aerodynamic temperature of sensible heat
T_{air}	Air temperature
τ	Transmissivity
$T_{B,obs}$	Observed brightness temperature
T_B	Brightness temperature (atmosphere corrected)
$T_{R,obs}$	Observed target radiometric temperature ($\epsilon_{ensemble}$ corrected)
T_R	Target radiometric temperature ($\epsilon_{ensemble}$ & atmosphere corrected)
T_c	Canopy temperature
T_s	Soil temperature
T_{sky}	Sky temperature
$\bar{q}$	Mean vertical H20 flux
$\overline{q'w'}$	Net average H2O covariance
$\bar{u}$	Mean streamwise windspeed
u'	Instantaneous streamwise windspeed
u_*	Friction velocity
$\overline{\mathrm{u'w'}}$	Net average wind covariance

Table continued next page…

…table continued	
$\bar{w}$	Mean vertical wind speed
w′	Instantaneous vertical windspeed
z_{0h}	Roughness length of sensible heat
z_{0m}	Roughness length of momentum
z_T	Air temperature measurement height
Z_u	Wind speed measuring height
z_{soil}	Soil depth

LIST OF STATISTICAL ABBREVIATIONS

Statistic	Meaning
$RMSE$	Root mean squared error
R^2	Coefficient of determination as explained variance
R^2_{adj}	Adjusted coefficient of determination as explained variance
R^2_{fit}	Goodness-of-fit with $1:1$ line (as explained variance)
r	Pearson correlation coefficient*
r^2	Squared Pearson correlation coefficient*
n_{mod}	Modified number of observations (modified t-test)
p	p-value significance of r
SD	Standard deviation
$bias$	Mean measurement bias
u_{Total}	Combined instrument and measurement uncertainty
$u_{instrument}$	Instrument uncertainty (calibration)
$u_{measurement}$	Measurement uncertainty (two times spatial or temporal SD)

* Effect of r changes depending on whether a modified t-test is used (autocorrelation corrected)

1 INTRODUCTION

1.1 Background

Quantifying land surface-atmosphere exchanges is an ongoing challenge for environmental scientists and meteorologists alike. The prominent method of eddy-covariance (EC) directly measures water vapour flux (represented using latent heat or evapotranspiration) as an area-averaged bulk value over a modelled footprint (fetch of land surface contributing to the bulk measurement). Although robust two-dimensional footprint models are available, they do not partition flux among surface source heterogeneity (Kljun et al. 2015). Variations in source strength - as it relates to water vapour flux - are caused primarily by differences in available soil moisture.

The conspicuous rise of unoccupied aerial vehicles (UAV) and subsequent developments in remote sensing now present new opportunities (Kustas and Anderson 2009, Hoffmann et al. 2016, Nieto et al. 2019, Nocco et al. 2019). Thermal remote sensing imagery can produce high-resolution evapotranspiration (ET) maps and reveal underlying landscape hydrology traits (Zipper and Loheide II 2014). Effectively, these methods apply a surface energy balance (SEB) with ground-based estimates of soil heat flux and net radiation and a thermal-derived sensible heat to solve latent heat (spatially-variable) as a residual.

It follows that UAV surface energy balance methods can also be applied to disaggregate EC flux footprints and quantify contributions from source surface features. In this thesis paper, we propose a disFFP disaggregation method involving the High-Resolution Mapping of EvapoTranspiration (HRMET) model (Zipper and Loheide II 2014) and the Kljun et al. (2015) footprint parameterization (FFP).

1.2 Research objectives

Our primary goal is to disaggregate EC flux footprints using high-resolution ET patterns from a UAV-driven surface energy balance. Achieving this objective requires a two-step approach. First, we proposed validating the selected SEB model - HRMET - with EC flux measurements. Alongside this, we investigate using UAV Light Detection And Ranging (LiDAR) methods to acquire canopy height, viewing factor, and leaf area index. We also sought to establish whether an easy-to-measure raw brightness temperature can capture ET patterns similar to those of a corrected temperature. In this first step, we are primarily concerned about preserving HRMET's

spatial authenticity to acquire relative evapotranspiration patterns (ET_R). This leads us to the second step of using ET_R to disaggregate EC footprints. In this step, we want to know how our disaggregation strategy (disFFP) performs on single footprints, seasonal climatologies, and multi-seasonal periods.

1.3 Organization of thesis

This thesis is presented in manuscript style and is composed of six sections. Section one (current section) contained a brief introduction of the topic, a statement of research objectives, and the present thesis organization overview. This is followed by a literature review section explaining the key principles of UAV surface energy balance models and the EC method. Afterwards, I present my first manuscript titled *Assessing a high-resolution evapotranspiration model for field crops*. Section four proceeds with my second manuscript titled *Disaggregating eddy-covariance footprints using UAV evapotranspiration patterns*. Lastly, I combine the findings of sections three and four into a synthesis report and thesis conclusion.

2 LITERATURE REVIEW

2.1 Thermal remote sensing energy balance

A SEB balance follows the energy exchanges across a surface. Net radiation from the sun (R_n) increases surface temperature and transfers this energy to the atmosphere as sensible heat (H), evaporates and transpires water as latent heat (LE), and is conducted into the ground through soil heat flux (G). Advection (A) is the horizontal movement of energy from hot to cold surfaces. Figure 1 demonstrates these interactions over a hypothetical land surface with no energy storage. It is a common simplification to exclude A in land surface and footprint models (Bastiaanssen et al. 1998a, Kljun et al. 2015). Although some studies have shown that this term is pertinent in arid dryland environments (Alfieri et al. 2012, Song et al. 2016a), the present study uses the simplified energy balance of [1].

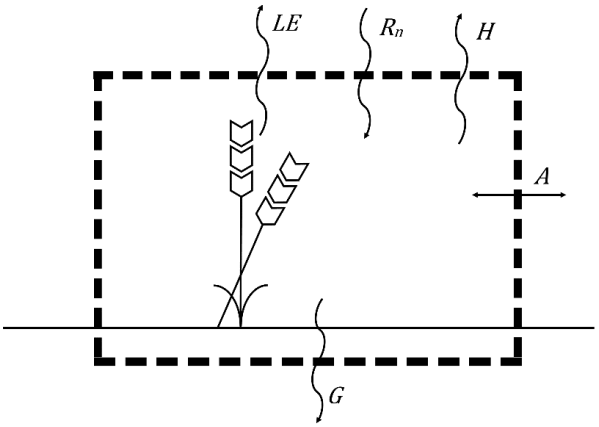

Figure 1. Surface energy balance over a cropped surface without energy storage

[1] $$R_n - G = H + LE$$

Surface energy balance models use empirical and analytical methods to solve [1] and are often applied in conjunction with thermal remote sensing (Kustas and Anderson 2009). For example, the two-source models developed by Norman et al. (1995) and Kustas and Norman (1999) partition R_n between canopy and soil using a fractional canopy cover term based on LAI and a clumping factor. Soil heat fluxes are approximated as a proportion of R_n, and H and LE are calculated based on temperature and water vapour pressure gradients, respectively. Common with other SEB models, thermal remote sensing is used to calculate H and then solve LE as a residual (Bastiaanssen et al. 1998b, Kustas and Norman 1999, Zipper and Loheide II 2014).

Equation [2] shows the general solution for H given an aerodynamic surface temperature (T_{ah}), air temperature (T_{air}), heat capacity (c_p), moist air density (ρ_a), and a parallel arrangement resistance term (Figure 2).

[2] $$H = \frac{\rho_a c_p (T_{ah} - T_{air})}{r_{ah}}$$

The aerodynamic resistance of sensible heat (r_{ah}) is founded on atmospheric boundary layer theory (Section 2.3) and is presented from Kustas and Norman (1999) in [3]. It includes measurement heights for wind speed (z_u) and air temperature (z_T), a canopy displacement height (d), the von Karman constant ($\kappa \approx 0.4$), stability correction terms for momentum (ψ_m) and sensible heat (ψ_h), and also roughness lengths for heat and momentum (z_{0h} and z_{0m}, respectively).

[3] $$r_{ah} = \frac{\left(ln\left(\frac{z_u - d}{z_{0m}}\right) - \psi_m\right)\left(ln\left(\frac{z_T - d}{z_{0h}}\right) - \psi_h\right)}{k^2 u}$$

Roughness lengths z_{0h} and z_{0m} are logarithmically related using the kB^- parameter in [4]. A constant kB^- value of 2.3 ($z_{0h} \approx 0.1\, z_{0m}$) is widely used (Allen et al. 1998, Bastiaanssen et al. 1998a); however, kB^- is known to vary with time and over heterogenous terrain (Su et al. 2001, Paul et al. 2014). Although z_{0m} is often crudely estimated from crop height, better parameterizations exist based on LAI and nominal surface roughness values (Raupach 1994).

[4] $$kB^- = ln\frac{z_{0m}}{z_{0h}}$$

The definition of T_{ah} is purely theoretical: a temperature at which [2] is satisfied (Norman and Becker 1995). However, it also represents a surrogate for thermodynamic temperature, the average of soil (T_s) and canopy (T_c) temperatures when in perfect kinematic equilibrium (Figure 2). A momentum-based aerodynamic resistance term (r_{am}) is used in place of the sensible heat interpretation. An additional surface resistance term r_s is also needed to account for drag forces exhibited by the bare-soil roughness when T_c and T_s are used in place of T_{ah}. Models using these two interpretations are referred to as one-source (OS) or two-source (TS) according to whether they use T_{ah} or T_c and T_s, respectively.

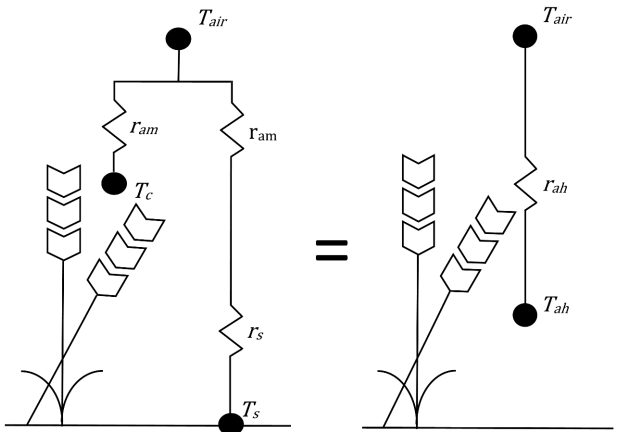

Figure 2. A parallel arrangement of resistors based on (Norman et al. 1995).

Variables T_c, T_s, and T_{air} are thermodynamic temperatures for canopy, soil, and air, respectively. These are related using a momentum resistance (r_{am}) and the soil drag resistance (r_s). Temperature T_{ah} is an aerodynamic term associated with the resistance to heat flow (r_{ah}).

A virtue of the TS approach is that it partitions remotely sensed brightness temperature (T_B) into T_c and T_s and solves the sensible heat exchange over each separately. Conversely, the HRMET model (used in this study) does not perform this step so is not a true TS model. HRMET was developed by Zipper and Loheide (2014) as an offshoot of Norman et al.'s TS model (1995) and Bastiaanssen et al.'s (1998a) single-source SEBAL (Surface Energy Balance Algorithm for Land). HRMET is a hybrid approach using TS R_n partitioning with an OS resistance scheme for calculating bulk H flux. It iteratively finds H by adjusting atmospheric stability (ζ) and solving the bulk transfer equations (Equation [3] and Section 2.3).

One-source models are generally worse at predicting H than TS schemes and are unable to provide independent soil and canopy estimates. However, OS methods are robust at calculating fluxes in remote regions where few data inputs are available (Bastiaanssen et al. 1998b). When appropriately handled, both OS and TS achieve comparable results (Kustas et al. 2007). HRMET attempts to combine the flexibility of OS with added precision from a TS radiation scheme. Although HRMET compared well against another model in its debut paper, greater uncertainty was evident at sparser canopy cover (Zipper and Loheide II 2014). This discrepancy may attribute to over-simplistic assumptions embedded in the model or to the uncertainty of the model inputs. In either case, HRMET performance has yet to be assessed with the EC method (Park et al. 2021).

2.2 Thermal remote sensing of radiometric temperatures

It is easiest to explain thermal remote sensing using Figure 3. The thermal sensor returns a raster map of discretized radiance values (L_s), considering the camera field-of-view [Φ], where each pixel value rests on a scale from 0-255 (for an 8-bit system). Unfortunately, L_s is convoluted with

other signals too. These components include upward-reflected solar radiance (L_U) from atmospheric gasses, aerosols and water vapour, downward atmospheric radiance and surrounding surface radiances reflected off the target surface (L_D), and the radiance of the target surface itself (L_B).

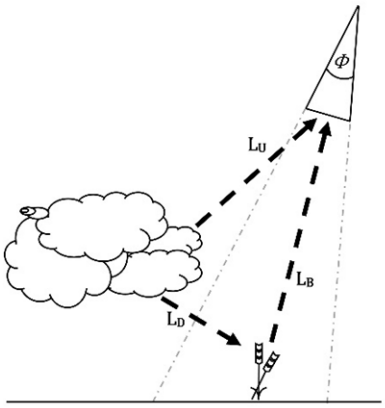

Figure 3. Remote sensing radiometric components

Where L_U is the upwelling sky radiance, L_B is the target area radiance, and L_D is the downwelling sky radiance contributing to the target area - adapted from (Jensen, 2015)

It is inferred from Figure 3 that each component is observed with the same spectral response; however, this is not always true when multiple thermal cameras are used in unison. Consequently, the component radiances are reinterpreted as spectral radiances [$W\ m^{-2}sr^{-1}\mu m^{-1}$], dividing by their respective central wavelength responses λ_{peak} [μm]. Thermal imagers (which operate in the near-infrared wavelengths) have a specified λ_{peak} within $0.8 - 1.4\ \mu m$. Continuing with the same variable naming convention, we include path transmissivity (τ) and target emissivity (ϵ) to relate L_S with its components in [5].

$$L_S = \tau\epsilon\ L_B + L_U + (1 - \epsilon)L_D \quad [5]$$

At this point, we may juggle between spectral radiance (L) and its temperature using Planck's Law [6]; where h_P is Planck's constant ($6.626\ x\ 10^{-34}\ J\ Hz$), c is the speed of light ($2.998\ x\ 10^{8}\ m\ s^{-1}$), k_B is the Boltzmann constant ($1.381\ x\ 10^{-23}\ J\ K^{-1}$), and T is the resultant temperature.

$$L = \frac{2hc^2}{{\lambda_{peak}}^5}\frac{1}{e^{h_P c/(k_B T)} - 1} \quad [6]$$

Within these interlaying steps, it is easier to adjust the sensor-observed temperature (T_{sensor}), subject to the sensor emissivity setting (ϵ_{sensor}), to a representative blackbody temperature ($T_{blackbody}$) with a blackbody emissivity ($\epsilon_{blackbody}$) of one [7].

[7] $$T_{blackbody} = \left(\frac{\epsilon_{sensor}}{\epsilon_{blackbody}} \, T_{sensor}{}^{4} \right)^{\frac{1}{4}}$$

Converting back to spectral radiance, we then ignore emissivity effects and simplify [5] to [8]. The τ and L_U terms can be estimated using an atmosphere transmission software or using linear regression with ground observations (Torres-Rua 2017). Finally, the spectral radiance of the target surface (L_B) can be deduced using [8] and its associated brightness temperature (T_B) retrieved from [6].

[8] $$L_S = \tau L_B + L_U$$

At this point, we can start to factor in the emissivity of the target surface. The Stefan-Boltzmann relationship of [9] is derived from Planck's Law and relates the hemispherical, full-spectrum radiant exitance (R_B with units $W\, m^{-2}$) to T_B through the Stefan-Boltzmann constant ($\sigma = 5.670\, x\, 10^{-8}\, W\, m^{-2}\, K^{-4}$). Equation [10] follows as a corollary to [9]; where T_R and T_{sky} are radiometric temperatures for the target surface and sky, respectively.

[9] $$T_B = \sigma^{-1} R_B^{1/4}$$

[10] $$T_B = [\epsilon (T_R)^4 + (1 - \epsilon) \left(T_{sky}\right)^4]^{\,1/4}$$

In some cases, T_B is treated with an emissivity of one allowing T_{sky} to be discarded. This assumption confounds efforts to retrieve a true radiometric temperature, but it is often necessary for implementation. A true radiometric correction would account for heterogeneous emissivities in the image, implications of wavelength sampling size (thermal vs full band), and differences between full hemispherical and finite viewing angle field-of-view (Norman and Becker 1995). Consequently, thermal imagery is often simplified to a blackbody brightness temperature with $T_B \approx T_R$. Furthermore, in UAV thermal imaging, the atmospheric corrections from [8] are sometimes also ignored, because the path lengths are relatively short; the resulting observed brightness temperature ($T_{B,obs}$) is then used. Even the best efforts to account for atmospheric and emissivity effects - resulting in the radiometric T_R - presents a less-than-perfect substitute for the true aerodynamic temperature required in [2].

2.3 Atmospheric surface layer overview

As the earth rotates, it generates a fluid-dynamics wake layer between the surface and atmosphere. Surface roughness and atmospheric meteorology influence the layer thickness at any given time and place. This layer is called the atmospheric boundary layer (ABL) and ranges

200-2000 m in depth. A subset of this is the atmospheric surface layer (ASL). The ASL exists closest to the earth's surface and is the portion of the ABL directly affected by surface roughness (Figure 4). A logarithmic wind profile of [11] is characteristic of the ASL. These profiles incorporate features related to the surface (measurement height z_u, displacement height d, and momentum roughness length z_{0m}) and parameters related to meteorology (friction velocity u_* and stability correction term for momentum ψ_m).

[11] $$u = \frac{u_*}{\kappa}\left(ln\left(\frac{z_u - d}{z_{0m}}\right) + \psi_m\right)$$

Meteorologic variables are joined through an atmospheric stability term (ζ). Atmospheric stability is typically expressed in terms of the Monin-Obukhov length parameter (L) - a term relating buoyancy and momentum forces to the turbulent kinetic energy - following [12].

[12] $$\zeta = \frac{z_u - d}{L} = -\frac{\kappa\, g\, (z_u - d)\, H}{\rho c_p\, T_{air}\, u^{*3}}$$

Atmospheric stability is classified in three ways: stable ($\zeta > 1$), when a parcel of air is colder than its surroundings and descends; neutral ($\zeta = 1$), when temperatures are close to equilibrium and vertical air movement is minimized; and unstable ($\zeta < 1$), when an air parcel is hotter than its surroundings and rises upward. These conditions have differing effects on the ASL, as shown in the stability correction terms for momentum (ψ_M) and sensible heat (ψ_H) under stable [13] and unstable [14] conditions.

[13] $$\psi_M = \psi_H = -6ln\,(1 + \zeta) \leftarrow \text{stable conditions}$$

[14] $$\psi_H = 2\,ln\left(\frac{1 + (1 - 16\zeta)^{\frac{1}{2}}}{2}\right); \psi_M = 0.6\psi_H \leftarrow \text{unstable conditions}$$

2.4 Eddy-covariance footprint

Eddy-covariance flux towers provide a direct estimate of LE and are frequently used to validate SEB models. These towers deploy within the atmospheric surface layer (ASL) to coincide with the logarithmic profiles of flux-gradient theory (Figure 4).

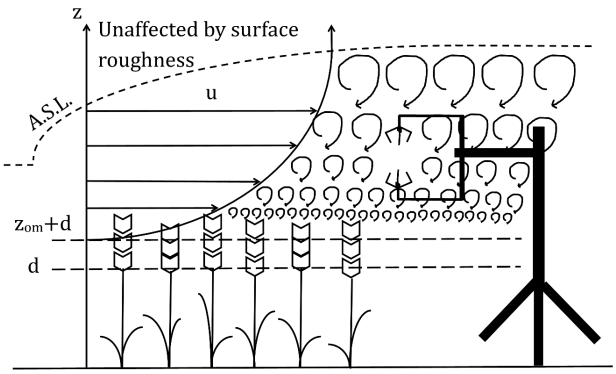

Figure 4. EC tower measuring turbulent wind eddies within the ASL

The wind profile (u) above the ASL is unaffected by surface roughness. Air movement below the momentum roughness length (z_{0m}) plus displacement height (d) threshold is diffusion-dominated.

A sonic anemometer measures instantaneous wind speeds in three directions. It is coupled with a high-frequency gas analyzer to detect water vapour fluctuations. At any given time, instantaneous wind speeds deviate around the mean value. Small covariances allow vapour to travel vertically even though the mean vertical wind speed $\overline{w}$ is essentially zero (Figure 5). The EC method determines the net covariance between specific humidity and vertical wind speed ($\overline{q'w'}$) and converts it into LE using air density (ρ_a) and the latent heat of vapourization (λ) in [15]. Friction velocity (u_*), a metric of momentum transfer, is similarly computed from the streamwise and vertical covariance ($\overline{u'w'}$) following [16]. Typical EC studies resolve 80% closure of the energy balance (Twine et al. 2000). Unaccounted energy is then attributed to storage terms and inconsistent spatial representations of the meteorological equipment. About 10% of the error revolves around the assumption that measured covariances are vertically uniform throughout the ASL (Foken 2016). Further EC assumptions require the flow field to remain constant over an averaging interval with no horizontal flux divergence or advection (Eugster and Merbold 2015).

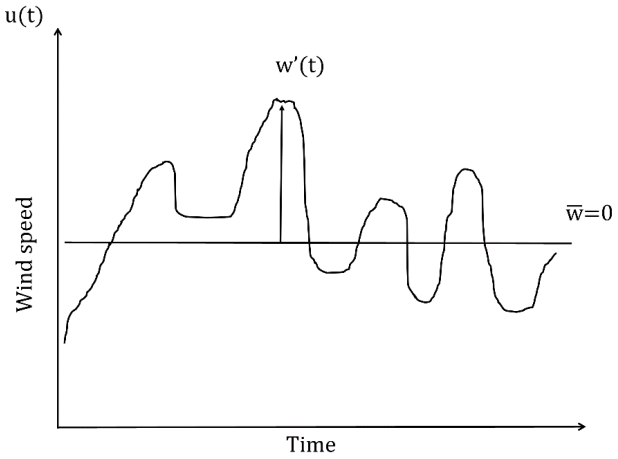

Figure 5. Reynolds decomposition

Instantaneous fluctuations in vertical wind speed (w') transport heat, momentum, and water vapour even though the mean vertical wind speed ($\overline{w}$) is zero.

[15] $$LE = \rho_a \lambda \overline{q'w'}$$

[16] $$u_*^2 = -\overline{u'w'}$$

Flux footprint models are based on boundary layer theory and used to distribute EC signals over a probability area. Time-series datasets are then combined to produce a climatology distribution. Kljun et al. (2002) developed a robust footprint model based on a backwards-Lagrangian particle touchdown probability - the likelihood that a particle (representing flux) originates from a source surface as traced backwards from the receptor. A simpler parameterization was later developed (Kljun et al. 2015) called the Flux Footprint Prediction (FFP) model and is further discussed in Section 4.3.1.

Eddy-covariance methods are unable to distinguish heterogeneity from variable surface sources within the footprint. Some studies have used remote sensing of normalized difference vegetation index (NDVI) and canopy closure to evaluate footprint representativeness in a particular landscape (Kim et al. 2006). Kirby et al. (2008) used this same method to disaggregate aircraft EC fluxes with land classification maps, apportioning flux with a probability weighting factor. Another method used land classification maps with overlapping footprints and multivariate regression to disaggregate the flux (Hutjes et al. 2010). More recently, management zones based on available water-holding capacity have been suggested, corresponding to physical field attributes of texture, organic matter, and topography (Bauer 2019). Based on similar principles, the evapotranspiration pattern index (ET_R) by Zipper and Loheide II (2014) presents a direct metric for disaggregating EC flux footprints.

3 ASSESSING A HIGH-RESOLUTION EVAPOTRANSPIRATION MODEL FOR FIELD CROPS

3.1 Preface

Prior to tackling eddy-covariance footprint disaggregation, we first require a surface energy balance model for retrieving high-resolution evapotranspiration patterns. Our candidate model, HRMET, was developed by Zipper and Loheide II (2014) and further tested by Nocco et al. (2019) and Park et al. (2021). Insofar as we know, HRMET has not yet been qualified against an eddy-covariance measured flux. This section sets out to amend this issue and specify the functional performance of HRMET, trialling different treatments of thermal surface temperature and assessing UAV LiDAR canopy structure retrieval techniques.

3.2 Abstract

Surface energy balance studies increasingly use unoccupied aerial vehicles (UAVs) for retrieving surface temperature and canopy structure. As applications of these models demand higher resolution evapotranspiration (ET) products, so does the need to provide scale-consistent inputs, particularly for canopy height, leaf area index (LAI), and canopy viewing fraction. Moreover, ambiguity surrounding temperature definition and accuracy questions the relevance of such thermal corrections in capturing spatial patterns of ET.

The present study assesses using UAV Light Ranging And Detection (LiDAR) to capture canopy height, LAI, and canopy viewing fraction as inputs to the HRMET model (High-Resolution Mapping of EvapoTranspiration). These methods were applied to non-irrigated barley and forage fields in a semi-arid continental climate. Despite the uncertainty with LAI field observations and differing canopy height interpretations with sparse canopies, the UAV LiDAR products demonstrated spatial coherence as a set, correspondence with field-scale observations ($RMSE$ $0.08 - 0.81\ m^2 m^{-2}$), and agreement with site knowledge.

The HRMET outputs were compared to eddy-covariance (EC) fluxes and local meteorology. The modelled latent heat flux achieved $RMSE$ between $79 - 136\ W\ m^{-2}$ tending to overestimate ET in full canopies (LAI$> 3\ m^2 m^{-2}$) when surface-to-air temperature differences exceeded $4 - 5\ °C$. Notably, none of the applied thermal corrections (ensemble emissivity, atmospheric) reconciled the difference in these conditions. An analysis (modified t-test) of thermal treatment concluded

that corrections to the raw thermal brightness temperature did not have a meaningful impact on thermal spatial patterns ($r > .99, p \ll 0.001$). A similar conclusion ($r > .93, p \ll 0.001$) was made about their effects on relative ET patterns (ET_R index). Consequently, a simple raw brightness temperature suffices to capture high-resolution patterns of ET. Lastly, it was found that an ET_R chronology of the 2018-2020 growing seasons adequately reflected changes to the hydrological environment and inferred crop stresses. These findings present a novel workflow for SEB users concerned with collecting high-resolution ET spatial patterns using UAVs over dryland field crops.

3.3 Introduction

3.3.1 New tools for high-resolution evapotranspiration

Thermal remote sensing estimates of evapotranspiration (ET) were first made possible with the 1982 launch of the Landsat 4 satellite (Engel and Weinstein 1983). Since then, the field has made steady progress through improved radiometric relationships (Moran 1990) and re-envisioned surface energy balance (SEB) schemes (Norman et al. 1995, Bastiaanssen et al. 1998a, Kustas and Norman 1999). Rapid advancements using Unoccupied Aerial Vehicles (UAV) enable versatile high-resolution inputs while testing the limits of traditional SEB schemes (Kustas and Anderson 2009, Niu et al. 2020). In contrast to the first thermal thematic mapper images, which were coarse ($30\ m$ resolution) and far removed from the Earth's surface ($> 700\ km$), low-altitude ($< 100\ m$) UAVs capture thermal patterns at the sub-metre scale. Similarly, detailed canopy structures are now feasible using UAV photogrammetry and Light Detection And Ranging (LiDAR) methods providing consistent input scales for high-resolution SEB modelling. Whereas before, model verification using the eddy-covariance (EC) method offered a coarse comparison with one overlapping pixel, now the comparison is ameliorated using sub-footprint weighting schemes for subsequently smaller pixels (Sutherland et al. 2017). However, the application of these new tools has its own unique set of challenges and trade-offs between correctness and useability: notably between interpretations of thermal temperature (Norman et al. 1995, Torres-Rua 2017, Kelly et al. 2019) and LiDAR limitations and operational errors in acquiring short vegetation foliage density and structure (Deems and Painter 2006, Nie et al. 2016). More field feasibility studies, like that presented here, are necessary for addressing these issues and coming up with workable solutions in the UAV-driven SEB arena.

3.3.2 SEB overview

The goal of a thermal remote sensing SEB model is to account for latent heat (LE), analogous to ET, through an energy balance [17]. Ignoring storage (a common practice for short vegetation applications) and advective terms (more impactful when considering irrigated cropland), the core components of net radiation (R), soil heat flux (G), and sensible heat (H) are estimated leaving LE as a residual. The R and G terms can be measured in-situ using radiometers and soil heat flux plates, and their values are assumed to represent the whole landscape. Sensible heat is then calculated according to [18] with: T_{aero} aerodynamic surface temperature, T_{air} air temperature, r_{ah} aerodynamic resistance to sensible heat, r_{ex} excess resistance, c_p specific heat capacity of air, and ρ_{air} density of air. Equation [18] requires r_{ex} to adjust for the transport of sensible heat experiencing more resistance that that of momentum transfer. Moreover, an additional resistance correction is sometimes used to address the inherent differences between the observed radiometric temperature (T_R) and the theoretical aerodynamic temperature (Matsushima 2005, Kustas and Anderson 2009). Interpreting T_{aero} from the raw thermal brightness remains a challenging endeavor.

[17] $$LE = R - G - H$$

[18] $$H = \rho_{air}\, c_p \frac{T_{aero} - T_{air}}{r_{ah} + r_{ex}}$$

3.3.3 UAV thermal

Although grounds for an aerodynamic temperature substitution (replacing T_{aero} with T_R) are firmly established (Brutsaert et al. 1993, Norman and Becker 1995), the prerequisites of addressing ensemble emissivity (converting brightness temperatures to radiometric temperatures) and path effects (atmospheric transmissivity and upwelling radiation) are often unmet. Ambiguity surrounds most efforts to obtain T_R from the raw brightness temperature ($T_{B,obs}$) of UAV thermal. Since a $\pm 0.5°K$ absolute accuracy is unlikely with most sensors (Kelly et al. 2019), it questions whether simpler interpretations can still be helpful. The direct use of $T_{B,obs}$ is constrained by confounding atmospheric effects (upwelling irradiance L_U and transmissivity attenuation τ) with reflectance from features around the target and with radiance from the target itself. In response, the standard practice is to atmospherically correct $T_{B,obs}$ to a surface brightness temperature (T_B) and factor in emissivity (ϵ) to obtain the target radiometric temperature (T_R). One compromise is to only use an observed radiometric temperature ($T_{R,obs}$) by ignoring τ and L_U effects. Although harmless in low-flying UAV flights ($< 30\ m$), impacts at higher elevations can exceed $\pm 4°K$ (Sagan et al. 2019).

Other times, it is prudent to ignore the ensemble emissivity correction proposed by Norman and Becker (1995) and assume a constant emissivity (ϵ of 1.0 or otherwise). The oversight of this is less severe, $\pm 1.25°K$ error according to Kelly et al. (2019). With Brutsaert et al.'s (1993) $\pm 0.5°K$ thermal accuracy objective far in the background, what operational strategies will conserve spatial patterns of ET even if absolute values are off?

Often atmospheric correction is interpreted as a linear modification to the raw digital numbers from a rectified source (Xia et al. 2016). An analogous approach considers ground-level radiance observations (Torres-Rua 2017) and enables direct interpretation of the atmosphere components transmissivity (τ) and upwelling radiation (L_U). The linear relationship of either method suggests that such atmospheric corrections affect ET patterns in uniform proportion. In contrast, with variable emissivity, the temperature distribution is non-linearly adjusted according to the 4th power Stephan-Boltzmann relationship with radiance [9]. Although atmospheric correction magnitudes are greater, the ensemble emissivity is suspected to have more influence on spatial patterns.

3.3.4 UAV LiDAR

With increasingly finer-resolution thermal-driven SEB applications, the need for higher-resolution canopy structure inputs becomes apparent (Sutherland et al. 2014). These inputs include canopy height (h), Leaf Area Index (LAI), and canopy viewing fraction (f_c) and are often inter-related - inferring one from the others. Until recently, spatially-continuous canopy structures were found using discrete ground sampling and spectral indices or stereo photogrammetry; however, developments in three-dimensional photogrammetry and LiDAR now enable superior structural descriptions (Leberl et al. 2010, Sutherland et al. 2017, Maesano et al. 2020) at resolutions consistent with UAV thermal remote sensing (Sutherland et al. 2014, Aboutalebi et al. 2020). Among these methods, UAV LiDAR has greater accuracy and can interpret the digital elevation model beneath a canopy (Widyaningrum et al. 2017).

In short, LiDAR is an active laser pulse device that returns three-dimensional point clouds at survey-grade precision. An emitted beam casts a UAV height-dependent spread over a surface and reflects back to the sensor as a return. Multiple returns are possible from the same pulse if the beam spread covers sufficiently contrasting terrain heights; otherwise, only single discrete returns are posted (Deems and Painter 2006). Typically, only single returns are made for short ($< 1\ m$) vegetation (Luo et al. 2014, Nie et al. 2016).

Canopy heights are interpreted as the distance between the point cloud and an interpreted Digital Elevation Model (DEM) of the bare ground surface. Due to the vertical orientation of plant stems

and leaves, h is systematically underestimated, with the laser pulses experiencing 'time-walk' and vertical errors (Deems and Painter 2006). Ten Harkel et al. (2020) observed this phenomenon and associated it with under-sampling. They concluded that spatial patterns are preserved even when h is underestimated. Song et al. (2020) made a similar conclusion with their UAV photogrammetry method of LAI estimation. A simple scaling correction with field observations can adjust the magnitude of h accordingly.

The canopy viewing fraction (f_c) as it pertains to thermal-driven SEB models, is the portion of a thermal camera's field-of-view taken up by the canopy (Norman et al. 1995). Analogies of f_c for LiDAR vary depending on if number of returns or intensities are used (Luo et al. 2014) or if it includes all scan angles or just nadir scans (Korhonen et al. 2011). A leaf penetration index approach [19] considers the relative number of canopy (n_c) and ground (n_g) classified points and has been effective over maize f_c (Luo et al. 2014, Nie et al. 2016). Canopy and ground returns are classified based on an arbitrary cut-off height above the DEM or by combining spectral information (Aboutalebi et al. 2020). Also, issues of f_c saturation are known to occur in dense canopy coverage where ground points are missing (Richardson et al. 2009); however, relationships to canopy height (Nie et al. 2016) suggests an opportunity for gap filling.

[19] $$f_c = \frac{n_c}{n_g + n_c}$$

A leaf area index (LAI), interpreted as the area of leave surface (one-sided) over a unit area of ground, is used to estimate roughness lengths for SEB applications (Raupach 1994). The meaning of LAI can be reinterpreted if leaf inclination angle, canopy clumping, or non-transpiring foliage are considered. Ignoring canopy clumping and dead leaf elements, an effective LAI (LAI_e) can be found with airborne LiDAR using a Beers-Lambert style regression with field observations (Solberg et al. 2006). Similar to the leaf penetration index approach, this interpretation [20] considers the relative number of ground and canopy points viewed from above and corrects for leaf inclination using a decay coefficient (κ). Typically assumed to be 0.5, based on a spherical canopy structure and nadir viewing angle (Nilson 1971, Kustas and Norman 1999), κ can also be uniquely determined for each canopy through regression with LAI observations (Solberg et al. 2006, Korhonen et al. 2011, Nie et al. 2016). Although effective, this method requires at least one ground return at the calculation resolution to work (Richardson et al. 2009).

[20] $$LAI_e = \frac{-ln(\frac{n_g}{n_g + n_c})}{\kappa_c} = \frac{-ln(1 - f_C)}{\kappa_c}$$

3.3.5 HRMET

Surface energy balance models employ thermal remote sensing to resolve LE as a residual. Spatially continuous H retrieval is founded on a similarity between aerodynamic and radiometric interpretations of temperature (T_{aero} and T_R, respectively). Although the suggested accuracy of substituting T_R for T_{aero} is $< 0.5°K$ (Brutsaert et al. 1993), inconsistencies $> 5°K$ are frequent (Matsushima 2005) which plague H estimates over hot, full cover canopies (Troufleau et al. 1997). Two-source (TS) models mitigate this error by calculating canopy and soil H fluxes separately (Kustas and Norman 1999), and one-source (OS) models bypass this issue by contextually scaling with temperature gradients (Bastiaanssen et al. 1998b, Allen et al. 2007). After addressing $T_{aero} - T_R$ differences, TSEB and OS approaches can offer similar LE accuracies (Kustas et al. 2007, Brenner et al. 2017). To achieve this, TS models require accurate T_R retrieval (Xia et al. 2016); while, OS contextual scaling relies heavily on subjective hot and cold pixel selection. Other OS solutions use empirical adjustment factors with difficult-to-ascertain aerodynamic relationships (Troufleau et al. 1997, Matsushima 2005). It has been suggested that a hybrid approach is needed to integrate TS and OS formulations for combined accuracy and robustness (Brenner et al. 2017).

The High-Resolution Mapping of EvapoTranspiration (HRMET) model uses a hybrid TS and OS schema (Zipper and Loheide 2014). This model combines a simplified TS radiation partitioning scheme with an OS bulk H evaluation (Norman et al. 1995). A parallel resistance network accounts for both momentum and sensible heat influences (Kustas and Norman 1999) in addition to Norman and Becker's excess resistance (1995), which Zipper and Loheide II (2014) claim mitigates $T_{aero} - T_R$ differences. An assessment of HRMET's response to hot full cover canopies (exasperating $T_{aero} - T_R$) remains untried. In the same study (Zipper and Loheide 2014), HRMET was validated against point calculations of the Shuttleworth-Wallace model over a barley field at $1.0\ m$ resolution. In other studies it achieved favourable results over sweet potato, corn, peas, and pearl millet (Nocco et al. 2019) and satisfactorily captured intra-field ET variation in a peach orchard (Park et al. 2021). However, the performance of HRMET has not yet been benchmarked against eddy-covariance (EC) flux tower observations.

In addition to HRMET, Zipper and Loheide II (2014) proposed a relative evapotranspiration index (ET_R). The aim was to develop a metric for precision agriculture to delineate water management zones. Since ET is mostly transpired in dry conditions, the patterns reflect plant access to available soil moisture. ET_R allows direct comparison between image dates and reveals the intrinsic spatial productivity of a field over an observed range of hydrological conditions for a select

crop species (Nocco et al. 2019). This information is useful for informing precision farming irrigated and dryland practices.

3.3.6 Goals

In this study, we assess the application of high-resolution thermal and canopy structure inputs within the HRMET framework. Furthermore, we trial varying degrees of thermal correction as inputs for the HRMET model. We evaluate how these thermal inputs affect the estimates of SEB components and then assess whether they substantiate a difference in ET spatial patterns as depicted using ET_R. This study explores a workflow for SEB users who prefer a simplified model driven by raw brightness temperature to map high-resolution differences in ET.

3.4 Methodology

3.4.1 Data collection

Area of study

The study location is situated near Saskatoon, Saskatchewan, in the Canadian Prairies (Figure 6). Acquired from local meteorological data, this semi-arid region produces $350\ mm$ of average annual precipitation and has average seasonal temperature fluctuations between $-37°C$ and $34°C$, consistent with a continental climate (Government of Canada 2021). The region is characterized by a short growing season, having an average of 169 consecutive days that are above $0°C$ (Government of Canada 2021), with moisture-limiting single crop rotations. This study observed two fields, $7\ km$ apart and $40\ km$ SE of Saskatoon, Saskatchewan. One field (coordinates: 51.937, -106.374) grew silage barley (2018-2019), while the other field (coordinates: 51.888, -106.385) grew hay forage (seeded 2019, monitored 2019-2020); hereafter, these sites are referred to as Barley and Forage). Both sites consist of dark brown chernozemic soil with a fine sandy loam texture (Appendices A2 and A3). The landforms are slightly undulating ($< 2\%$ slope) glaciolacustrine till with knob and knoll depressions (Ellis et al. 1970). Saline terminal wetlands and small water bodies pocket the landscape around each site.

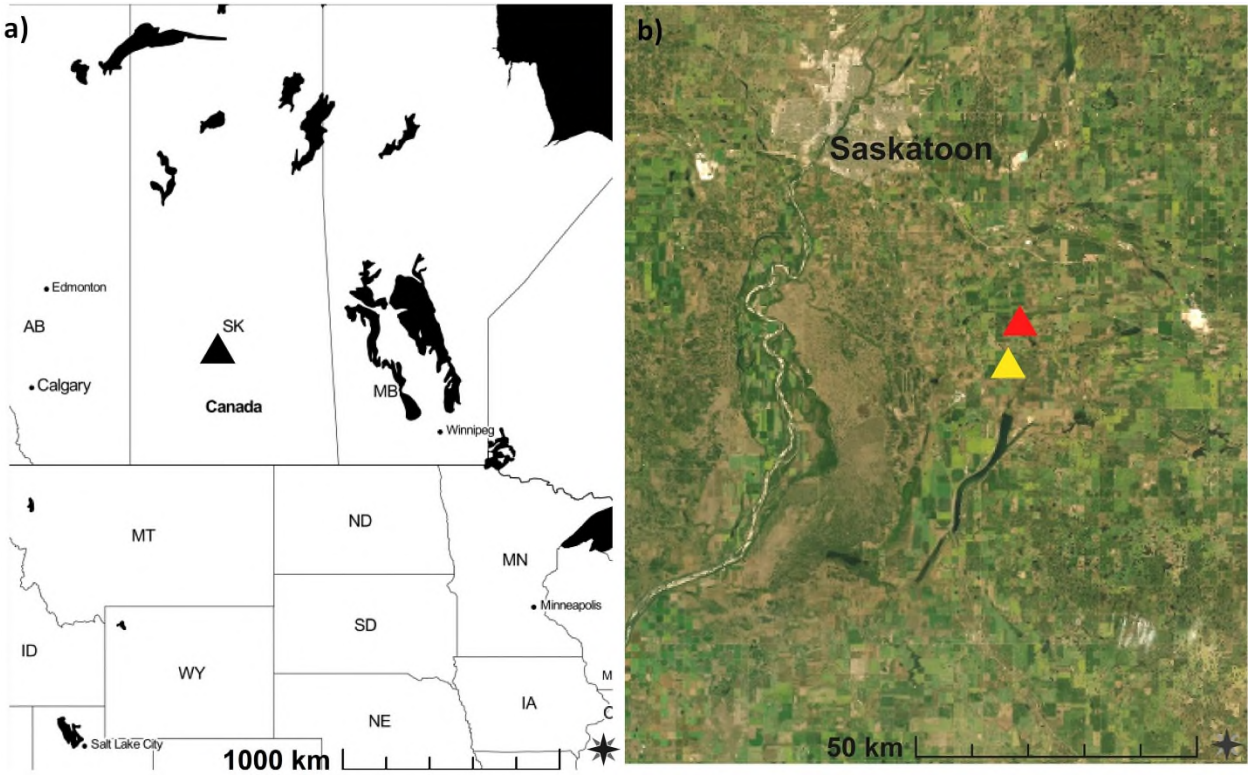

Figure 6. Site overview
a) regional and b) local geography

Flux tower

We monitored Barley and Forage using an EC flux station complete with 20 Hz gas analysis (LI-COR 7500A) and three-dimensional sonic wind speed (CSAT3, Campbell Scientific) and $30\ min$ records of air temperature and relative humidity (HMP45C212, Campbell Scientific), four-component net radiation (CRN1, Campbell Scientific), surface temperature (SI-121, Apogee), soil heat flux (HFP01, Hukseflux), and $0.1\ m$ and $0.2\ m$ soil moistures and temperatures (CS650, Campbell Scientific). Each year, the towers were set up in the same approximate locations with flux measurement heights between $1.5 - 2.5\ m$.

In summary, fluxes were processed in EddyPro software (v7.0, 2021) at $30\ min$ flux averaging intervals with a 10% missing sample allowance. Dynamic metadata files of biweekly crop height and instrument heights were supplied. A block averaging detrending accompanied double axis coordinate rotations. The Webb et al. (1980) method was also used to adjust for density fluctuations. High and low-pass filtering corrections were applied using the Moncrieff et al. (2004) and (1997) techniques. We used EddyPro default settings for de-spiking, setting absolute limits, and addressing discontinuities and the angle of attack. Finally, the time series data were filtered in Rstudio (R v4.0.2, 2020) to remove outliers containing $LE < -100\ W\ m^{-2}$ and $u_* < 0.1\ m\ s^{-1}$.

UAV data

Thermal surface temperature data from 17 flights (10 Barley, 7 Forage), captured over five days and across three years, were used in this project (Table 1). Corresponding LAI, h, and f_c for each day were acquired using UAV LiDAR. Flight schedules included a mixture of scanline orientations (due to chosen perpendicular flight paths with the prevailing wind), with most being cross-flight patterns as prescribed by ten Harkel et al. (2020). For additional flight log metadata, refer to Appendix A1.

Table 1. List of flights, dates, and EC footprint overlap times

Image [$yy\_DDD\_p\_\#$]*	Date	Site	Start overlap CST [$hh{:}mm{:}ss$]	End overlap CST [$hh{:}mm{:}ss$]	Solar zenith ∠ [°]
18_207_e_1	July 26, 2018	Barley	13:03:00	13:10:00	32.7
19_177_e_1	June 26, 2019	Barley	11:24:00	11:33:00	34.9
19_177_e_2	June 26, 2019	Forage	12:35:00	12:40:00	29.4
19_177_e_3	June 26, 2019	Forage	14:32:00	14:37:00	32.8
19_177_h_1	June 26, 2019	Barley	15:09:00	15:20:00	38.1
19_177_e_4	June 26, 2019	Barley	15:30:00	15:40:00	39.3
19_184_h_1	July 3, 2019	Barley	7:41:00	7:54:00	67.4
19_184_h_2	July 3, 2019	Forage	9:03:00	9:10:00	54.8
19_184_h_3	July 3, 2019	Forage	11:31:00	11:39:00	34.7
19_184_h_4	July 3, 2019	Barley	12:41:00	12:45:00	29.6
19_184_h_5	July 3, 2019	Barley	14:14:00	14:23:00	31.6
19_184_h_6	July 3, 2019	Forage	15:35:00	15:44:00	40.2
19_212_h_1	July 31, 2019	Barley	10:48:00	11:00:00	44.0
19_212_h_2	July 31, 2019	Forage	13:12:00	13:18:00	33.8
19_212_h_3	July 31, 2019	Barley	14:37:00	14:47:00	37.7
20_210_h_1	July 28, 2020	Barley	11:20:00	11:34:00	39.8
20_210_h_2	July 28, 2020	Forage	14:27:00	14:35:00	36.4

* Flight identification label yy_DDD_p_# corresponds to the year, the Julian day, the payload (e for ThermoMAP, h for FLIR Vue Pro R), and the flight number

Equipment

A combination of UAV and handheld instrumentation was used in this study. We took thermal images using EbeeX and Ebee+ fixed-wing UAVs equipped with FLIR Vue Pro R and FLIR Vue Pro (ThermoMAP) sensors, respectively. Factory specifications attest to $\pm 5\,°C$ accuracy and central wavelengths of 1079 and 1029 nm for ThermoMAP and FLIR Vue Pro R, respectively (Appendix A4). A handheld FLIR T650sc ($\pm 1\,°C$, 1029 nm central wavelength) was used for referencing atmospheric corrections. High-resolution LAI_e, h, and f_c were also collected using a DJI M600 Pro hexacopter equipped with a Riegl miniVUX1-UAV LiDAR (laser specifications: $0.0015\ m$ accuracy, $0.001\,m$ precision) and an APX-15 IMU device for motion corrections. Coinciding ground-level LAIs were observed using a Decagon LP-80 ceptometer ($0.865\ m$ wand length) in both full sun and partial sunlit conditions.

Sampling

For ground validation efficiency, we flagged observation points (Figure 4) across three W to E transects spaced $200\ m$ apart according to the 100:1 rule with EC fetch (Burba 2013). We surveyed additional points around each tower, apparent saline outcrops (observed white precipitate on the soil surface and impeded emergence), and in landscape depressions, where we expected to see a sufficient range of observations. Field-scale LAI and crop height information were used instead of specified points for the 18_207_e_1 image. Also, in 2020 (since only one image was collected) we chose sample spots along a single transect upwind of each flux tower. Flags were surveyed ($\pm 0.03\ m$ accuracy) using a Leica GPS with real-time kinetics and precise point processing corrections with the Natural Resources Canada online tool. We made observations from these placemarks about one metre south of each flag. Thermal observations were collected at chest height (approximately one metre above the ground) to achieve a field-of-view of 0.6 m (the width of three crop rows at Barley). Since Forage vegetation was more scattered, we attempted to balance the relative proportions of grass, alfalfa, and bare ground viewed in each observation. Meanwhile, we recorded LAI as an average of three cross-row and with-row means within a 1 m^2 zone (Figure 8). With-row measurements were taken at about one-third of the crop row spacing (4" from the crop row base). After the above-canopy reading, we took a second below-canopy reading to ensure stability within $\pm 10\%$ to mitigate light transience. A separate set of LAI observations (not dedicated to this study) were collected as routine measurements for the upkeep of the flux tower sites; these took a spatial average of three spot measurements across a $5\ m$ transect. The two sets of LAI are separate because the latter has a coarser spatial registration; we label these 'dedicated' or 'undedicated', respectively. Average field heights were taken with a measuring tape as the height of horizon disappearance from a level viewpoint ($\pm 0.05\ m$ accuracy).

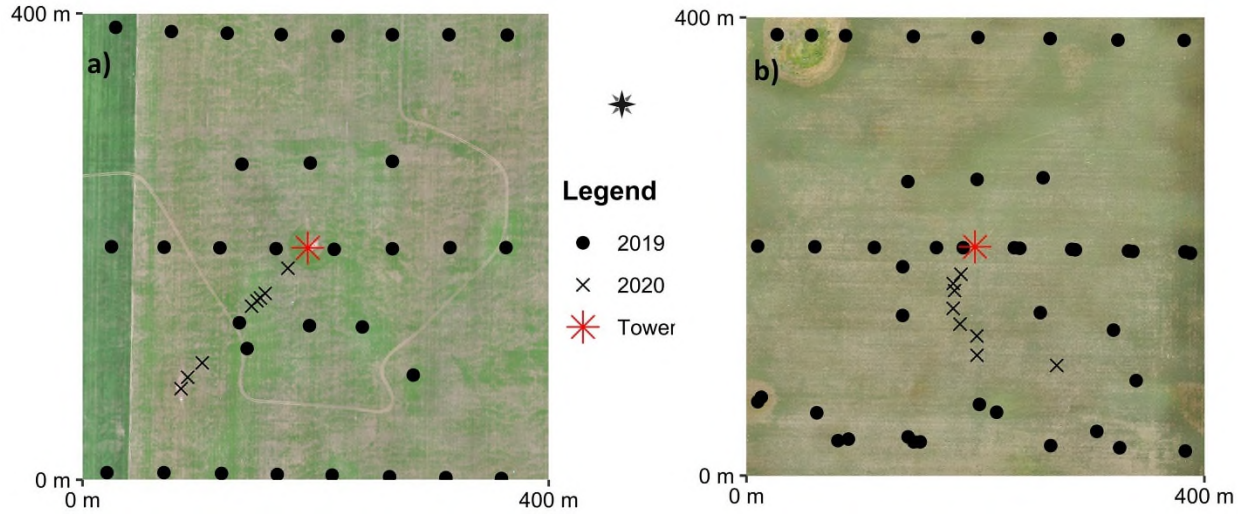

Figure 7. Sampling maps
a) Barley and b) Forage

Figure 8. Example of field LAI measurements
a) with-row and b) cross-row

Statistics

We used a modified t-test (Clifford et al. 1989, Dutilleul 1993) to assess spatial correlations amongst thermal temperatures and ET_R results. This test provides a Pearson correlation coefficient (r) corrected for spatial autocorrelation by reducing the effective number of observations. We performed the test using the SpatialPack (Vallejos et al. 2020) package in R (v4.0.2, 2020). We applied the *modified.ttest* function with 20 class categories and default settings on random raster subsets of $10{,}000$ cells each. Results from this test include r, the effective number of observations (n_{mod}), and the significance p-value.

Three-dimensional point clouds were surveyed using UAV LiDAR. We flew LiDAR at around 100 $magl$ at average speeds of $6\ m\ s^{-1}$ (Appendix A1). To improve ground point recovery in dense vegetation (Richardson et al. 2009), we considered all available scan angles (typically 0-80°) similar to the multi-angle photogrammetry approach used by Song et al. (2020). DEMs were

retrieved from early-season point clouds and provided good descriptions of depressional areas for referencing h throughout the analysis. The LiDAR GNSS survey and base station data post-processing was performed in Leica Infinity (v3.0.1, 2018) with precise point positioning using the Natural Resources Canada online system. Post-processing of the APX-15 IMU data to develop a smoother best estimate of the trajectory of the LiDAR system was performed with POSPac UAV (v8.5, 2020). RiPROCESS software (v1.9.1, 2021) combined post-processed trajectory with laser scans to then develop, refine and generate geo-registered point clouds.

3.4.2 Canopy height

Canopy height models (h) were inferred from the bare-ground DEM using the *lasground* function in LAStools (Isenburg 2021). We extracted h from the post-processed point cloud as the vertical distance between each point and the ground DEM. We then converted h to raster format using a 95^{th} percentile height and aggregating to $0.6\ m$ (Barley) and $1.0\ m$ (Forage) resolutions. Afterwards, h was scaled manually to match field observations. For a scaling factor, we used the fraction of the average field height over the unscaled raster average height. This method corrected h magnitude while preserving its high-resolution spatial patterns.

3.4.3 Canopy viewing fraction

Canopy viewing fractions were acquired using equation [19]. Similar to Nie et al. (2016), only discrete returns were considered. We used the lidR package in R (Roussel and Auty 2021) to analyze point clouds and statistics: its *filter_poi* function separated ground and canopy returns with date-specific cut-off heights of $0.05 - 0.20\ m$, and *grid_metrics* calculated the number of canopy points n_c and ground points n_g at three-metre resolution. We adopted a sigmoidal regression with the spatially continuous h to gap-fill areas with missing or insufficient number of ground points. This flexibility allowed us to adjust the required number of ground points from one (Richardson et al. 2009) to a statistically better sample size of twenty. Concurrent f_c and LAI interpretations used the same height and ground return thresholds ($5 - 20\ cm$ and $20\ pts$ respectively).

3.4.4 Effective leaf area index

The Beers-Lambert approach [20] was used to solve LAI_e helped by the lidR package (Roussel and Auty 2021) in R (v4.0.2, 2020). We applied [20] to the point cloud directly instead of using f_c, and considered the relative number of canopy and ground return points at each pixel. We then

adjusted κ_c so that LAI_e matched LAI field measurements. This effectively made κ_c an empirical adjustment factor unique to each LiDAR point cloud. The $lasclip$ function helped us retrieve points within a $1.5\,m$ search radius of the field observation locations. Afterwards, we used the *grid_metrics* function to help calculate LAI_e at three-metre resolution with uniform cut-off heights for each point cloud ranging from $0.05\,m$ (sparser canopies) to $0.20\,m$ (denser coverage). As with f_c, gap filling followed a sigmoidal regression with h.

3.5 Thermal corrections

To get $T_{B,obs}$ from raw thermal data, we first had to apply internal camera corrections and geo-register with ground control points; these were done in Pix4D software (v4.3, 2021). We used three to five ground control points consisting of a one-by-two-metre reflective foil for each flight. Orthomosaics of $T_{B,obs}$ were then generated at $0.05\,m$ and $0.15\,m$ resolutions for FLIR Vue Pro R and ThermoMAP cameras, respectively.

3.5.1 Ensemble emissivity correction

To isolate $T_{R,obs}$ from the target surface, we used a two-component ensemble emissivity ($\epsilon_{ensemble}$) following Norman and Becker (1995). The correction applies canopy (f_c) and soil (f_s) viewing fractions to distribute emissivity (ϵ_c and ϵ_s) according to $T_{B,obs}$ in [21]. The $\epsilon_{ensemble}$ replaces default emissivity ($\epsilon_{default}$) settings in the thermal imagers (usually 0.95 or 1.0) and relates $T_{R,obs}$ to $T_{B,obs}$ following [22] (Nieto et al. 2019). Alternately, assuming atmospheric corrections, the relationship holds for obtaining T_R from T_B following [23].

[21] $$\epsilon_{ensemble} = \frac{f_c\,\epsilon_c T_{B,obs} + f_s\,\epsilon_s T_{B,obs}}{f_c\,T_{B,obs} + f_s\,T_{B,obs}}$$

[22] $$T_{R,obs} = \left(\frac{\epsilon_{default}}{\epsilon_{ensemble}}\,{T_{B,obs}}^4\right)^{\frac{1}{4}}$$

[23] $$T_R = \left(\frac{\epsilon_{default}}{\epsilon_{ensemble}}\,{T_B}^4\right)^{\frac{1}{4}}$$

The $\epsilon_{ensemble}$ correction causes the temperature to increase more over sparse canopies than over full canopies. A sparse canopy has $\epsilon_{ensemble}$ closer to that of soil ($\epsilon = 0.95$), while the dense canopy has $\epsilon_{ensemble}$ nearer to that of vegetation emissivity ($\epsilon = 0.98$). Being farther away from a blackbody default emissivity ($\epsilon = 1.0$) causes the sparse canopy temperature shift to be higher.

3.5.2 Atmospheric correction

The atmospheric correction follows the 'vicarious calibration' approach presented by Torres-Rua (2017). It uses the logic that ground-level thermal observations are unaffected by path irradiance (L_U) and transmissivity (τ) attenuation. Ground-level and UAV temperatures are converted to spectral radiances (L_B and L_S) using Planck's Law and the thermal imager central wavelengths. These are arranged as a linear regression according to [8], which is then inverted as a radiometric correction to convert L_S to a ground-level equivalent (in place of L_B). Afterwards, the adjusted spectral radiance is reverted to $T_{R,obs}$.

3.6 HRMET processing

This study uses the HRMET (Zipper and Loheide 2014) SEB model coded in R (v4.0.2, 2020) with some processing and input differences. First, the code was vectorized and adapted for parallel processing to increase speed. Then the incoming longwave formula was replaced with measured values. Lastly, a LiDAR interpretation of f_c was used instead of the LAI-Beers law relationship.

3.6.1 Key processes

HRMET uses the radiation partitioning prescribed by Norman et al. (1995), where the fractions of longwave and shortwave radiation reaching the soil (X) are related to the canopy viewing fraction (f_c) following [24]. The constant 0.9 pertains to Nilson's (1971) description of gaps in a spherical canopy structure. Moreover, we approximated soil heat flux following $G \approx 0.35\ R_{n,s}$, as a ratio of net soil radiation ($R_{n,s}$).

[24] $$X = exp(0.9\ ln(1 - f_c))$$

The parallel resistance scheme employed by HRMET to solve [18] uses the sensible heat description of aerodynamic resistance (r_{aH}) according to Kustas and Anderson (2009). It includes an additional excess resistance (r_{ex}), originally intended to compensate sensible heat applications for use in a momentum-based theory (Norman and Becker 1995); however, HRMET considers it as a radiometric correction factor for using T_R in place of T_{aero}.

Model uncertainty is assessed through a Monte-Carlo permutation approach. HRMET computes 100 estimates at each cell based on randomly selecting inputs from their uncertainty distributions. The inputs are varied using a normalized distribution of the 95% confidence uncertainty estimates. Uncertainty estimates for raster inputs consider spatial uncertainty using the mean and standard

deviation from a three-by-three moving window. Meanwhile, meteorological inputs include temporal uncertainty using the mean and standard deviation from the surrounding $30\ min$ records. All 95% confidence uncertainty estimates (u_{Total}) were calculated according to [25] where $u_{instrument}$ is the instrument accuracy and $u_{measurement}$ is twice the standard deviation from the moving window analysis (raster inputs) or the adjacent records (time series inputs). In this way, HRMET creates mean and standard deviation maps for each SEB component.

[25] $$u_{Total} = \sqrt{u_{instrument}^2 + u_{measurement}^2}$$

3.6.2 Eddy-covariance comparison

UAV and flux tower comparisons have some issues when it comes to temporal and spatial registration, the aligning of time intervals and measurement areas. First, while flux tower measurements are made with $30\ min$ averaging intervals, the UAV overpass time of the footprint only takes $5 - 10\ min$. We address this by isolating the UAV footprint overpass time and, if it straddles two $30\ min$ records, using linear interpolation to weight the corresponding meteorology inputs for HRMET. The same technique is applied to compare SEB outputs with $30\ min$ EC fluxes. Moreover, HRMET accounts for temporal stability using its permutation-based Monte-Carlo strategy, which provides confidence boundaries for each SEB output. To encourage spatial registration between HMRET and EC footprints, we issued a weighting function following [26] where a is the pixel area, $\frac{f_i}{\Sigma f_i}$ is the fraction of the total sum of footprint values in the footprint area at a given cell i, χ_i is the SEB component (LE, H, R, or G) value at each coinciding pixel, and χ_f is the footprint weighted bulk SEB component value.

[26] $$\chi_f = a \sum \left(\frac{f_i}{\Sigma f_i} \chi_i \right)$$

Following Brenner et al. (2017), we apply a Bowen-ratio closure to our eddy-covariance H and LE terms for comparison with HRMET. Upper and lower thresholds are represented using closure bounds (residual energy assigned wholly to H or LE). We calculated residual energy (RES) using $RES = R - H - LE - G$ (Foken 2008).

Flux tower G was derived from a soil heat flux plate at $0.10\ m$ depth with attenuation corrections following [27]; where G_{obs} is the soil heat flux at $0.10\ m$ depth, dT is the change in $0.10\ m$ soil temperature between $30\ min$ records, C_s is the thermal conductivity of the soil, z_{soil} is the $0.10\ m$ soil depth, and t is the time of observation ($30\ min$).

[27] $$G = G_{obs} + dT\ C_s \frac{z_{soil}}{t}$$

3.6.3 Relative evapotranspiration

Following Zipper and Loheide (2014), we represented spatial ET patterns using the ET_R index. This was done by stretching each ET raster between the 2.5^{th} and 97.5^{th} percentiles (95% confidence range) and normalizing between zero and one. The output ET_R contains values from zero (low) to one (high) representative of the relative ET patterns within each image. By ordering ET_R images sequentially, we address how ET patterns relate with changing hydrology and canopy development.

3.7 Results and discussion

3.7.1 Background conditions

Hydrology

Barley and Forage received most of their soil moisture from winter runoff and spring rains (Figure 9), then precipitation tapered off in July-August. Cumulative ET continued strong until available soil moisture depleted, then ET too tapered off. Forage maintained higher ET rates throughout the season; this is explained by deeper established root systems than at Barley. The 2018 season stands out with higher antecedent soil moisture, scant Spring rains, and less overall precipitation. Conversely, the 2019-2020 rainfalls came earlier in greater quantity. The soil moisture drawdowns in 2018-2019 are relatively steeper than in 2020, indicating higher drought stress in these first two years. Meanwhile, the UAV flight dates were focused on the peak growth periods and moisture-limiting transitions (where cumulative ET plateaus).

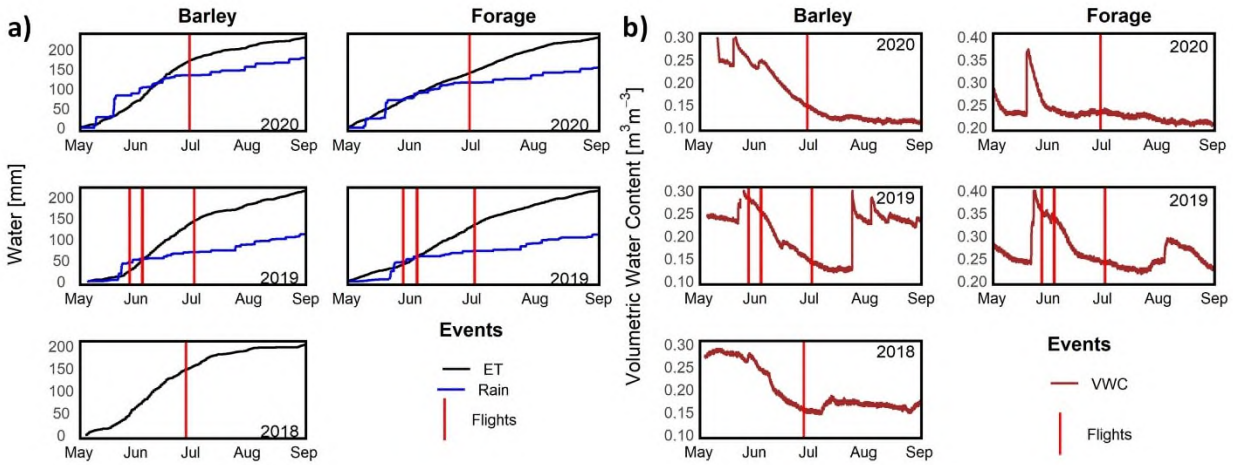

Figure 9. Overview of seasonal site hydrology with corresponding flight overpasses
a) Cumulative precipitation and ET and b) $0.2\ m$ volumetric soil moisture

Meteorology

Unlike UAV data, which provides a snapshot in time, other SEB meteorological inputs are averaged over $30\ min$ intervals and are subject to uncertainty from shifting meteorological conditions. To help interpret HRMET outputs, we present flight occurrences in context with the daily energy dynamics in R, G, and the surface-air temperature gradient (Figure 10). In Appendix A5, we provide further meteorology measurements coinciding with each UAV flight (shortwave incoming, longwave outgoing, air temperature, surface brightness temperature, vapour pressure deficit, wind speed, friction velocity, and relative humidity).

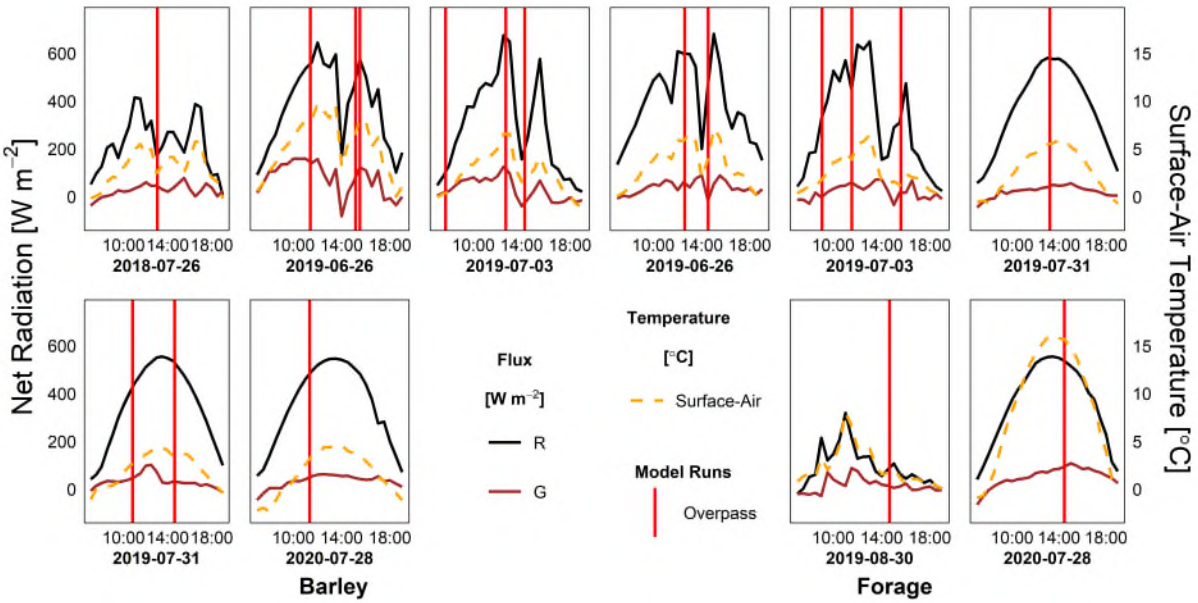

Figure 10. Daily energy dynamics with coincident UAV overpasses

3.7.2 Applying UAV LiDAR

For brevity, we present UAV LiDAR figures for Barley and include Forage results only in the table summaries. Although each site required manually-adjusted parameters, the outcomes were generally the same for both.

DEM

We began by creating Digital Elevation Models (DEMs) from UAV LiDAR point clouds of sparse canopies. The Barley DEM (Figure 11) depicts the depressions and rises throughout the site and identifies a tillage ridge - an old field boundary - running W to E along the top quarter of the map. This $0.6\ m$ resolution description of site topography provides a reference for h and helps us interpret f_C, LAI_e, and ET_R.

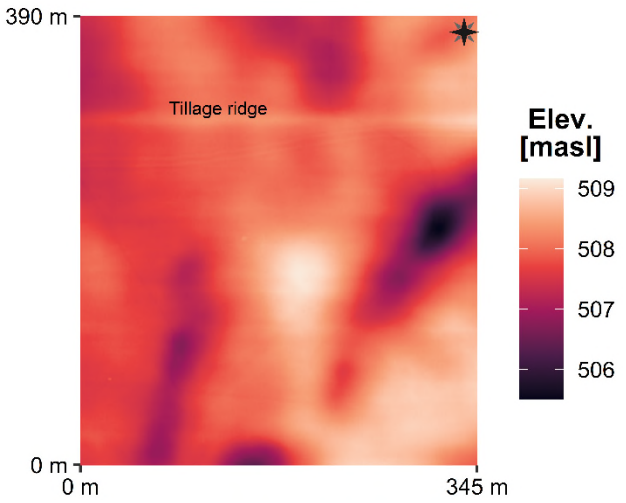

Figure 11. Barley field DEM from UAV LiDAR at $0.6\ m$ resolution
A tillage ridge (old field boundary) is revealed in the DEM, shown as a horizontal lighter-coloured line

Canopy height

The canopy height models (h) generally agreed with field-average observations (Barley sample shown in Table 2). First attempts to relate observations with h failed ($R^2 < 0$, not shown) partly because of a lack of observed variation and systematic differences between aerial and ground-based canopy height estimates. Nonetheless, we applied uniform scaling to match the average field values. The correction was proportionally larger and positive for sparse canopies ($80 - 82\%$ increase over unscaled mean height) than for fuller canopies ($0 - 15\%$ decrease).

Table 2. Field-average canopy height correction at Barley

Date	$\boldsymbol{h}$ mean unscaled [$\boldsymbol{m}$]	$\boldsymbol{h}$ mean scaled [$\boldsymbol{m}$]	$\boldsymbol{h}$ mean change [$\boldsymbol{m}$]
18_207	0.76	0.65	-0.11
19_177	0.10	0.18	0.08
19_184	0.13	0.23	0.10
19_212	0.73	0.70	-0.03
20_210	0.83	0.84	0.00

The UAV-LiDAR derived h maps depict patterns consistent with RGB imagery for sparse and full canopies (Figure 12). Over sparse cover (19_184), green patches of canopy emergence coincide with taller h (in yellow). Furthermore, the alternating diagonal patterns in Figure 12a mimic known tillage rows in the field. In the later image (19_212) comparison (Figure 12c-d), we see that the RGB only partially explains the h pattern: with the bare road, gravel pads, and N to S tractor tracks evident in both. The unexplained taller canopy patches in h are accounted for in the DEM depressions from Figure 11. From a field observer's point of view, this phenomenon was viewed with the crop growing to a seemingly level plain that belied the actual ground surface.

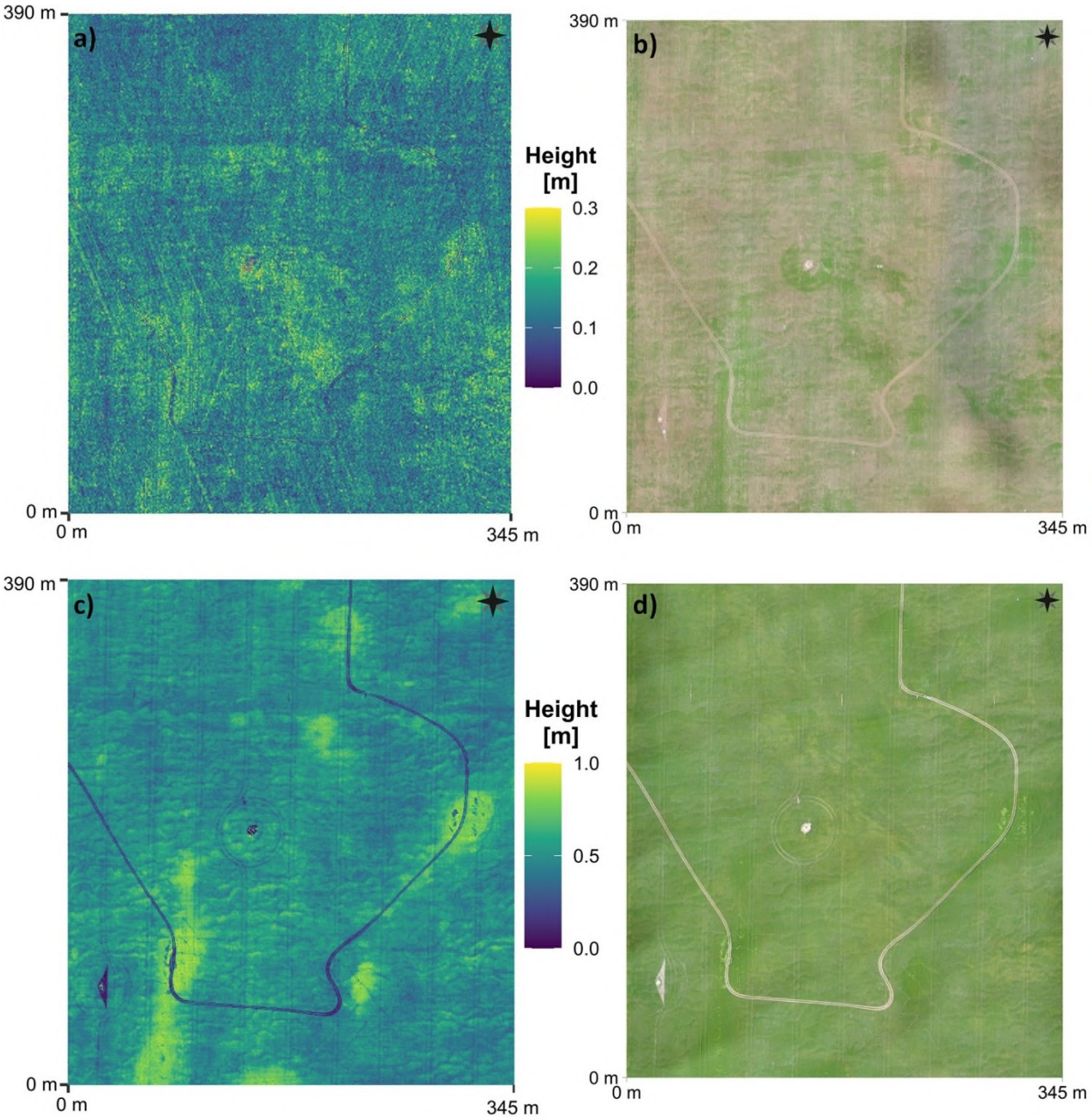

Figure 12. UAV LiDAR barley canopy structures
a,b) sparse canopy (19_184) and c,d) full canopy (19_212) conditions

LAI_e and f_c

A calibration regression of UAV LiDAR LAI_e with LAI observations yielded low R^2 but achieved acceptable $RMSE$ (Table 3). Dedicated LAI (measured over a one-metre-squared area instead of along a five-metre transect) at Barley 20_210 had a good comparison ($R^2 = 0.81$) even though it contained the fewest number (10) of observations. Meanwhile, over a similar canopy (19_212), the more numerous undedicated observations failed to match LAI_e. This implies that the spatial

uncertainty of our observations exceeded the LAI contrast present in the field. To compensate indeterminate R^2 values, κ_c was adjusted $(0.5 - 1.0)$ until the average LAI_e matched average field LAI. This solution anchors LAI_e within $RMSE$ of $0.08 - 0.82\ m^2 m^{-2}$, consistent with similar studies (Nie et al. 2016). Solutions for f_c are contained with in the LAI_e formulation, so their performance was assumed to be consistent with that of LAI_e.

Table 3. LAI regression parameters

Date [YY_DDD]	Average point density $[pts\ m^{-2}]$	Canopy cut-off height $[cm]$	κ, Extinction coefficient	Number of observations	Dedicated observations? [yes/no]	R^2 (explained variance)	$RMSE$ $[m^2 m^{-2}]$
Barley							
18_207	44.6	20	0.8	0	-	-	-
19_177	68.6	5	0.5	20	no	-2.56	0.08
19_184	73.1	5	0.5	20	yes	0.12	0.56
19_212	66.3	20	0.6	32	no	-1.2	0.81
20_210	73.2	20	0.5	10	yes	0.82	0.48
Forage							
19_177	77.6	5	0.75	15	yes	0.31	0.33
19_184	89.0	5	1.0	23	yes	-0.31	0.53
19_212	81.3	10	1.0	40	no	-1.92	0.52
20_210	85.6	5	0.9	0	-	-	-

To fill areas of the f_c and LAI_e maps where UAV LiDAR could not penetrate the dense canopy, we relied on our gap-filling procedure with h (Figure 13). A sigmoidal curve regression allowed smoother gap-filling (Figure 13b and 13e) with better R^2_{adj} than a regular linear model (Appendix A6) and also capped LAI_e at realistic values $(6 - 8\ m^2 m^{-2})$. The gaps coincide with low-spots in the DEM (Figure 11) and N to S tractor seeding paths; this also happens to be where SEB dependency on LAI_e and f_c is expected to plateau (over full canopies). Since gap filling was only needed for $LAI_e \gg 1\ m^2 m^{-2}$, the relative impact of $RMSE$ on these larger LAI_e is diminished.

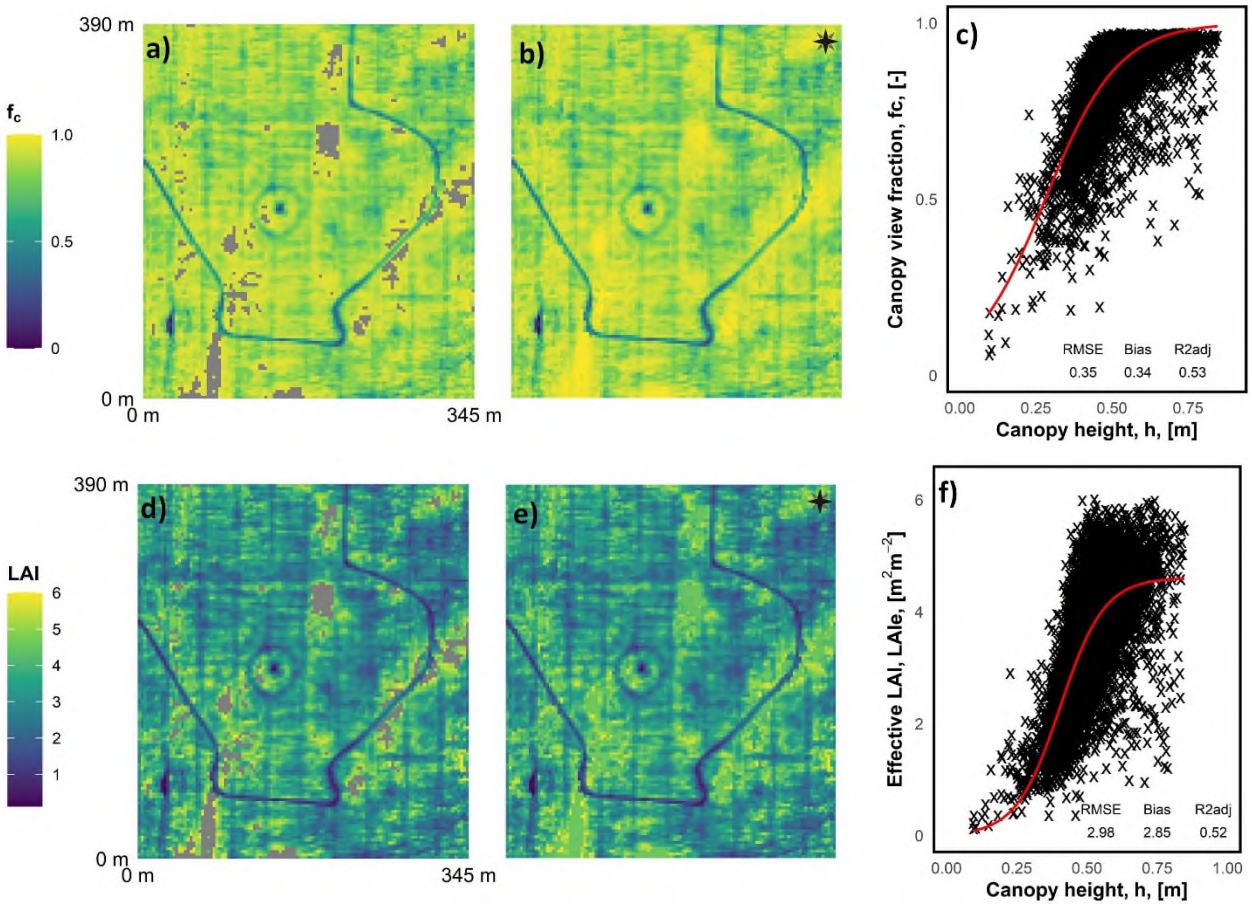

Figure 13. Gap-filling procedure for f_c and LAI_e
a-c) f_c and d-f) LAI_e with sigmoidal curve fitting regression (Barley, 19_212)

A field morphology summary (Table 4) documents key differences between the two sites. Whereas Barley shows a solid seasonal growth trend, Forage experiences relatively subtle changes in LAI_e, h, and f_c. The range of Barley LAI_e proceeds from 0.2 m^2m^{-2} early in the season to $2.7 - 5.1$ m^2m^{-2} by the end of July. There is also a dramatic increase in Barley vegetation in the 2020 collection than at similar times in 2018 and 2019, which may have resulted from increased available moisture in the 2020 season (Figure 9). Conversely, Forage demonstrates relatively modest canopy structure changes over the season. This fact reflects the asynchronous phenology stages and root structures in the grass and alfalfa cultivars at Forage.

Table 4. Field morphology summary of average field values

	Barley			Forage		
ID	LAI_e	h $[m]$	f_c	LAI_e	h $[m]$	f_c
18_207	2.5	0.65	0.85	-	-	-
19_177	0.2	0.18	0.11	1.1	0.51	0.54
19_184	0.4	0.23	0.18	1.3	0.61	0.68
19_212	3.4	0.70	0.85	1.7	0.70	0.78
20_210	5.1	0.84	0.92	1.0	0.17	0.59

Challenges with UAV LiDAR

An interpretive issue arises when using UAV LiDAR to acquire h over sparse canopies. We found that our 95^{th} percentile aggregation of canopy-classified points led to an 80% underestimation compared with ground-level observations. The reason is that in sparse canopies, the aerial-view LiDAR is more likely to measure h along the plant stem than it is to measure the top; whereas, in full canopies, more returns are likely made from the top matt of vegetation. This poses a challenge for integrating UAV-LiDAR h with empirical relationships derived using conventional crop height estimates. In response, it is prudent to correct h estimates from sparse canopy UAV LiDAR.

Relating handheld LAI observations to sub-metre UAV observations is notoriously tricky due to spatial variation in heterogenous landscapes (Nassar et al. 2022). Our efforts met similar resistance, with strongly clumped canopies garnering negative R^2 (Table 3) and worsening results when changing the calculation resolution (Nie et al. 2016). Although our LAI sampling strategy provided representative field-scale values, it struggled to spatially relate with three-metre resolution UAV LiDAR. This is partly due to a relatively large LAI sampling uncertainty compared to the range of observations. Considering that previous successes with this approach applied to taller vegetation - maize (Nie et al. 2016) and trees (Richardson et al. 2009), we suspect that attempts over young field crops may not provide sufficient contrast. Alternatively, we suggest improving the observation technique. Following Nie et al.'s (2016) approach, LAI observations could be limited to diffuse light conditions only (sunset, sunrise, or overcast). Doing so would bypass assumptions about canopy leaf structure and increase the measurement consistency.

We sough to use UAV LiDAR for acquiring physically-based canopy characteristics at resolutions consistent with UAV thermal remote sensing. Resultant h, LAI_e, and f_c reflected actual field conditions, and their magnitudes were consistent with field observations. Furthermore, the associated growth patterns coincided with high-resolution RGB imagery and DEM topography.

3.7.3 Applying UAV thermal

Practical considerations using thermal corrections

Attempts to perform atmospheric corrections using the 'vicarious calibration' method had mixed results. In many cases, field observations did not capture a sufficiently contrasting temperature range to succeed with the correction. We specified a successful correction as one that produced temperatures with $RMSE$ less than $5\ °C$ (FLIR Vue Pro R and ThermoMAP absolute accuracy). In terms of spectral radiance (Table 5), this corresponded to corrected $RMSE$ less than 0.4

$W\ m^{-2}sr^{-1}\mu m^{-1}$ and $R^2 > 0.67$. The three successful applications were at Barley: 19_177_e_4, 19_212_h_3, 20_210_h_1, with $RMSE\ (R^2)$ of $0.28\ (0.77)$, $0.17\ (0.90)$, and $0.40\ (0.67)$, $W\ m^{-2}sr^{-1}\mu m^{-1}$ respectively. We observed that atmospheric influences were greater in the early season, with L_U in 19_177_e_4 twice as high and τ half as much compared to 19_212_h_3 and 20_210_h_1. This implies that atmospheric corrections are more important to consider earlier in the season when there is greater atmospheric water vapour.

Table 5. Atmospheric corrections

Flight [YY_DDD_ID]	# Obs. [-]	R^2 [-]	r (p-value) [-]	$RMSE$ [$W\ m^{-2}sr^{-1}\mu m^{-1}$]	Upwelling spectral radiance, L_U [$W\ m^{-2}sr^{-1}\mu m^{-1}$]	Transmissivity, τ [$W\ m^{-2}sr^{-1}\mu m^{-1}$]
18_207_e_1	-	-	-	-	-	-
19_177_e_1	14	0.15	.39 (0.16)	0.34	8.34	0.16
19_177_e_4	10	0.77	.88 (<0.001)	0.28	6.62	0.35
19_177_h_1	16	0.27	.52 (0.037)	0.29	6.37	0.3
19_184_h_1	-	-	-	-	-	-
19_184_h_4	22	0.08	.28 (0.19)	0.77	8.06	0.23
19_184_h_5	23	0.36	.60 (0.002)	0.52	5.92	0.38
19_212_h_1	24	0.14	.37 (0.066)	0.39	6	0.36
19_212_h_3	12	0.90	.95 (<0.001)	0.17	1.35	0.92
20_210_h_1	8	0.67	.82 (0.013)	0.4	3.5	0.68
19_177_e_2	11	0.16	.40 (0.23)	0.51	12.83	-0.29
19_177_e_3	14	0.06	.24 (0.39)	0.92	9.02	0.11
19_184_h_2	-	-	-	-	-	-
19_184_h_3	19	0.03	.17 (0.48)	0.6	8.4	0.1
19_184_h_6	14	0.23	.48 (0.12)	0.51	6.63	0.29
19_212_h_2	26	0.15	.39 (0.052)	0.84	7.55	0.3
19_242_h_2	14	0.24	.49 (0.075)	0.77	6.4	0.26
20_210_h_2	8	0.03	.17 (0.66)	1.19	15.46	-0.22

Combined corrections

Of the combined thermal corrections in Figure 14 and Figure 15 (for sparse (19_177_e_4) and full (19_212_h_3) canopies, respectively), those with an atmospheric correction achieved closer parity between UAV and field observations. The $\epsilon_{ensemble}$ correction shifted each measurement with the same increase and did not noticeably change R^2. Atmospheric corrections applied a uniform UAV offset (L_U) in both situations with the rotation (τ) pronounced in the early season (Figure 14). The later season image was almost parallel to field observations (Figure 15) with an $RMSE$ offset similar to the $5°C$ UAV thermal accuracy. This suggests that a ground-level camera calibration with a NIST traceable blackbody (Torres-Rua 2017) could replace the full spatial calibration in these conditions (low L_U, high τ).

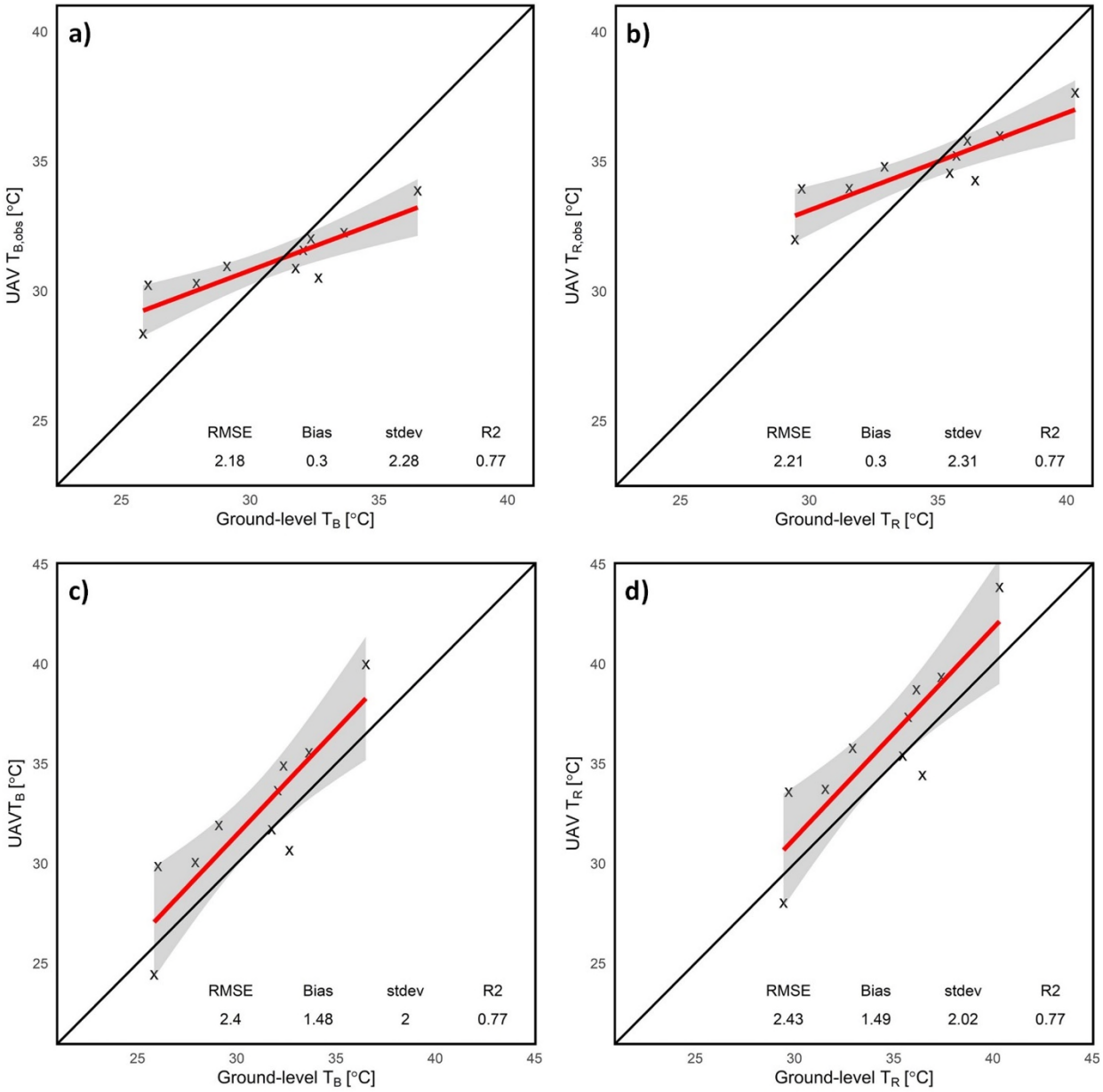

Figure 14. Incremental thermal corrections for 19_177_e_4 at Barley
a) $T_{B,obs}$, b) $T_{R,obs}$, c) T_B, d) T_R

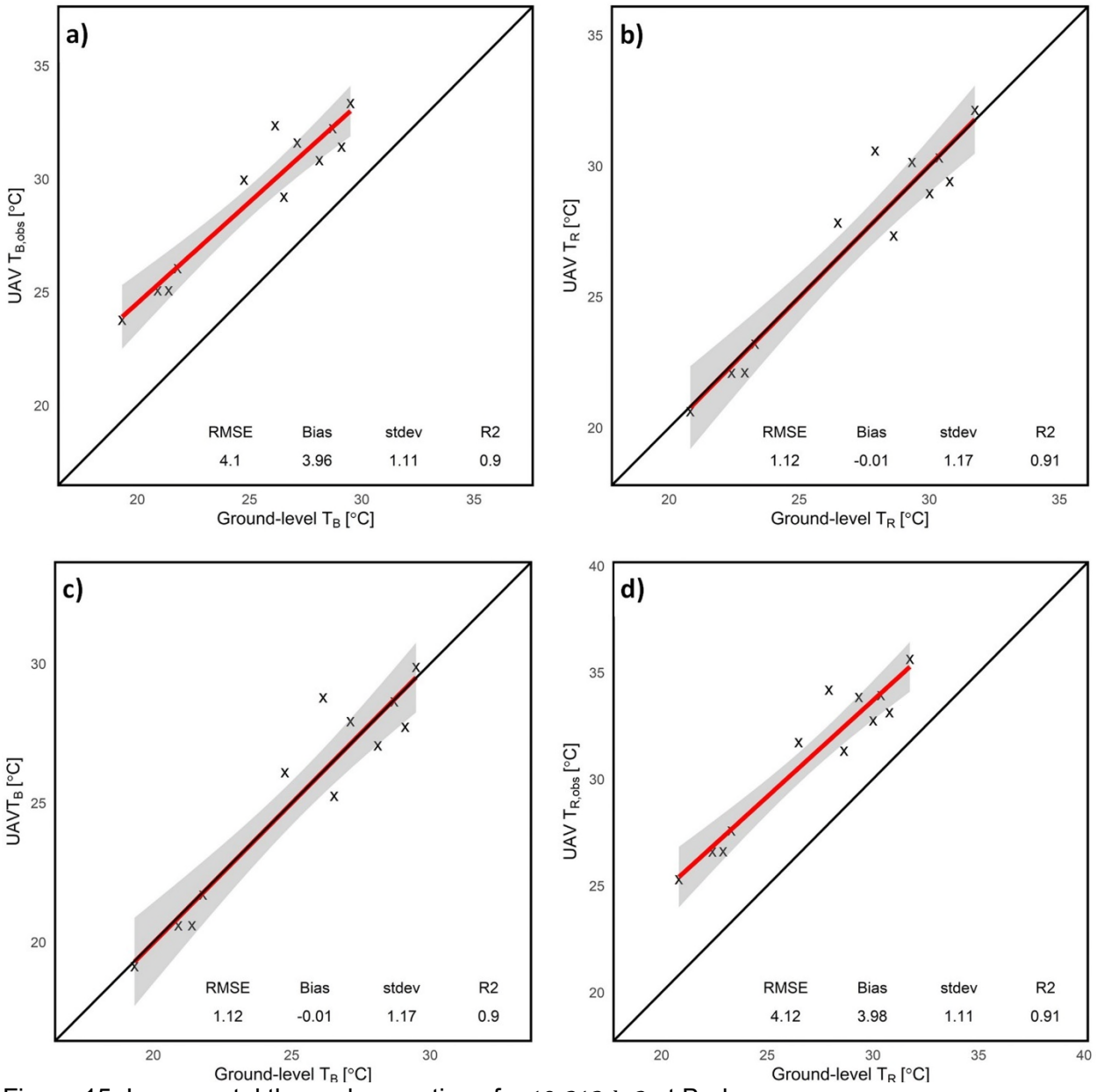

Figure 15. Incremental thermal corrections for 19_212_h_3 at Barley
a) $T_{B,obs}$, b) $T_{R,obs}$, c) T_B, d) T_R

The level of thermal correction had differing effects on statistical distributions (Figure 16). Ensemble emissivity corrections ($T_{R,obs}$) increased mean temperature for early and late images ($3.7°C$ *and* $1.9°C$ respectively) but had little effect on variability (decrease standard deviation ~$0.1°C$ for both). Meanwhile, tenable atmospheric corrections (T_B) tended to flatten the histogram (increase standard deviation) with a more pronounced standard deviation increase in early sparse canopies (~$3°C$) than in later images (~$0.3°C$). It also shifted temperature slightly to the right (~$0.4°C$ increase) in the early season image (high L_U, low τ) but strongly to the left (~$3.7°C$ decrease) in the later season image (low L_U, high τ). The combined thermal corrections (T_R)

exercised facets of both corrections; notably, the temperature shift of 19_212_h_3 (late season) was moderated between the positive shift from $\epsilon_{ensemble}$ and the negative translation from the atmospheric correction. Consequently, omitting either correction had different outcomes depending on the developmental stage of the canopy, which coincides with increasing canopy closure and lessening atmospheric effects.

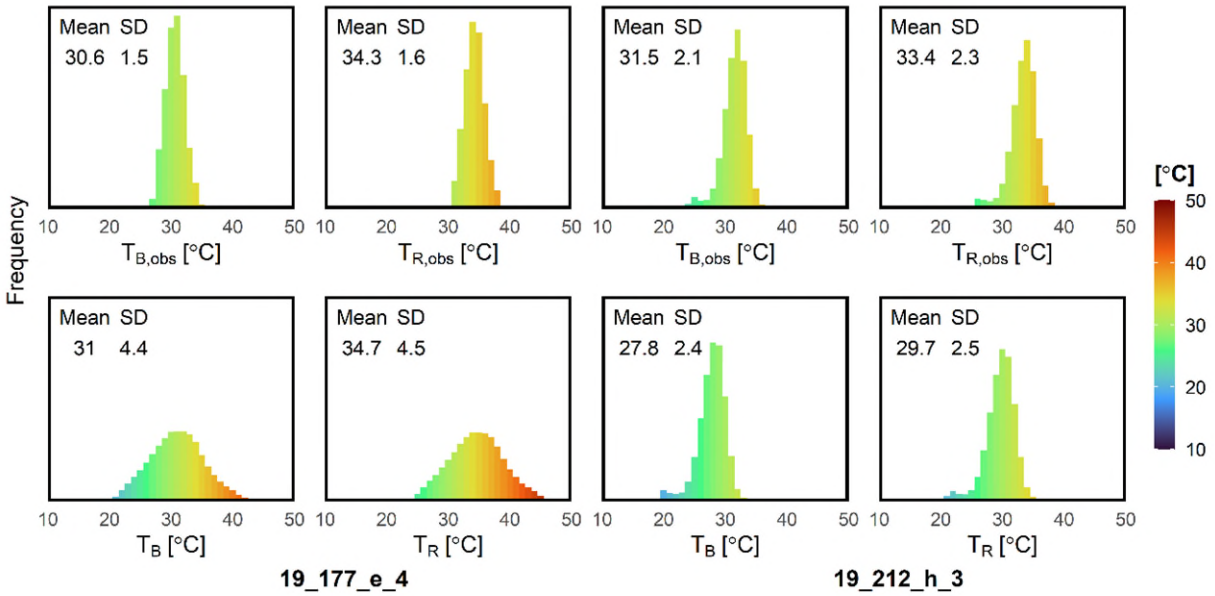

Figure 16. Sample temperature adjustment histograms

The impact of the thermal correction on spatial patterns was assessed with the modified t-test (Clifford et al. 1989, Dutilleul 1993) using $T_{B,obs}$ as a comparator. Interestingly, although thermal corrections had dissimilar histograms, their spatial correlations were virtually identical ($r > .99$, $p \ll 0.001$). The one exception at Barley with the ensemble emissivity correction of 19_184_h_1 ($r = 0.92$ $p \ll 0.001$) suggests that variable emissivity has an increased role in determining spatial thermal patterns under early morning sparse canopy conditions. Yet overall, the modified t-test indicates that atmospheric and emissivity temperature corrections have minimal impact on surface thermal patterns.

It follows that a $\pm 5\,°C$ measurement uncertainty from the UAV thermal cameras (Appendix A4) would similarly not alter the spatial patterns significantly. We assume the $\pm 5\,°C$ error acts uniformly across each image because the thermal sensors have a very fine ($0.2 - 0.04\,°C$) sensitivity one-to-two orders smaller in magnitude. Furthermore, within HRMET's Monte-Carlo error analysis, the three-by-three moving window analysis of raster information incorporates the potential spatial error (thermal standard deviation of moving window) in the results (95% confidence bounds of surface energy balance components).

Challenges with UAV thermal

We successfully applied ensemble emissivity correction to all thermal images in this study; however, certain operational challenges made atmospheric corrections only partially successful. Relying on handheld thermal observations of the terrain alone typically did not achieve strong R^2 linear regressions. Using temperature calibration plates to acquire a sufficient thermal contrast (Kelly et al. 2019) appears to be the simplest solution. Alternatively, a second UAV might be operated, hovering just above the ground (three metres, for example) to collect large quantities of concurrent sample temperatures. This would enable better ground coverage and increase the number of samples, thus improving geo-registration and sampling efficiency and avoiding the need to set up calibration plates.

3.7.4 HRMET validation with the EC method

LE time-series comparison

We compared HRMET's footprint weighted LE against an EC time series to assess the model response to changing flux (Figure 17) while using thermal input names $T_{B,obs}$, $T_{R,obs}$, T_B, and T_R to refer to their respective model outputs. The model error bounds reflect a 95% confidence interval derived from the footprint-weighted standard deviations of HRMET. Larger uncertainty bounds corresponded to quickly shifting meteorological inputs caused mainly by changing cloud cover and incoming solar radiation (Figure 10). Meanwhile, the upper and lower boundaries in the EC data reflect the degree of energy balance closure and associated closure methods (the upper boundary attributing RES to LE and lower boundary to H). During rapid meteorological changes RES becomes erroneously negative, leading to a reversal of the closure bound. We decided to retain these deprecated segments to benefit discussion of the daily flux environments.

At a glance, Figure 17 tells us that modelled LE generally agrees with the EC time series. Differences between HRMET and EC latent heat are mostly reconciled within the 95% HRMET confidence interval. A diurnal sequence is observed with Forage (2019-07-03), while Barley (2019-07-03 and 2019-07-31) captures the LE increase from morning to mid-day. HRMET also responded to sudden upward (19_177_h_1) and downward (19_184_h_5) changes in LE, albeit more strongly than the EC signal.

Seasonally, the comparison is better with earlier estimates (2019-06-03 and 2019-07-03) than with late-season estimates (2019-07-31 and 2020-07-28). The exceptions to these categories are at Forage after baling (2020-07-28) and at Barley (2018-07-26) and Forage (2019-08-30) when

prevailing cloud cover and low surface-air temperature gradients brought HRMET and EC latent heat flux into agreement (Figure 10). The cases of HRMET overestimating LE occurred later in the season when surface-to-air temperature differences reached $4-5\ °C$, and the canopy was fully developed. Considering the concurrently dry soil conditions (Figure 9) and the regional presence of saline wetlands, advection may have contributed $10-20\%$ to the total error (Alfieri et al. 2012) but leaves the remaining 50% unexplained. Furthermore, all thermal trials in HRMET gave similar LE output and did not reconcile LE discrepancy in these late season conditions.

Differences among model trials of thermal input appear to be small and systematic. The three instances where atmospheric correction was applied (19_177_e_4, 19_212_h_3, and 20_210_h_1) repeat the pattern T_B (high), $T_{B,obs}$, T_R, T_{R_obs} (low). This progression generally follows the temperature shifts in Figure 16 ($T_{R,obs}$ always highest) being inversely proportional to LE following [2] and [17]. While the trial differences are minor compared to the model overestimation in 19_212_h_3 and 20_210_h_1, they have more meaning when considering the 19_177_e_4 estimates. In this image, the $\epsilon_{ensemble}$ corrected $T_{R,obs}$ fairs closest with the bowen-ratio closure, while the atmospheric and $\epsilon_{ensemble}$ corrected T_R leans towards the lower LE residual closure bound. Given how T_R had the best radiometric alignment in Figure 14, we can infer that the LE residual closure is a truer EC flux estimate in these conditions. Thus, the thermal corrections were informative for early-season images but had limited use in late-season images when their effects were overshadowed by HRMET model error.

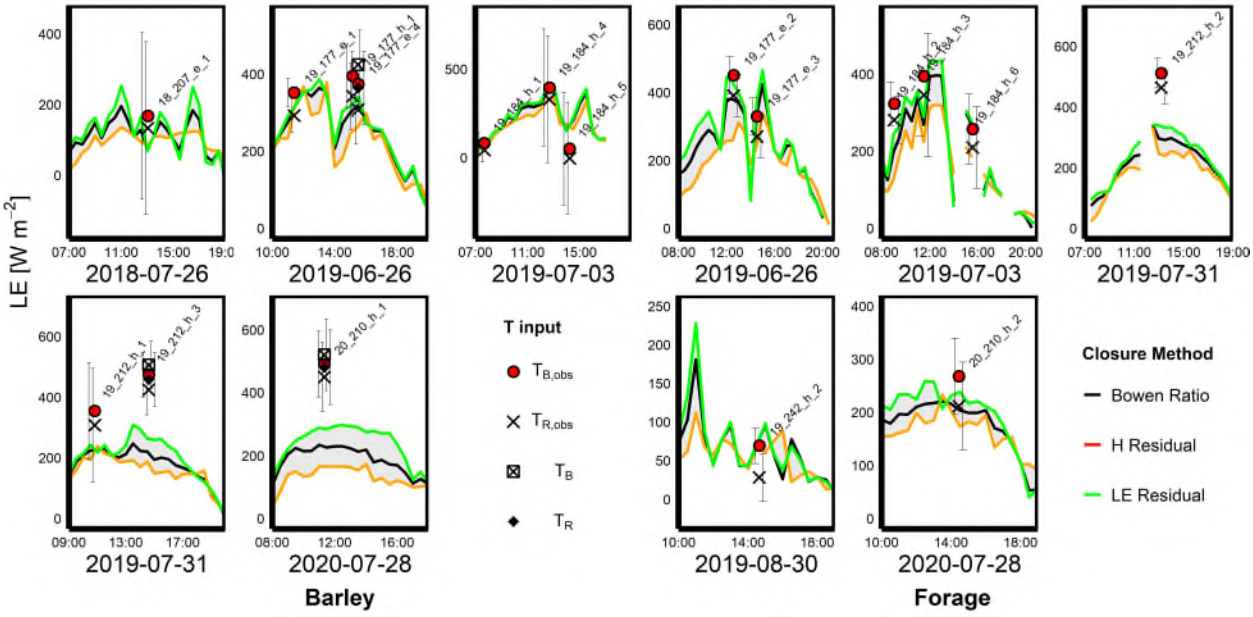

Figure 17. HRMET comparison within EC closure bounds

SEB component comparison

We separated component fluxes (Figure 18) to help diagnose LE output and reveal HRMET's modelling tendencies. We included each estimate's 95^{th} percentile error bound based on the HRMET-modelled standard deviation. Table 6 and Table 7 provide the supporting statistics: root mean squared error ($RMSE$), mean bias, standard deviation, coefficient of determination in terms of explained variance with the 1:1 line (R^2_{fit}), and a Pearson correlation coefficient (r) with significance (p). Since the atmospheric correction had only three applications, two of which were in poorly estimated late-season images, we excluded it (T_B and T_R) from the remaining analysis. The discussion follows each component separately: sensible heat (H), net total radiation (R), soil heat flux (G), and latent heat (LE).

HRMET estimates of H somewhat follow a one-to-one agreement with EC fluxes but with some exceptions. Namely, the 19-07-31 estimates at both sites and Barley 20-07-28 are all low. However, H at Barley 18-07-26 (overcast and cloudy) and Forage 20-07-28 (post-harvest) better resemble EC observations. This phenomenon may relate to HRMET's OS resistance scheme. Similar results from Troufleau et al. (1997) show that OS models underestimate H over full canopies with high surface-to-air temperature differences. The only instant of H being overestimated is at Forage (19-08-30) with a full canopy and marginal (one-degree Celsius) surface-air temperature gradient. Statistically, there is improvement in using $T_{R,obs}$ over $T_{B,obs}$ by neutralizing mean bias (-40 to $-2\ W\ m^{-2}$ at Barley and -25 to $+13\ W\ m^{-2}$ at Forage) and reducing $RMSE$ (80 to $73\ W\ m^{-2}$, Barley; 52 to $48\ W\ m^{-2}$, Forage). Excluding model variance, Barley H is poorly fit with EC observations (negative $R^2_{1:1}$); while Forage has a less poor fit ($R^2_{1:1} < 0.5$). These results are largely affected by the outliers previously mentioned.

Although R is strongly correlated at both sites ($r > .97, p < 0.001$) with a good fit ($R^2_{1:1} > 0.74$), its $RMSE$ contributions are larger than those of H ($60 - 114$ vs $48 - 80\ W\ m^{-2}$). Additionally, a $54 - 95\ W\ m^{-2}$ positive bias is present, comprising most of the $RMSE$ inflation. This presents an opportunity for updating the radiation partitioning scheme, as informed by Anderson et al. (2005) and (Colaizzi et al. 2012b). Inconsistent measurement scales are also problematic (those between the field-of-view of the net radiometer and the parcellated increments of HRMET), contributing to the total error. When considering model trials, $T_{R,obs}$ succeeded over $T_{B,obs}$ by reducing $RMSE$ by $12 - 14\ W\ m^{-2}$, bias by $13 - 17\ W\ m^{-2}$, and improving $R^2_{1:1}$ 0.74 to 0.80 and 0.84 to 0.89 for Barley and Forage respectively.

It proved difficult to relate HRMET with the soil heat flux plates. The largest outliers (19_177_h_1, 19_184_h_5 and 19_177_e_3) coincide with sudden large changes in R (Figure 10). Embedded in the results are deviations from HRMET's simplistic G interpretation (Santanello and Friedl 2003) and mismatched spatial coverages between UAV and soil heat flux plates. The observed fluxes at Barley are generally twice as much as those found at Forage. The difference lies in Forage having a scattered emergence pattern with less exposed soil, thus experiencing smaller soil temperature changes and smaller G. Differences in model trials have negligible effects on comparison statistics; however, while Barley has better goodness-of-fit and linearity metrics, the smaller quantities at Forage give it a better $RMSE$ and a reduced bias.

The LE plots in Figure 18 reiterate the outliers found in Figure 17 but depict overall model performance with greater clarity. LE mostly agreed with EC (95% confidence), except for the few late-season outliers. Of all the SEB components, LE had the highest $RMSE$ $(79 - 136\ W\ m^2)$ equivalent to $0.12 - 0.20\ mm\ hr^{-1}$ evapotranspiration at $20\ °C$. This lends to the fact that LE is estimated as a residual of the other SEB components and inherits their combined net errors. Interestingly, sometimes these errors appear to cancel out; in the 19_177_h_1 image, the excess energy in R and underestimated H are countered by a large G over-evaluation resulting in a fair LE estimate. Furthermore, the goodness-of-fit statistic is somewhat greater than that of H or G. This implies that HRMET models LE as an energy balance residual better than it models H from [18]. As a model for deriving absolute LE, HRMET achieved $RMSE$ comparable to operational models like DATTUTDUT as posted by Song et al. (Song et al. 2016b). Its capacity to derive accurate LE pattern however, is a subject of greater interest.

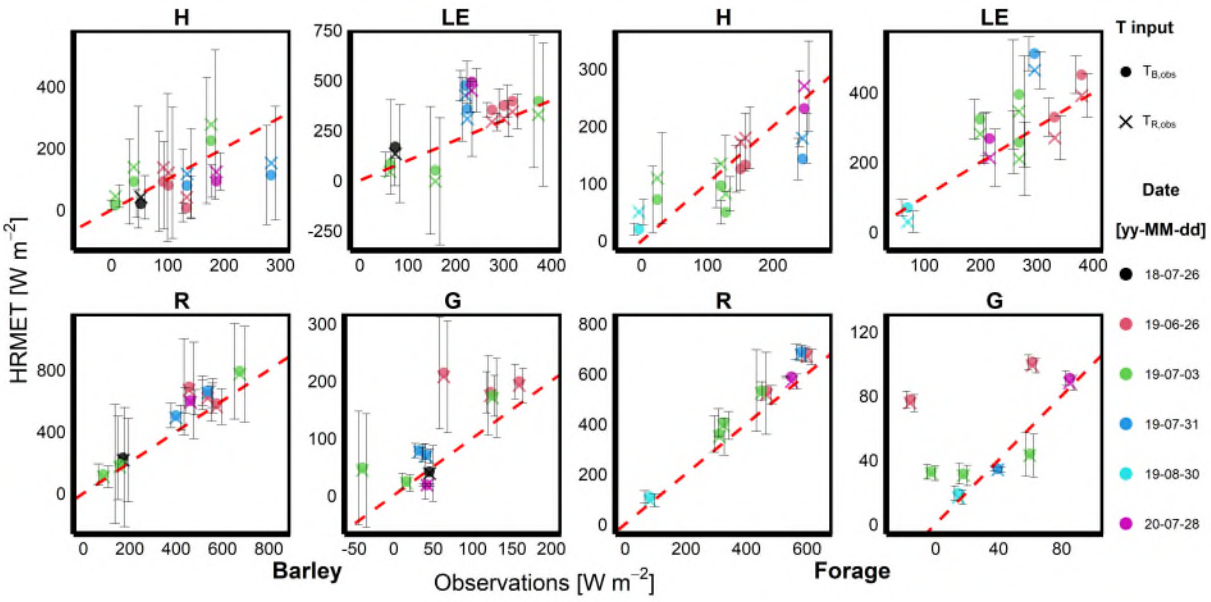

Figure 18. HRMET component evaluation with EC energy balance

Table 6. Barley HRMET component evaluation

	$\boldsymbol{RMSE}$ $[\boldsymbol{W\ m^{-2}}]$	Bias $[\boldsymbol{W\ m^{-2}}]$	Std. Dev. $[\boldsymbol{W\ m^{-2}}]$	$\boldsymbol{R^2_{fit}}$ [1:1]	$\boldsymbol{r}$ (p-value)
$T_{B,obs}$					
G	64	44	49	0.24	.77 (0.009)
H	80	-40	73	-0.8	.51 (0.130)
R	114	95	67	0.74	.97 (<0.001)
LE	136	89	108	0.16	.73 (0.017)
$T_{R,obs}$					
G	61	40	48	0.29	.78 (0.008)
H	73	-2	77	-0.20	.49 (0.150)
R	100	78	66	0.80	.97 (<0.001)
LE	113	38	112	0.40	.68 (0.029)

Table 7. Forage HRMET component evaluation

	$\boldsymbol{RMSE}$ $[\boldsymbol{W\ m^{-2}}]$	Bias $[\boldsymbol{W\ m^{-2}}]$	Std. Dev. $[\boldsymbol{W\ m^{-2}}]$	$\boldsymbol{R^2_{fit}}$ [1:1]	$\boldsymbol{r}$ (p-value)
$T_{B,obs}$					
G	39	21	35	-0.78	.45 (0.26)
H	52	-25	49	0.26	.85 (0.007)
R	72	67	27	0.84	.99 (<0.001)
LE	103	71	80	0.34	.82 (0.013)
$T_{R,obs}$					
G	38	20	34	-0.74	.45 (0.26)
H	48	13	49	0.45	.85 (0.008)
R	60	54	28	0.89	.99 (<0.001)
LE	79	21	81	0.59	.79 (0.019)

Challenges with UAV high-resolution SEB applications

Spatial and temporal inconsistences remain challenges for implementing high-resolution SEB models with UAV data. Although footprint weighting allowed us to reference HRMET outputs to bulk EC fluxes, the ancillary R and G spatial registrations remain unaccounted. Large R biasing ($54 - 95\ W\ m^{-2}$) and subsequently poor G regressions ($R^2\ < 0 - 0.29\ W\ m^{-2}$) are evidential for

improving their spatial representations. Aside from updating the radiation model (Colaizzi et al. 2012a, 2012b), we suggest exploring methods to scale R and G within the EC footprint.

Errors from comparing dissimilar measurement intervals between UAV data ($5-10\ min$) and meteorological records ($30\ min$) were mitigated in our linear interpolation strategy. However, the large uncertainty bands presented by HRMET reaffirm the difficulty of resolving instantaneous SEB processes in real-life environments. The reality of this issue limits accurate SEB use to ideal conditions of near-constant meteorology.

3.7.5 Relative evapotranspiration

Although our EC comparison revealed a limited ability to model absolute LE (specifically in full canopy conditions with high surface-to-air temperature differences), it reveals little about the spatial output patterns. These are more important for operations intending to apply ET_R indices.

ET_R differences among thermal corrections

Spatial similarities between ET_R outputs of different thermal inputs were assessed using the modified t-test (Appendix A7). This works because ET_R retains a normal distribution (albeit, with restrictions on the upper and lower bounds) like its predecessor ET. All trials were strongly correlated ($r > .93, p < 0.001$) with their respective $T_{B,obs}$-derived ET_R. Moreover, differences between $T_{R,obs}$, T_B, and T_R trials were indistinguishable for the late season images and very small for the 19_177_e_4 image ($r = .957, .960, .948$ respectively, with $p < 0.001$). These findings suggest that $\epsilon_{ensemble}$ and atmospheric corrections had negligible effect on ET patterns.

We consider how the HRMET code and the derivation of ET_R might mask thermal spatial adjustments. Since HRMET was intended for daytime use, it limits large negative LE values to $-100\ W\ m^{-2}$ by default, so any changes to the temperatures at these cells may be ignored. ET_R applies further distortion by normalizing to the 2.5^{th} and 97.5^{th} percentiles. However, including these filters helps prevent intrusive artifacts (human objects, animals, litter) from influencing the results. Assuming these precautions, we conclude that ET_R is unaffected by thermal treatment, and the simplest $T_{B,obs}$ may be used.

ET_R chronologies

Since our ET_R patterns were irreverent of thermal adjustment, the $T_{R,obs}$ output was selected (simply because it had better correspondence with EC) for presenting ET_R chronology (Figure 19).

Early season images at Barley depict a low-ET ridge running W to E and a high ET circular seeding pattern around the flux tower. These agricultural effects were replaced by water-driven landscape signals later in the season. Depressions with lingering soil moisture produced higher ET_R, while road pathways and gravel patches were apparent dead zones. Interestingly, the radius around the tower subjected to increased seeding density did not maintain its high ET_R. This further indicates a moisture-limiting regime at season end. Forage progression of ET_R was less drastic than Barley. The NW wetland ET_R was lower for most of the season but increased at the end of July; this is partly due to it having feral grass species of differing phenology cycles. The post-harvest 20_210_h_2 landscape revealed areas of surplus moisture (NW wetland, the E ditch line, and interlaying depressions) accessible to plant species with deep root systems (alfalfa). Wetland perimeters (NW and SW wetlands) have consistently low ET_R (indicative of excess salinity), whereas the eastern swath, central key-shaped patch, smaller south depression, and eastern ditch line maintained high levels of ET_R throughout all images.

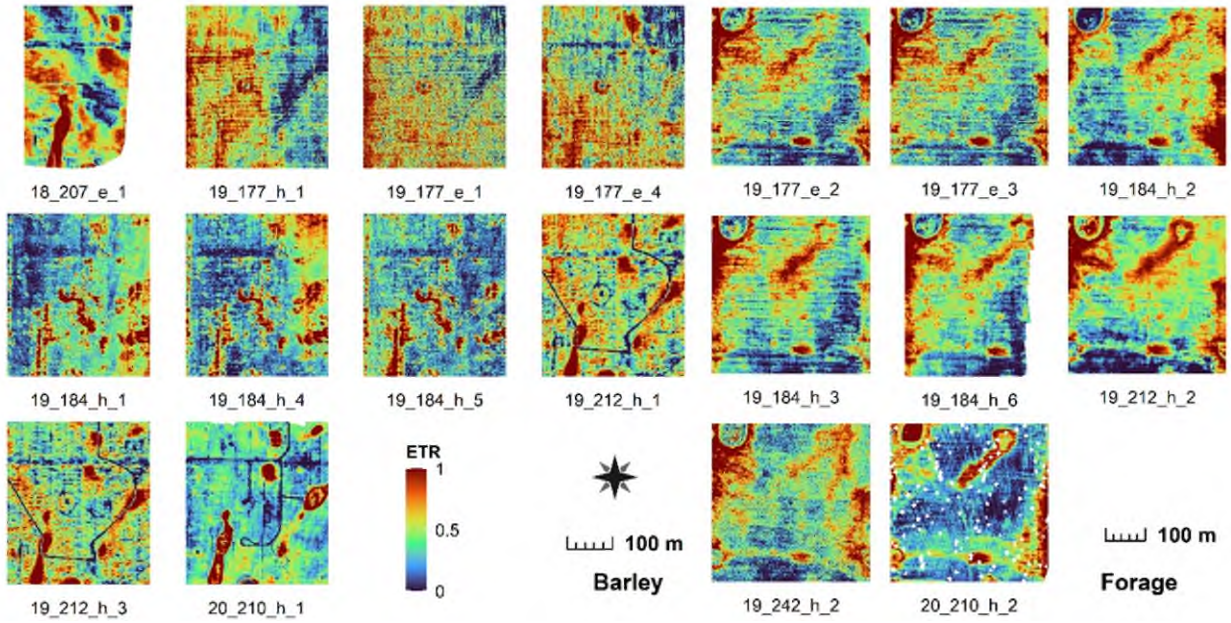

Figure 19. ET_R chronology at Barley and Forage

Note: blank patches in 20_210_h_2 are the locations of hay bales omitted from the analysis

ET_R limitations and recommendations

As a non-integer ordinal data type, ET_R alone cannot assign a quantitative weighting to ET spatial differences; however, ET_R can be used to detect ET pattern changes over time and assess relative areas of better or worse plant growth. The ability of ET_R to reveal something of the hydrological landscape highlights its potential for long-term monitoring purposes. Existing UAV methods are labour-intensive and only provide a snapshot perspective. These strategies require

ongoing surveillance restricted to flight limitations and data processing turn-around time. The ET_R index proposes an alternative strategy using carefully selected discrete images that reveal hydrological landscape traits for continual crop monitoring. Since ET_R does not contain information on the location (mean ET) and scale (standard deviation) of the spatial distribution, it is necessary to have some estimate of average ET and a spatial standard deviation. Furthermore, the representation criteria for selecting ET_R images are well open for discussion. These plans should be purpose-specific, and their application limited to the observed span of hydrological conditions. One could potentially apply these linkages to disaggregate EC footprints and footprint climatologies (Kljun et al. 2015). Some other caveats for comparing ET_R include having similar plant compositions and dry surface conditions (isolating transpiration). Overall, this study presents a case for using discrete UAV acquisitions of thermal $T_{B,obs}$ in an operational SEB model to identify intrinsic field properties based on spatial ET patterns.

3.8 Conclusion

Our research objectives were threefold: 1) to evaluate a UAV LiDAR workflow for acquiring high-resolution LAI_e, f_c, and h; 2) to study the magnitude and spatial impact of incremental $T_{B,obs}$, T_{Robs}, T_B, and T_R thermal corrections; and 3) to assess the HRMET model performance based on EC fluxes and ET spatial patterns.

The present use of UAV LiDAR was mostly successful. We were able to interpret a detailed DEM map from early season flights that helped us to acquire h maps at $0.6\ m$ and $1.0\ m$ resolutions at Barley and Forage, respectively. These h maps agreed with average field observations but required scaling over sparse canopies. We suggest this is caused by the UAV LiDAR viewing more lower stems and leaves than in full canopies. We also used a Beers-Lambert method to find f_c and LAI_e with mixed results. Estimates of f_c and LAI_e showed vegetation patterns consistent with RGB imagery and DEM topography and compared favourably to average field observations ($RMSE\ 0.08 - 0.81\ m^2m^{-2}$). Efforts to regress LiDAR LAI_e with handheld ceptometer readings, however, were less successful in terms of R^2 ($< 0 - 0.81$) but achieved good $RMSE$ ($0.08 - 0.81\ m^2m^{-2}$). We attributed the poor regression to uncertainty in our field observations and sampling protocols and the inherently smaller field variations compared to taller crops and tree canopies. We suggest that users applying the Beers-Lambert method over short vegetation ($< 0.5\ m$) increase their measurement precision by restricting ceptometer readings to diffuse light only and by averaging multiple with-row and cross-row observations within the desired LAI_e resolution area.

In addition to trialling UAV LiDAR, we examined the utility of UAV thermal corrections and their effects on temperature. The four temperature descriptions proceeded from raw blackbody brightness and radiometric temperatures ($T_{B,obs}$ and $T_{R,obs}$ respectively) to atmospherically corrected values (T_B and T_R). An ensemble emissivity correction incorporating LiDAR-derived f_c was successfully applied to all images. The $T_{R,obs}$ experienced uniform increases in mean temperature but had little impact on standard deviation. Meanwhile, the atmospheric correction (vicarious radiance regression) was only partially successful ($3/17$ flights) due to insufficient observed temperature contrasts. We imposed criteria that successful corrections have $R^2 > 0.67$ and $RMSE < 0.4\, W\, m^{-2} sr^{-1} \mu m^{-1}$. Tenable corrections ($T_B$) observed slight mean temperature increases in early season images (high L_U, low τ) and ~$3.5°C$ decreases with later images (low L_U, high τ). Moreover, early season images experienced more variability (standard deviation increased by ~$3°C$) with the atmospheric corrections. Lastly, the combined corrections (T_R) reflected both adjustments and had a moderated temperature increase when $\epsilon_{ensemble}$ and atmospheric corrections worked in opposite directions to shift the mean temperature. We found that $\epsilon_{ensemble}$ and atmospheric corrections differed depending on the canopy development stage and associated atmospheric parameters. Interestingly, modified t-tests with spatial auto-correlation corrections revealed that thermal treatments had nearly identical spatial patterns to $T_{B,obs}$ ($r > .99, p < 0.01$).

We tested HRMET's performance on barley and forage crops using 17 images collected at different daytimes across three growing seasons. The model aptly responded to diurnal patterns and sudden flux changes; however, it overestimated LE in later season images with full canopy cover (LAI $> 3\, m^2 m^{-2}$) and surface-air temperature gradients exceeding $4 - 5\ \ W\, m^{-2}$. Successful atmospheric corrections using the vicarious radiance approach (acquiring T_R) indicated an improvement with early-season LE but had little influence in later images. Ensemble emissivity corrected trials, $T_{R,obs}$, yielded closer EC agreement than T_B, but they also could not reconcile late-season LE errors. This suggests that HRMET struggles with aerodynamic-radiometric differences over hot, full canopies, similar to an OS model. Overall, HRMET replicated LE flux tower observations within $79 - 136\, W\, m^{-2}$ $RMSE$ given $T_{B,obs}$ and $T_{R,obs}$ thermal inputs.

Irrespective of absolute accuracy, we assessed HRMET's ability to capture ET spatial patterns in the form of the ET_R index. We applied the same modified t-test as performed on the thermal corrections and found that all ET_R trials were spatially consistent with the $T_{B,obs}$ ET_R ($r > .93, p \ll 0.001$). These findings imply that a $T_{B,obs}$ is equally effective as $T_{R,obs}$, T_B and T_R at capturing ET spatial patterns. Moreover, a site ET_R chronology reflected site hydrological changes and the

expected stress patterns. Consequently, we propose that ET_R maps derived from uncorrected $T_{B,obs}$ can be useful to SEB users who are concerned primarily about spatial patterns of ET and their linkages to a changing hydrological environment.

4 DISAGGREGATING EDDY-COVARIANCE FOOTPRINTS USING UAV EVAPOTRANSPIRATION PATTERNS

4.1 Preface

Now in this section, we reach the intended application of our study: to disaggregate eddy-covariance footprints using UAV high-resolution ET patterns. We start with the ET_R maps from Section 3.7.5 and ascribe them to EC data timelines using the introduced concepts of ET period and an ET combination method. Proceeding with Kljun et al.'s (2015) footprint parameterization, we applied our disaggregation method (disFFP) to individual footprints and climatologies. This section presents our disFFP method, showing how it reallocates flux in agreement with local flux features. Furthermore, we commend disFFP as a tool for EC researchers to interpret continuous flux footprint monitoring using discrete UAV-acquired ET_R.

4.2 Abstract

Surface-atmosphere flux measurements enable the study of regional climates and localized energy balances. Direct flux measurements, using the eddy-covariance (EC) technique with short towers (less than three-metres), provide bulk values from a spatially aggregated source area (footprint). Additionally, variable landscape features within the footprint contribute to the overall flux measured at the instrument. Often, these source contributions are identified with some surface property or land classification for purposes of assessing flux tower representativeness or for regional upscaling. Contrarily, this study intends to disaggregate EC footprints using high-resolution maps of evapotranspiration (ET).

The rise of surface energy balance models driven by high-resolution thermal imagery presents new opportunities for land-atmosphere interaction research. Namely, sub-metre resolution ET patterns measured from unoccupied aerial vehicles (UAVs) may be used to disaggregate coinciding flux footprints. Furthermore, ET patterns may be ascribed to distinct flux intervals using flux rate, coefficient of variation, phenology timing, and hydrological characterizations and used to interpret entire seasonal or multi-seasonal climatologies of amalgamated footprints. Coupled with a validated parameterization of the backwards Lagrangian stochastic dispersion model, the following disFFP footprint disaggregation framework is proposed.

In the present study of an unirrigated barley field in a semiarid continental climate, five ET estimates from 2018-2020 were used to disaggregate EC source areas using the proposed disFFP method. Disaggregated results were compared with vegetation patterns and topography (proxies for access to soil moisture). The resultant footprint maps showed flux assignment changes of up to $\pm 9\%$. It is expected that disFFP would have even stronger impacts on taller towers encompassing a larger footprint area. The novel ET period and ET combination method added new insights to the EC bulk ET flux ($144\ mm$) by mapping a smaller portion ($90 - 120\ mm$) to pathways and gravel pads and revealing that the high-ET landscape depressions contributed 38% higher fluxes ($180 - 200\ mm$). This affirms the potential of using discrete UAV images to disaggregate continuous EC monitoring.

4.3 Introduction

Quantifying surface-atmosphere interactions is fundamental to meteorology. Application scales range from large eddy circulation patterns in the convective boundary layer to micro-scale diffusion across plant stomata. A common tool to measure turbulent fluxes at the field scale ($0{:}\,200 - 1000\ m$) is the eddy-covariance (EC) method. This method provides a bulk flux measurement over an area that can be described using a footprint model. However, understanding the source heterogeneity throughout the footprint requires additional information. High-resolution remote sensing may provide a direct way to disaggregate EC footprints of evapotranspiration (ET) based on a relative pattern ET index (ET_R). Still, the temporal incongruity between continuous EC and discrete remote sensing presents a confounding issue.

4.3.1 Eddy-covariance footprints

The EC technique is a benchmark for measuring land-surface interactions (Baldocchi et al. 2001). This non-destructive, non-intrusive approach is used to measure scalar quantities and trace gases (Eugster and Merbold 2015). Eddy-covariance provides continuous flux observations representative of a fetch of weighted contributions (aka flux footprint). Here the terms ‘flux footprint’ or ‘footprint’ are analogous to the ‘source weight function’ (Schmid 1997), meaning the spatial distribution of flux values from the ensemble of contributing surface sources. It can also be re-interpreted as percentage isopleths of the summed footprint function within a domain of interest (ex. 80% of the measured flux). Methods for estimating tower-based source areas vary in complexity: from the empirical 100:1 rule of thumb (Burba 2013) to analytical K-theory models (Horst and Weil 1992), to Lagrangian statistical techniques (Kljun et al. 2002), to higher-order

closure numerical models, large eddy simulations, and various hybrid approaches (Leclerc et al. 2014). Among these, the backwards Lagrangian stochastic dispersion model and its latest parameterized form - Flux Footprint Prediction (FFP) - (Kljun et al. 2002, 2015) share an optimal balance of accuracy and ease of use.

4.3.2 Climatologies

Although footprint modelling is framed around discrete EC averaging periods (where flow stationarity is assumed valid), it is often more useful to superimpose a series of footprints into a single climatology footprint. Within the FFP code, climatologies are created by treating each constituent footprint with equal weighting (Kljun et al. 2015). We refer to this type of climatology as a 'combination by occurrence'. It tells the user 'where' the flux likely came from at any given time in the record. Unfortunately, this description gives misleading results when the user is concerned about quantifying flux contributions over a time of changing emission rates due to seasonality and crop phenology (Wizemann et al. 2014). A 'combination by contribution' climatology - used in the present study - provides an alternative approach for synergy between EC bulk measurements and footprint disaggregation strategies.

4.3.3 Footprint disaggregation

Interpreting EC fluxes over heterogeneous landscapes requires addressing the topic in two ways. First, there is the aerodynamic interpretation of heterogeneity, where surface features manipulate the turbulent flow fields. This situation compromises EC assumptions of a constant rate vertical flux and a negligible horizontal divergence (Eugster and Merbold 2015). Turbulent heterogeneities are typically expressed as abrupt changes in momentum roughness length (Barcza et al. 2009, Heidbach et al. 2017), scalar roughness lengths (Klaassen et al. 2002, Joy and Chávez 2021), advection (Alfieri et al. 2012), and secondary circulations (Markkanen et al. 2003). The classic 'small perturbation' assumption by Schmid (2002) uses references-of-scale to minimize aerodynamic heterogeneity if the measurements are taken above a certain blending height (about equal to the roughness sub-layer height) where the flow is well mixed and representative of the landscape. This concept of 'representativeness' was also defined by Schmid (1997) as a metric to assess whether an EC tower location's footprint contained features sufficiently similar to the region of interest. Thus, the problem of aerodynamic heterogeneity is typically resolved in the placement of the EC tower to allow simplifying assumptions about the flow field.

The second type of heterogeneity involves variable scalar emissions intrinsic to the properties of the landscape. Although these variable sources (or sinks) cause the scalar turbulence differences of the first type (aerodynamic), they remain embedded in the EC flux even when the flow assumptions are valid (Schmid 2002). It is the topic of ongoing research on how to interpret this second type (source) heterogeneity from the bulk flux measurements entrained in EC footprints.

Various explanatory variables have been proposed to interpret intra-footprint source variations: canopy structure and digital elevation models for ET (Sutherland et al. 2014, 2017), thermal remote sensing environmental respiration (ER) (Kelly et al. 2021), surface temperature and soil moisture proxies for sensible heat (H) and latent heat (LE) respectively (Anderson and Vivoni 2016), enhanced vegetation index (EVI) proxy for gross primary production (GPP), net ecosystem CO_2 exchange (NEE) and ER (Wagle et al. 2020), remote sensing GPP models (Gelybó et al. 2013), land cover classifications (LCC) (Göckede et al. 2006, Kirby et al. 2008, Barcza et al. 2009, Hutjes et al. 2010, Peng 2015, Xu et al. 2017); and multivariate combination methods for deciphering carbon assimilation (Griebel et al. 2016), methane fluxes (Reuss-Schmidt et al. 2019, Tuovinen et al. 2019, Levy et al. 2020) and H and LE fluxes (Metzger et al. 2013).

These relationships are typically derived from various forms of spatio-temporal analysis. Linear regression methods are common for comparing footprint aggregated explanatory variables with bulk EC fluxes over time (Sutherland et al. 2014, Anderson and Vivoni 2016) and for assigning LCC contributions from overlapping footprints (Hutjes et al. 2010, Peng 2015, Xu et al. 2017); whereas, a multivariate analysis represents an alternative approach using multi-level modelling (Levy et al. 2020) and machine learning (Metzger et al. 2013). Generally, the purpose of spatio-temporal analysis is to qualify footprint representativeness in the site environment (Göckede et al. 2006, Barcza et al. 2009, Reuss-Schmidt et al. 2019) or to characterize the regional flux using the retrieved relationships with a continuous surface variable or LCC (Metzger et al. 2013, Tuovinen et al. 2019, Levy et al. 2020).

Although it has been shown that higher resolution flux aggregations compare best with EC bulk measurements (Sutherland et al. 2014, 2017, Anderson and Vivoni 2016, Wagle et al. 2020), the spatially variable source fluxes have seldom been known *a priori* and used explicitly to manipulate the flux source area. One example of this (known to the authors at the time of writing) is Gelybó et al. (2013), who used downscaled FPAR (fraction of photosynthetically active radiation) to weigh GPP contributions within a daily climatology and achieved improved comparisons with EC-derived bulk GPP. The desire to disaggregate intra-footprint source heterogeneity using high-resolution

spatial flux interpretations has been alluded to by various authors (Kljun et al. 2015, Wagle et al. 2020, Kelly et al. 2021) and is an objective of the present work.

4.3.4 Evapotranspiration modelling from thermal remote sensing

High-resolution ET modelling with unoccupied aerial vehicles (UAVs) provide a unique opportunity for disaggregating EC footprints. Although EC is commonly used to validate such models (Song et al. 2016a, Xia et al. 2016, Nassar et al. 2021), thus far, the flux patterns from high-resolution ET modelling have not been used to re-allocate EC source areas.

The ET_R product by Zipper and Loheide II (2014) poses an intuitive solution for capturing spatially variable ET patterns (normalizing the 2.5^{th} and 97.5^{th} percentiles between 0-1). It does this using sub-metre thermal remote sensing to drive a surface energy balance model - HRMET - and resolve ET as a residual. Although ET_R originated as a tool for delineating management zones for precision agriculture, the same tool has the potential to disaggregate ET footprints. Particularly, we wonder if ET_R can disaggregate not only concurrent EC footprints but further be used to interpret longer-term climatologies based on inferred relationships with flux rate, phenology, and season (Wizemann et al. 2014, Reuss-Schmidt et al. 2019, Ohana-Levi et al. 2020).

4.3.5 Segmenting observation periods

Various criteria have been proposed to select footprints for climatology amalgamation. These include using spatial bias stabilization times (Kim et al. 2006), atmospheric stability regimes (Göckede et al. 2006), dominant seasonal wind patterns (Griebel et al. 2016), methane flux rates (Reuss-Schmidt et al. 2019), and phenology and climate (Wizemann et al. 2014). Ohana-Levi et al. (2020) showed that soil-type management zones could be inferred using seasonal or multi-seasonal spatial ET. Furthermore, they show that ET growth patterns are inextricably linked with landscape properties and soil moisture. This implies that the spatial information embedded in ET_R and coincident ET coefficients of variation are representative of a period of like flux patterns and environmental conditions. This ‘ET period’ may then be matched with a coinciding EC climatology representing the same period. By exploring this connection between ET_R and the flux environment, it is possible to use discrete remote sensing ET observations for interpreting continually-monitored EC climatologies.

4.3.6 Objectives

The objectives of the present study are to:

- Propose a disaggregated form (disFFP) of Kljun et al.'s (2015) Flux Footprint Prediction (FFP) parameterization using ET_R from the High-Resolution Mapping of EvapoTranspiration (HRMET) model (Zipper and Loheide II 2014) for a single footprint
- Explore ET period selection for linking discrete spatial ET information to eddy-covariance ET climatologies
- Apply disFFP to disaggregate seasonal and multi-seasonal climatologies

4.4 Data and methodology

4.4.1 Data collection

Area of study

We monitored a barley field near Saskatoon, Saskatchewan (Canada), during the 2018-2020 growing seasons. The continental climate experiences annual temperature swings averaging from $-37\ °C$ to $34°C$ and receives $350\ mm$ of precipitation annually (Government of Canada 2021). The field lies in a glaciolacustrine plain that is slightly undulating ($< 2\%$ slopes) with ephemeral wetlands (Ellis et al. 1970). Dark brown chernozem of a fine sandy loam texture characterizes the soil. During this study, the environment was severely (2018) to moderately (2019-2020) dry (Figure 20) based on an annual standard precipitation index (SPI) spanning the prior 50 years using data from local weather stations (Government of Canada 2021).

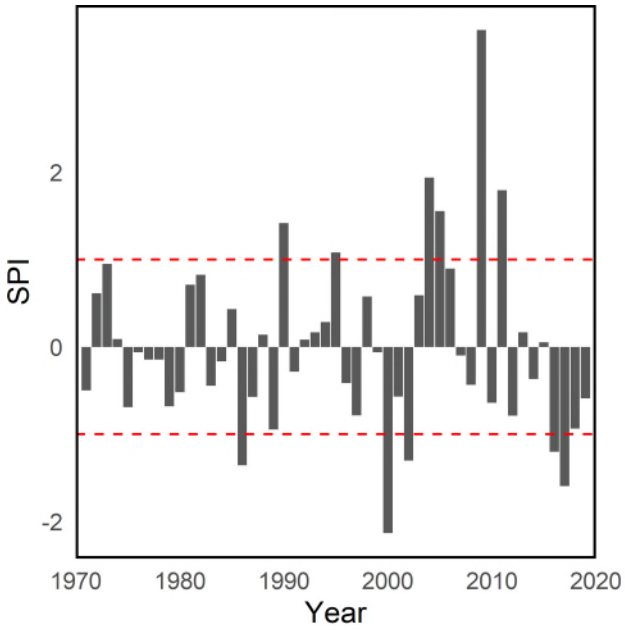

Figure 20. Saskatoon annual SPI over 50 year period
Red horizontal dashed lines indicate upper and lower 'normal' bounds. (data from the Government of Canada (2021) meteorology website database)

Flux Tower

Each year we set up a portable EC flux tower with accompanying meteorology instrumentation (Figure 21). A LI-COR 7500A open path gas analyzer with Campbell Scientific CSAT3 sonic anemometer ($20\ Hz$) was used to measure LE at $30\ min$ averaging intervals from a height of $2 - 2.5\ magl$. Accompanying $30\ min$ meteorology records included: additional wind speed (05103-10, R.M. Young), four-component net radiation (CRN1, Kipp & Zonen), air temperature and humidity (HMP45C212, Vaisala), surface infrared temperature (SI-121, Apogee), rainfall (TE-525M, Texas Electronics), soil heat flux (HFP01, Hukseflux), and $0.10\ m$ and $0.20\ cm$ soil moistures and temperatures (CS650, Campbell Scientific). The influence from the adjacent groundwater observation well pad was mitigated by positioning it away from the prevailing NWW-SEE winds observed by the tower.

Figure 21. Eddy-covariance meteorological station at the barley field

Flight Schedule

Fluxes were continuously monitored from May to September, yet we flew UAVs only on select days. While the 2018 and 2020 seasons have just one late-season flight each, 2019 was monitored throughout its phenological progression from tillering to head-filling stages. This progression is shown in Figure 22 using RGB imagery and ground-level photographs of the general site.

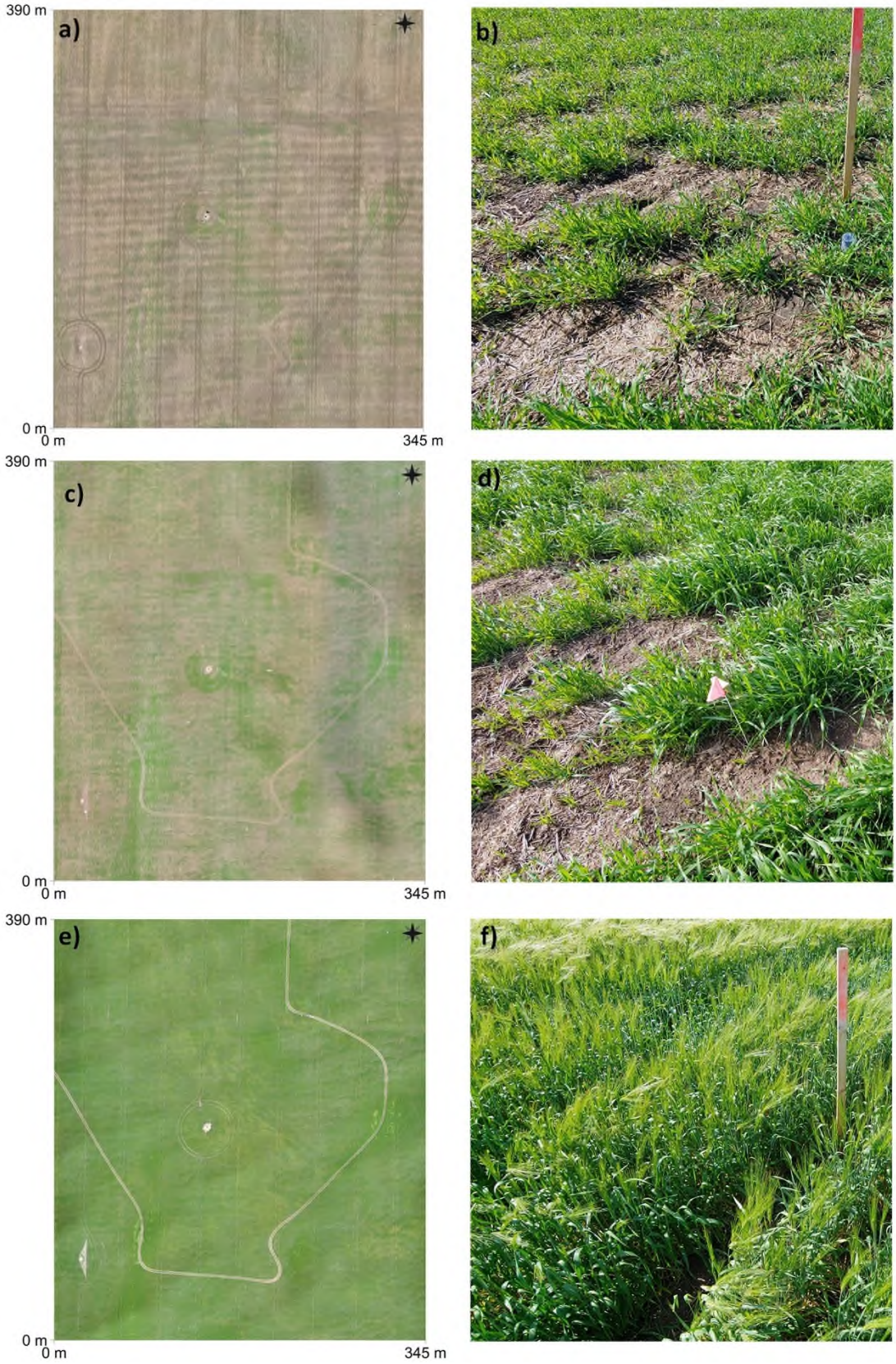

Figure 22. Barley RGB imagery 2019
observed from a,c,e) UAV and b,d,f) ground-level during a,b) June 26, c,d) July 3, e,f) July 31-August 2

4.4.2 Data processing

UAV surface energy balance

To disaggregate EC footprints, we used a high-resolution SEB model called HRMET (Zipper and Loheide 2014). In summary, HRMET solves the surface energy budget by inferring sensible heat from surface temperature (including measured net radiation and soil heat flux) and resolving ET as a residual. We applied this model to our barley field using high-resolution UAV inputs of surface temperature and LiDAR-derived canopy viewing fraction, effective leaf area index (LAI_e), and canopy height. We converted the modelled ET into a common scale index (ET_R) by normalizing between zero and one of the 2.5^{th} and 97.5^{th} percentiles. The ET_R patterns used here were validated in Section 3.7.5 against RGB, thermal, and leaf area index images. Briefly, the LiDAR-derived LAI_e was acquired using a Beers-Lambert relationship of discrete returns and observations, while the canopy height was determined as the 95^{th} percentile height from a LiDAR-derived digital elevation model. More detailed instructions on HRMET inputs and ET_R are given in Section 3.6.

Flux data processing and quality control

Eddy-covariance data was processed in Eddy Pro software (v6.2.1, 2018) using a Webb et al. (1980) correction for density fluctuations, Moncrieff et al. (1997, 2004) adjustments for high and low pass filtering, and default settings for addressing de-spiking, absolute limits, discontinuities, and angles of attack. We performed flux averaging over $30\ min$ intervals with a 10% missing sample allowance. Afterwards, we used Rstudio (R v4.0.2, 2020) to filter remaining records containing LE less than $-100\ W\ m^{-2}$ and friction velocity less than $0.1\ m\ s^{-1}$.

Flux footprint

Kljun et al.'s FFP (2015) predicts a two-dimensional flux footprint by tracing the touchdown probabilities back in time from the sensor location to the landscape sources. The FFP model has been validated against analytical models, large eddy simulations, wind tunnels, and tracer experiments. (Kljun et al. 2004b, 2015, Heidbach et al. 2017). The main benefits of FFP are its operability in most stability conditions (Kljun et al. 2004a) and its insensitivity to small roughness changes (Vesala et al. 2008, Leclerc et al. 2014). Shy of higher-order numerical models and hybrid LES approaches, which are computationally expensive, the FFP model offers a utile option. Some of the common footprint limitations apply to FFP, such as assumptions of flow stationarity,

horizontal homogeneity, and restrictions to the measurement height - measured above the roughness sub-layer and below the convective boundary layer (Kljun et al. 2015).

Kljun et al.'s (2015) FFP parameterization was adopted in this study to calculate two-dimensional flux footprints and climatologies. We supplied basic FFP inputs of sonic anemometer height, mean wind speed, Obukhov length, standard deviation of vertical velocity fluctuations, friction velocity, wind direction, and a boundary layer height determined using ERA5 reanalysis data (Hersbach et al. 2018). An LE flux term was also included for determining climatology footprints. Individual footprints span a single flux averaging period. They provide a two-dimensional upwind probability distribution useful for exploring the ET contributions of a particular record. To find a governing pattern, we refer to a climatology footprint of consecutive footprints.

We adapted the FFP code to include a LE weighting for each footprint. It involves multiplying each footprint contribution by its respective LE_{bulk} (eddy-covariance flux) and dividing the final footprint amalgamation by cumulative LE [28]. We use LE_{bulk} in place of ET_{bulk} here because it is the raw measurement from which ET is derived. The resulting climatology (F) tells the user 'where' flux is coming from and 'how much' with respect to the total cumulative flux. It assigns a greater weighting to records with higher LE flux (i.e. daytime fluxes) and thus distributes EC flux proportionate to the contributing landscape sources.

[28] $$F = \frac{\sum_{i=1}^{n}(F_i * LE_{bulk_i})}{\sum_{i=1}^{n}(LE_{bulk,i})}$$

Computation region

All raster manipulations were performed over a three-metre resolution grid. This specification was to match the ET_R resolution set according to the three-metre LiDAR-derived canopy structure inputs used to calculate ET. Accordingly, footprint flux values were also calculated at three-metre resolution and georegistered with ET_R prior to calculations. A region of $345\ m$ E-W by $390\ m$ N to S was used for analysis. Missing values were assigned a NA (void place-holder) to keep the domain structure but were otherwise omitted in calculations.

Spatial statistics

To compare differences between two coincident raster images, we used a modified t-test in R (Vallejos et al. 2020) following (Clifford et al. 1989, Dutilleul 1993). This test accounts for spatial autocorrelation by reducing the number of observations to an effective value supplying a Pearson correlation coefficient (r) and significance (p). Although this approach provides conservative p

values when cyclic patterns are present - crop row patterns not considered in the default autocorrelation template - (Dale and Fortin 2002), it nonetheless works well for agricultural applications - because the conservative p values are sufficient - (Taylor and Bates 2013).

4.4.3 Footprint disaggregation

A footprint disaggregation interprets what the flux tower 'sees' according to static ET_R images representative of an otherwise transient flux landscape. We infer that ET source patterns are linked to variations in water availability (SPI) and plant growth (phenology, foliage density and height); hence, we suggest that the ET pattern is a characteristic of a flux landscape and can be categorized into unique ET periods. It follows that an environment is defined by a finite number of unique ET periods and that ET_R could be used to interpret footprints of a different time with similar conditions. In the proposed disaggregated FFP (disFFP) method, we apply an ET_R-derived weighting to Kljun et al.'s (2015) FFP footprint function to acquire a source-weighted footprint.

ET_R selection

To ensure ET_R represents the largest intra-day ET contribution (mid-day), we use a time-of-day window between 11:00-15:00 CST for filtering the ET_R candidates. This avoids times of uneven solar heating (from low zenith angles) and selects ET_R where peak ET contributions and dominant patterns exist. The July 31, 2019, images - 19_212_h_1 (11:00 CST) and 19_212_h_3 (14:45 CST) - verify this assumption ($r = .91, p < 0.01$) using a modified t-test in R (Vallejos et al. 2020) for spatial autocorrelation (Clifford et al. 1989, Dutilleul 1993). Given a choice, we use an average of the two ET_R ($r = .98, p < 0.01$) to represent this image for disaggregation. Likewise, we assume that the coefficient of variation - standardized metric relating spatial ET standard deviation to mean ET - coincides with peak ET flux, and that the spatial relationship stored therein is representative of the flux majority. Disaggregating individual footprints involves only one ET_R image and a corresponding EC flux. For climatology graphs composed of multiple ET_R the process requires more discernment to pick an image representative of its time.

The time frame in question, henceforth called the ET period, is identified as an interval of near-constant rate day-over-day ET flux. Each ET period appears as a distinct linear segment on the cumulative ET plot. These linear trendlines are superimposed over diurnal signals and brief breaks in the data record, creating sections of consistent slope (ET rate). We first visually identify the nodes separating each period and then adjust our initial guesses using spliced linear regression fitting. We presume that if two ET_R occurred within the same period, they would be

similar, and an average ET_R would suffice. To qualify ET periods, we calculate and compare diurnal ET rates by averaging the total elapsed time (day and night) of each period. Coefficients of variation - ratios of spatial standard variation to mean ET observed in the SEB maps - are also given to each period as a potential moisture regime character trait. Additionally, we consider growing degree days (GDD) [29] (where T_{max} and T_{min} are the maximum and minimum observed daily temperatures, respectively), phenology, field photos, and relative moisture conditions to verify the period selection.

[29] $$GDD = \frac{T_{max} - T_{min}}{2} - 0\ ^{\circ}C$$

Although ET_R lacks scale and magnitude, we can combine it with observations of mean ET and spatial standard deviation (remote sensing SEB output) to interpret scalar values. A coefficient of variation (cv_{ET}) stores the spatial information (σ_{ET}, ET spatial standard deviation; μ_{ET}, ET spatial mean) captured using a remote sensing SEB model [30]. We can then use cv_{ET} to estimate a new spatial standard deviation ($\sigma_{\widehat{ET}}$) corresponding to an EC measured bulk ET (ET_{bulk}) following $\sigma_{\widehat{ET}} = cv_{ET}\ ET_{bulk}$. This step allows us to relate ET_R to actual ET values; moreover, it incorporates a high-quality ET observation (EC flux) into a spatial framework without relying on the SEB modelling accuracy. Relative ET is converted first to its standard normalized form using equation [31] and the ET_R standard deviation (σ_{ET_R}) and mean (μ_{ET_R}). Afterwards, a new ET map ($\widehat{ET}$) is made following [32]. In the case of an ET period, we substitute ET_{bulk} for a cumulative day-over-day ET rate (ET_{rate}) representative of that period. Finally, multiple ET periods are combined into an effective ET (ET_e) using a duration (i) weighting ($d_i / \sum_{i=1}^{i=N} d_i$) of the total ET periods (N) [33]. This ET_e product, likely with units in $mm\ d^{-1}$, is easily converted to a cumulative ET map by multiplying ET_e by the number of elapsed days.

[30] $$cv_{ET} = \frac{\sigma_{ET}}{\mu_{ET}}$$

[31] $$ET_{SN} = \frac{ET_R - \mu_{ET_R}}{\sigma_{ET_R}}$$

[32] $$\widehat{ET} = ET_{SN}\ \widehat{\sigma_{ET}} + ET_{bulk}$$

[33] $$ET_e = \sum_{i=1}^{i=N} \widehat{ET_i}\ \frac{d_i}{\sum_{i=1}^{i=N} d_i}$$

disFFP

The disFFP method proposed in this study disaggregates individual footprints using the derived ET map ($\widehat{ET}$). First, the unscaled disaggregation matrix χ was derived following element-wise

multiplication of [34], where r and c are the number of rows and columns in the computation space. A scaling factor (ω) was then found from the areal sum $\omega = \sum_{i=1}^{r}\sum_{j=1}^{c}\chi_{i,j} \;/\; \sum_{i=1}^{r}\sum_{j=1}^{c}F_{i,j}$. We then applied ω as a constant scalar to all cells in χ to yield the disaggregated footprint (F_D) following $F_D = \chi/\omega$. For visualization purposes, F_D could then be limited to a 90% contribution range and converted to percentage isopleths following a minimum-value threshold discretization - our interpretation of Kljun et al.'s (2015) relative contribution prescription. This iterative operation keeps a running tally of the unassigned total flux percentage (initially F_D multiplied by cell size) and assigns the current-iteration flux percentages to the cells falling below a current-iteration threshold (starting very small and increasing by 0.1% at each iteration) and continues until all footprint cells have assigned percentages.

[34] $$\chi = \frac{\widehat{ET}}{\sum_{i=1}^{r}\sum_{j=1}^{c}\widehat{ET}_{i,j}}\,F$$

4.5 Results and discussion

We start this section by designating ET periods for each growing season and discussing similarities among years. We then test disFFP for a single flux footprint, an ET period, and seasonal climatologies. Lastly, the discussion then extends to disaggregating a multi-season climatology within a single ET period.

4.5.1 ET periods

Cumulative seasonal ET graphs provide a basis for segmenting ET periods (Figure 23). We split each season into five ET periods: namely 'Pre', 'Early', 'Mid', 'Late', and 'Post', to which ET_R are matched. Piece-wise linear regression affirmed the node selections with $RMSE$ of 2.2, 1.5, and $2.0\ mm$ and $R^2 > 0.99$ for 2018, 2019, and 2020 respectively (Appendix B1). The relatively close 2019 June 26 and July 3 images fall along visually discernable slopes, 3.2 and $3.8\ mm\ d^{-1}$, respectively and are thus separated. The brief 'Early' segments (2018 and 2019) are consistent with a rapid green-up period after early season rainfall (Figure 23). The longer 'Early' segment for 2020 is consistent with improved crop growth (greater LAI and canopy height than in 2018 -2019).

The 'Early', 'Mid', and 'Late' periods generally coincided with tillering through head filling (Appendix B2). Not unexpectedly, the 'Pre' and 'Post' seasons reflect the fringe growth phases of emergence and canopy senescence. Year-to-year nuances on the exact phenology dates reflect a mix of segmentation biases and yearly unique hydrological circumstances. While the 2019 and 2020 'Late' periods occupied heading to fruit development stages, the 2018 'Late' ET period

occurred from heading to harvest. We suspect this deviation is related to 2018's dry field conditions (Figure 20) and stunted crop growth (Table 8).

Across the three seasons, the ET period to growing degree day (GDD) associations differed 5-36% (standard deviation as a percentage of sample mean), with the ending GDD of the 'Pre' periods having the least precision and the 'Mid' and 'Late' GDDs having the highest precisions (Appendix B2). Similarly, ET rates varied $2-38\%$, with the closest agreement between 'Late' periods and the least agreement for the 'Pre' and 'Post' periods. It is peculiar that ET rates are relatively consistent across years for like periods despite 2020 having nearly twice the foliage height and density than those from 2018. Although ET rates differentiate ET periods within a season, they alone may not be sufficient to group ET periods across growing seasons. Additionally, consistent coefficients of variation across 'Late' periods (Table 8) suggest that this metric may offer a corollary to ET rate for interpreting ET periods. Other factors such as SPI, LAI, canopy height, and phenology timing may influence ET period associations between years.

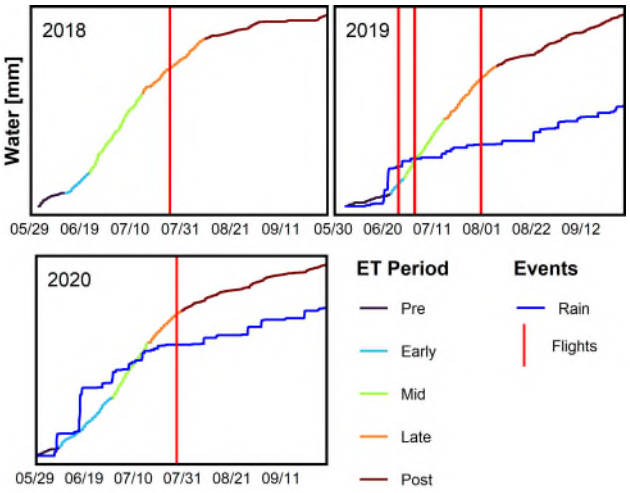

Figure 23. Cumulative ET denoting constant-rate ET periods
Flight overpass days (vertical red lines) and cumulative precipitation (blue line) were added for reference for the 2019 and 2020 seasons

Table 8. Phenology corresponding to UAV field days

ET_R date [YY_DDD]	ET_R Barley phenology	ET period	ET period rate $[mm\ d^{-1}]$	Coefficient of Variation	LAI_e* $[m^2\ m^{-2}]$	h* $[m]$
18_207	Anthesis	Late	2.7	0.10	2.5	0.65
19_177	Tillering	Early	3.2	0.07	0.2	0.18
19_184	Stem Elongation	Mid	3.8	0.23	0.4	0.23
19_212	Head Filling	Late	2.6	0.10	3.4	0.70
20_210	Heading	Late	2.6	0.10	5.2	0.84

* Computation region (field) averaged values

4.5.2 Disaggregation

Single footprint

Following the conversion from ET_R to $\widehat{ET}$ (Equations [30],[31],[32]), we demonstrate how the spatial ET patterns from a high-resolution SEB model Figure 24a) can be re-interpreted (Figure 24b) using the more-accurate ET_{bulk}. This novel ET combination method pairs the accuracy of the EC method with the precise spatial distributions of a high-resolution ET model and thus incorporates the strengths from both approaches. In future work, we suggest testing the allotment accuracy of this method using in-situ ET survey techniques.

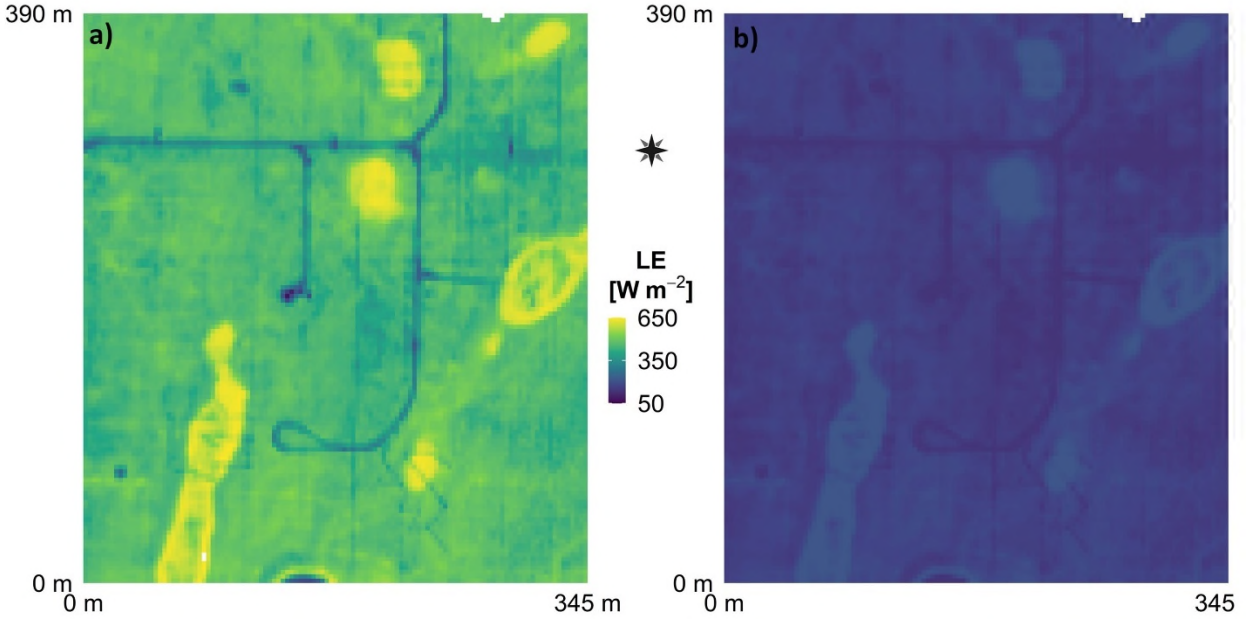

Figure 24. Barley ET combination method expressed as latent heat flux
a) LE measured from SEB model and b) re-interpreted using eddy-covariance bulk LE for 20_210_h_2

As an initial test for the disFFP method, we apply it to an individual footprint (Figure 25). This represents our closest means of comparison because the EC footprint and ET_R image directly coincide. The 20_210_h_1 footprint (Figure 25a) extends across a transpiring depression with high ET indicated in yellow (Figure 25b). The disFFP method (Figure 25c) responds accordingly by assigning these hotspots a higher-ranking flux value (minus $2-4\%$). Similarly, the influence of low-ET foot pathways and access roads (Figure 25d) is reduced - i.e. positive flux percent change - (Figure 25e). This example demonstrates the ability of disFFP to address source-heterogeneity from surfaces of heightened ET (moisture-rich depressions) and reduced ET (pavement, cover material, extensive bare ground) mingled in the landscape. Ultimately, disFFP

shows what we already intuitively know about the ET flux pattern based on variable crop growth and topography (indicative of soil moisture availability).

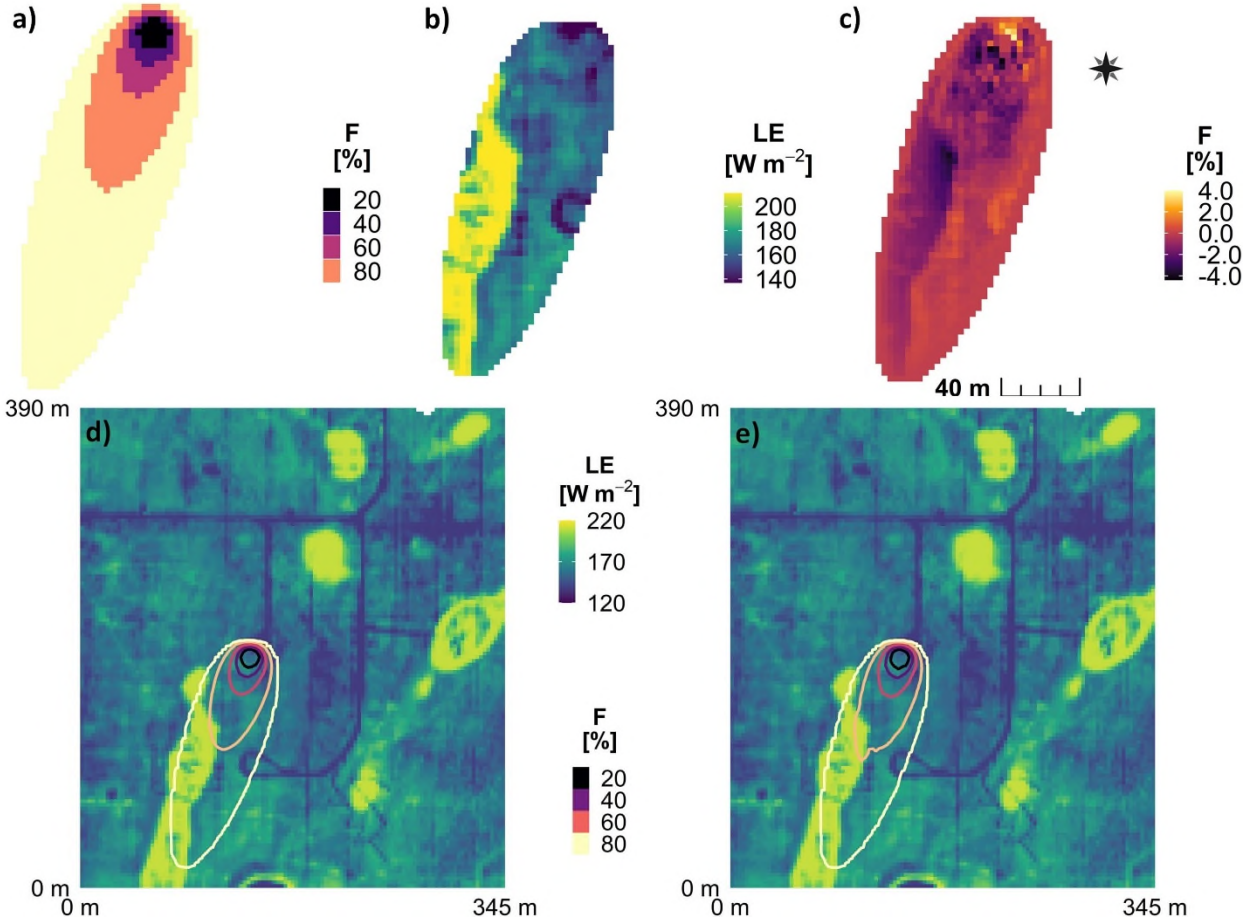

Figure 25. Barley disFFP progression with single LE footprint July 28, 2020
a) FFP, b) $\widehat{ET}$ (expressed as latent heat) from ET_R, c) disFFP changes to FFP, d) FFP and b) disFFP

The previous example qualifies disFFP based on known coinciding ET patterns. We continue the discussion to amalgamated climatologies where concurrent remote sensing ET patterns were not directly observed. We now rely on the proposed ET period linkages to inform disFFP application.

Seasonal

We test disFFP using the 2019 'Early', 'Mid', and 'Late' ET period climatologies (Figure 26). The original FFP footprint (Figure 26a) overlooks source heterogeneity depicted using ET_e - the combination of ET_R and cv_{ET} from each ET period (Figure 26b); whereas, the disFFP footprint (Figure 26c) makes these relative adjustments (-4 to $+6\%$ change).

The combination of ET source patterns and EC footprints provide a new line of feedback for improving EC experiments. We notice the ET_e depicts a yellow, crescent-shaped patch of high

ET surrounding the flux tower and the highest-weighted F contributions (Figure 26a). Coincidentally, F_D is also concentrated around the tower (Figure 26e). This insight provides feedback for us to improve our tower installations by addressing cropping management around the tower. Moreover, while Kljun et al.'s FFP parameterized code (2015) enabled a 90% contribution fetch for the single footprints, it truncated the climatology footprint limits below 90%, so an 80% flux extent was imposed. Breaking away from the $1V:100H$ rule of thumb (Burba 2013), this finding suggests that for short-tower ($2-3\ magl$) climatology footprints over short vegetation (less than one-metre) at 80% contribution the ratio is half as much ($1V:50H$) than that of the anticipated field coverage.

A benefit of disFFP is that it adapts to alterations imposed on the study site. For example, whereas the adjacent research pad occupied a large F portion in the FFP approach, it was systematically devalued in F_D using the disFFP method. Access paths in the 2018 and 2020 images (not shown) are also accounted for in the F_D. The disFFP method presents a pragmatic approach for adapting EC footprints to surrounding flux landscapes while being flexible to site disturbance.

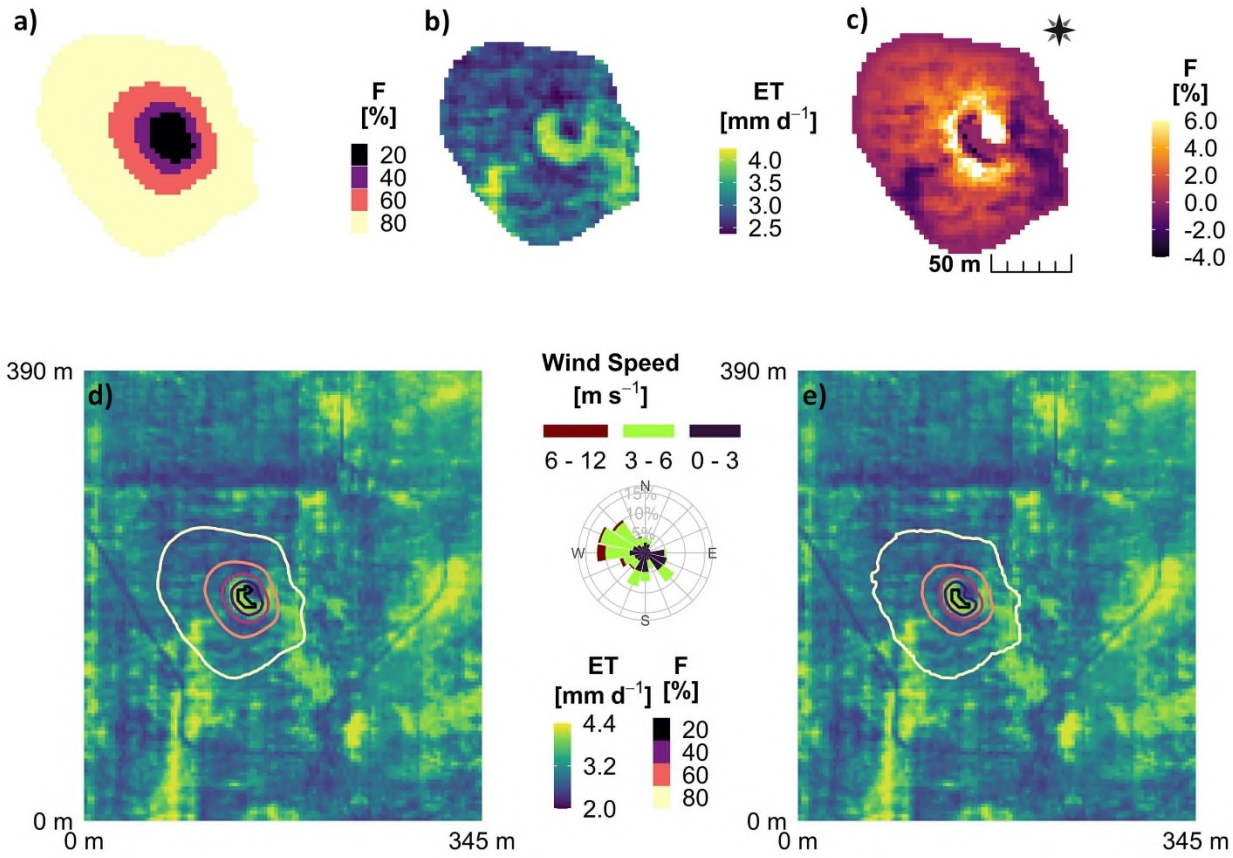

Figure 26. Barley seasonal disFFP application 2019

a) original FPP, b) ET_e underneath footprint, c) respective disFFP changes, d) FFP over ET_e map, e) disFFP over ET_e map. Climatology windrose is limited to daytime (6:00-18:00 CST) values. Footprint values (F) are given as a percentage of the total flux (limited to the computation region extent)

Ancillary to disFFP, our ET combination method (converting ET_R and cv_{ET} to ET_e and $\widehat{ET}$) presents the ability to allocate cumulative ET across the featured landscape (Figure 27). In this example, the $144\ mm$ of ET estimated using the EC method is re-interpreted within the source heterogeneity of the field. It is revealed that a negligible $90 - 100\ mm$ of ET occurred over the roadways and northern tillage ridge, while the ET from depressional areas exceeded our EC estimate by 38% $(180 - 200\ mm)$.

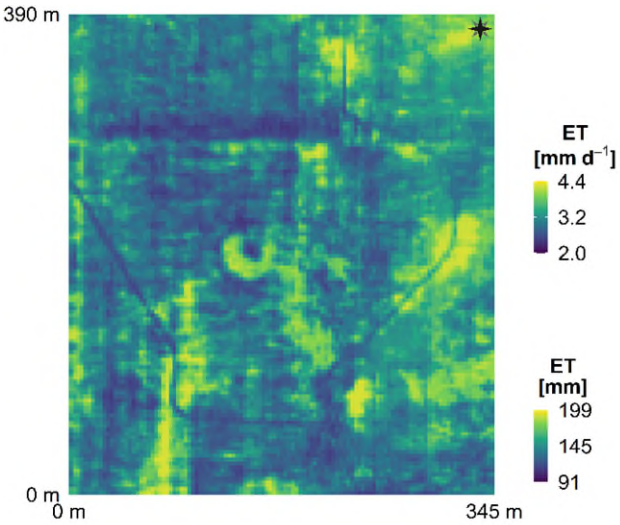

Figure 27. Effective ET rate (ET_e) and cumulative ET for early to late ET periods in 2019

Multi-season

In addition to seasonal applications, we test disFFP using multi-year data from similar ET periods. This enables focused investigation on a specific growth stage. We apply a contribution disaggregation to the 2018-2020 'Late' ET periods (Figure 28). Dominant wind patterns from the NWW and SEE directions form the overall footprint shape. Underlying landscape forces further articulate the flux ranking by attributing greater ET to the higher ET_e and removing it from low ET_e areas. The resultant footprint maintains a similar extent to the original FFP, yet it repositions the footprint values in accordance with ET_R. Interestingly, the multi-season approach softens the signals from our site disturbances (access paths) yet retains the key landscape ET patterns. Despite interannual differences, we identify a persistence of the low-ET ridge running E-W, four unique high-ET depressions, and a low-ET gravel pad in the SW corner. It follows that multiple images are best suited for inferring intrinsic landscape features from ET patterns.

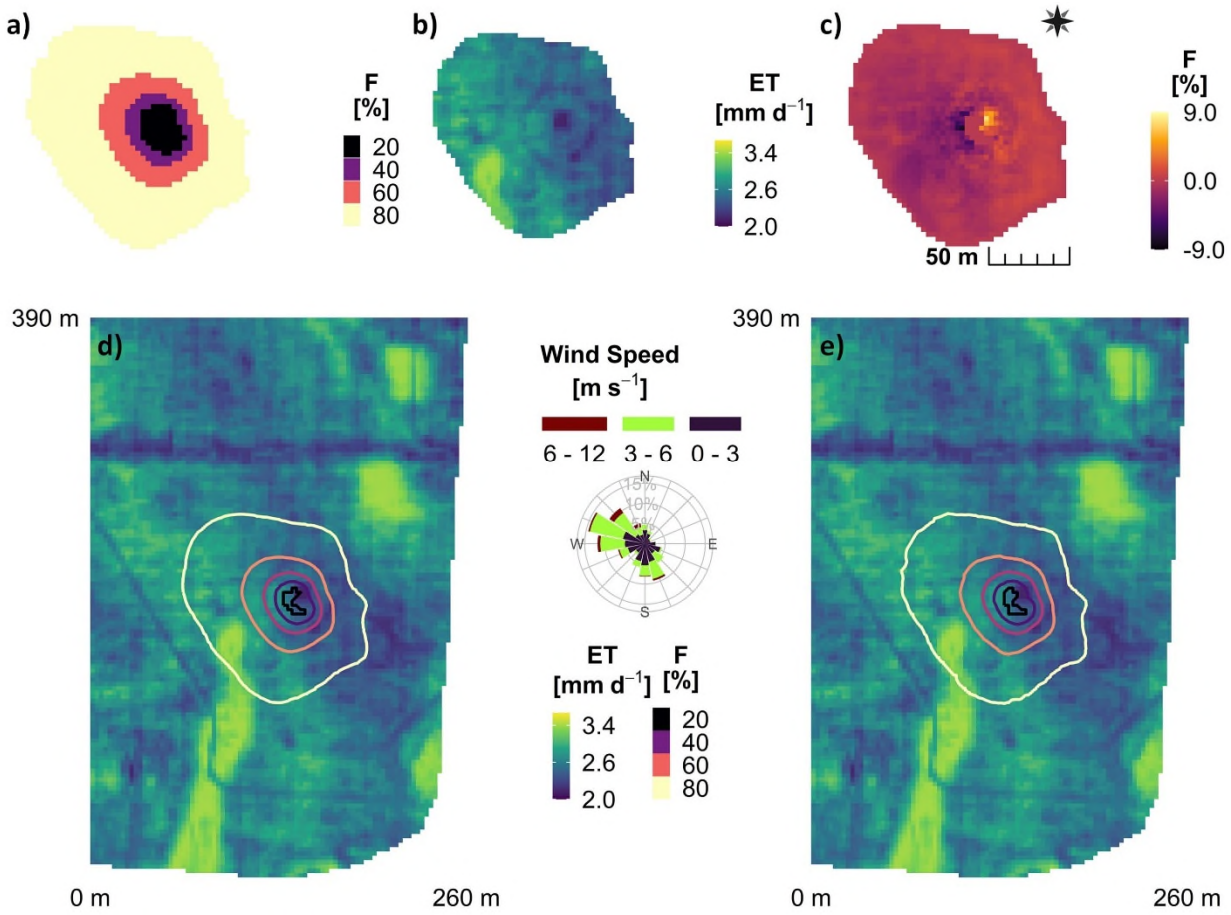

Figure 28. Disaggregated interseasonal climatology footprints 2018-2020
Climatologies (by contribution) from barley anthesis to senescence ('Late' ET periods). Footprint values (F) are given as a percentage of the total flux (limited to 80%)

4.5.3 Limitations and recommendations

Limitations exist when using discrete ET_R observations (and derived ET_e) to interpret continuous EC footprints. Since flight conditions cannot be controlled during ET_R acquisitions, this challenges their representativeness of ET periods. Further differences in flight payloads or instrument types may also introduce uncertainty into the ET_R comparison, especially when collection takes place over multiple seasons and equipment is replaced. We also note that spatial relationships from cv_{ET} have some diurnal and seasonal influences, so our peak-day assumption provides only a first-order estimate (Appendix B3). Future work could incorporate a variable cv_{ET} model responding to some continuously monitored environmental variable. Finally, with interpreting ET periods between seasons, it is assumed that the crop type and agricultural management (seeding, fertilizing, irrigation) remain the same.

In this study, we developed a new disaggregation technique (disFFP) for interpreting source heterogeneity in EC footprints using high-resolution ET patterns from UAV remote sensing. We demonstrated how disFFP can spatially allocate bulk eddy-covariance LE within a footprint and across the greater extent of the field. Moreover, we gave a practical example of spatially allocating cumulative ET for seasonal water balances. Coupled with ET periods and characteristic ET_R maps, we showed how disFFP captures persistent source heterogeneity patterns in a flux landscape and thus can alleviate disparate UAV and EC measurement time scales. Consequently, disFFP might be run using a catalogue of pre-determined ET_R maps. Upon retrieving this ET_R database, the EC study could continue without further UAV acquisitions. We recommend exploring disFFP over a longer range of EC data, further considering spatial soil moisture availability in addition to the factors discussed (phenology timing, foliage density and height, SPI). Another extension of this work might be to test disFFP on larger regions containing multiple land classifications. For these complex landscapes, it seems necessary to derive unique ET_R relationships for each land classification and use a mosaic of ET_R to then apply disFFP.

4.6 Conclusion

This study demonstrates the utility of using discrete ET_R maps from UAVs to disaggregate continuous EC tower flux footprints. We introduced a disaggregated flux footprint prediction method (disFFP) using Kljun et al.'s (2015) parameterized footprint model as a base. We then developed the concept of ET period using steady rate eddy-covariance ET fluxes with piece-wise linear regression to differentiate periods. We used ET_R from HRMET (Zipper and Loheide II 2014) and coefficients of variation to represent the ET patterns from coinciding ET periods. Then we discussed these ET periods in terms of phenology, foliage density and height, and SPI, demonstrating that ET rate alone was not enough to categorize ET periods among hydrological landscapes of different years. After verifying disFFP on a single footprint, we extended it to climatology footprints through the concepts of ET period and ET_R linkages. This method resolved spatial flux influences around known high ET corridors (well-watered depression) and low ET zones (especially those created through human alteration, i.e. access pathways, monitoring pads, equipment, etc.). An EC bulk ET of $122\ mm$ was depicted as a map of spatially variable sources: $0-20\ mm$ around pathways and gravel pads and $180-200\ mm$ derived over moisture-rich depressions. Ultimately, disFFP improved upon FPP by depicting what is intuitively known about the ET flux pattern based on variable crop growth and topography (tied to soil moisture availability). Furthermore, we demonstrated how similar ET_R images from one year could interpret the disFFP

spatial flux patterns of another year similar to or better than the coinciding FFP proximity-based description. These findings warrant further investigation into the disFFP method and its utility in EC monitoring programs.

5 SYNTHESIS AND CONCLUSION

We set out to find a way to disaggregate eddy-covariance (EC) fluxes using sub-metre evapotranspiration (ET) from a surface energy balance model - HRMET. First, we began the study by assessing HRMET; performance against EC short tower flux estimates, as this comparison had not been published yet in other works. This step comprised most of Section 3, the first manuscript. Integrating with HRMET, we assessed a UAV Light Detection And Ranging (LiDAR) method for retrieving high-resolution canopy structures of crop height (h), canopy viewing fraction (f_c), and Leaf Area Index (LAI). Upon validating HRMET and its ET pattern, in the form of a relative ET index (ET_R), we continued with the initial objective of disaggregating EC footprints throughout Section 4. In that section, we proposed the concept of 'ET period' to help form linkages between discrete ET_R maps and continuous climatology footprints based on characteristic landscape hydrology and phenology traits. We first tested our disaggregated Flux Footprint Prediction (disFFP) on a single footprint with coincident ET_R. Based on ET period, we extended disFFP application to a seasonal climatology and then to a multi-season single-period trial.

Key results from this thesis include:

- UAV LiDAR can provide high-resolution h, f_C, and LAI estimates coinciding with observed field patterns (RGB and DEM maps) and field-average values.
- UAV LiDAR interpretations of h are underestimated in sparse canopies but can be scaled to match ground-level observations.
- UAV LiDAR derived LAI_e achieved good $RMSE$ ($0.08 - 0.81\ m^2 m^{-2}$) with ground LP-80 LAI observations, but that a large range of R^2 ($< 0 - 0.81$) indicates a need for higher-precision sampling protocols for LAI observations in short-field crops;
- Practical application of the 'vicarious radiance' approach requires $R^2 > 0.67$ and $RMSE < 0.4\ W\ m^{-2} sr^{-1} \mu m^{-1}$ to be effective;
- Thermal atmospheric and $\epsilon_{ensemble}$ corrections have larger effects in early-season images when greater atmospheric moisture is present;
- Thermal corrections had little effect on relative temperature patterns, as shown from a modified t-test ($r > .99, p \ll 0.001$);

- HRMET applied with UAV LiDAR and T_B or $T_{B,obs}$ surface temperatures gave a $79 - 136$ $W\ m^{-2}$ $RMSE$ (equivalent to $0.12 - 0.22\ mm\ hr^{-1}$ at $20°C$) against EC latent heat flux and tended to overestimate LE over full canopies when surface-air temperature gradients exceeded $4 - 5\ °C$;
- ET_R preserves ET patterns similarly using $T_{B,obs}$ (uncorrected sensor brightness temperature) as it does with T_B, $T_{R,obs}$, and T_R as shown from a modified t-test ($r > .93$, $p \ll 0.001$);
- ET_R and ET period have synergy within the proposed disFFP method enabling EC footprint disaggregation;
- disFFP allocates bulk EC estimates of LE and ET to the surrounding landscape using ET_R and combines the accuracy of the EC method with the spatial precision of a UAV surface energy balance model. (Allocated $144\ mm$ of cumulative ET over roadways with 100 mm and wet depressions with $200\ mm$)
- disFFP may add greater versatility to EC research by allowing continuous footprint disaggregation from discrete UAV acquisitions.

In Section 3, we tested the application of UAV LiDAR to acquire high-resolution inputs of h, f_c, and LAI for use in a surface energy balance model - HRMET. Moreover, we assessed the utility of atmospheric and $\epsilon_{ensemble}$ temperature corrections and their impacts on HRMET output magnitude and pattern. Lastly, we compared HRMET against short tower EC fluxes and characterized the changing moisture environment using ET patterns as depicted with the ET_R index.

Our choice of an HRMET delivery method was decided based on the available UAV payloads held within our research team. Alongside existing FLIR Pro Vue R and ThermoMap infrared imagers, we used a Riegl miniVUX1-UAV LiDAR to retrieve survey-grade point clouds for canopy structure derivation. Our assessment of LiDAR-derived h, f_c, and LAI was confounded somewhat by poor spatial registration with ground observations; however, the resultant products agreed with independent RGB imagery, site knowledge, and field-average observations.

To address difficulties in obtaining thermodynamic surface temperatures from UAV thermal, we assessed incremental thermal treatments for preserving HRMET output ET patterns. After post-processing instrument calibrations, we considered the effects of using raw brightness temperature ($T_{B,obs}$), target brightness temperature (T_B), observed radiometric temperature ($T_{R,obs}$), and target radiometric temperature (T_R). We applied an $\epsilon_{ensemble}$ correction to find $T_{R,obs}$ and a radiance

linear regression with ground-level observations to determine $T_{R,obs}$; afterwards, these were combined to form the quintessential T_R. Surprisingly, we found that all thermal treatments were spatially related and produced indistinguishable ET_R estimates ($r > .99, p < 0.01$).

We started with the understanding that HRMET is a hybrid model involving a two-source radiation scheme with a one-source bulk handling of sensible heat. After assessing the component fluxes of HRMET's surface energy balance, we realized that it performs more like a one-source model. Mainly, it underestimated sensible heat flux over full canopies when surface-air temperatures exceeded $4 - 5\ °C$.

When comparing HRMET, we used a time weighting scheme to register meteorological and EC records. This process determined the exact environmental inputs to use in HRMET at the time of footprint overpass; it also shifted the EC estimate towards either adjacent $30\ min$ record, depending on the overpass period. From this comparison, HRMET replicated EC fluxes within $79 - 136\ W\ m^{-2}\ RMSE$ (equivalent to $0.12 - 0.20\ mm\ hr^{-1}$ at $20°C$). The modest performance of HRMET at matching EC fluxes was compensated by its ability to capture precision ET patterns.

Continuing with our first objective, our work in Section 4 took the described ET patterns (represented by ET_R) and applies them to disaggregate EC flux footprints. After defining our borrowed footprint model, we proceeded to introduce our concept of 'ET period' and the proposed disaggregated flux footprint prediction (disFFP) method. We made a base assessment of disFFP using a single ET_R and the coinciding EC footprint. Finally, we tested disFFP in more useful examples of a seasonal climatology disaggregation

To bridge the connection between discrete ET_R and continuous EC fluxes, we presented the concept of 'ET period'. Namely, we defined an ET period as an interval of constant rate day-over-day EC flux. These ET periods also maintained similar representative coefficients of variation (from ET remote sensing SEB model). In pictures and with a phenology timeline, we showed how our seasonal ET periods generally coincided with vegetative growth phases. Additionally, we considered concurrent site hydrology to explain apparent inter-seasonal timing differences between like periods.

We then introduced our disFFP as a direct method for single footprints and as a guided approach using ET period linkages for climatology footprints. Our single footprint disaggregation showed that disFFP reallocated EC flux in favour of ET sources and away from non-transpiring features. Intriguingly, disFFP worked around site interferences (access roads, pathways, equipment) and diminished the contributions of these areas over the original footprint model. A similar confirmation

was made when we extended disFFP to seasonal climatology applications. Moreover, we gave an example that considered $144\ mm$ of cumulative ET (measured during part of the 2019 season at Barley) and used disFFP to attach absolute ET values to the seasonal ET_R map (100 mm over roadways and $200\ mm$ over wet depressions). Finally, we tested inter-seasonal disFFP by combining ET_R of like ET periods from three years. We found that the averaged ET_R softened the impact of year-to-year site modifications and exposed the prevailing landscape source heterogeneities of the time. These findings implicate using ET patterns and ET periods for future work describing flux landscapes under constant monitoring.

In conclusion, our work demonstrates a new way to interpret EC data using ET maps acquired from discrete UAV energy balances. We presented a novel UAV-LiDAR workflow for retrieving detailed canopy structures. We then benchmarked the HRMET model against EC fluxes and showed that a raw brightness temperature is sufficient to replicate ET_R patterns. Afterwards, we applied ET_R to disaggregate EC footprints by supplying an ET period description. This disFFP approach allocated fluxes consistent with interlaying footprint features. We present this work as a novel workflow for high-resolution UAV energy balance retrieval and EC footprint disaggregation.

REFERENCES

Aboutalebi, M., Torres-Rua, A.F., McKee, M., Kustas, W.P., Nieto, H., Alsina, M.M., White, A., Prueger, J.H., McKee, L., Alfieri, J., Hipps, L., Coopmans, C., and Dokoozlian, N. 2020. Incorporation of Unmanned Aerial Vehicle (UAV) point cloud products into remote sensing evapotranspiration models. Remote Sensing, **12**(1). doi:10.3390/RS12010050.

Alfieri, J.G., Kustas, W.P., Prueger, J.H., Hipps, L.E., Evett, S.R., Basara, J.B., Neale, C.M.U., French, A.N., Colaizzi, P., Agam, N., Cosh, M.H., Chavez, J.L., and Howell, T.A. 2012. On the discrepancy between eddy covariance and lysimetry-based surface flux measurements under strongly advective conditions. Advances in Water Resources, **50**: 62-78. Elsevier Ltd. doi:10.1016/j.advwatres.2012.07.008.

Allen, R.G., Pereira, L.S., Raes, D., Smith, M., and Ab, W. 1998. Fao,1998. Irrigation and Drainage Paper No. 56, FAO,: 300. doi:10.1016/j.eja.2010.12.001.

Allen, R.G., Tasumi, M., Morse, A., Trezza, R., Wright, J.L., Bastiaanssen, W., Kramber, W., Lorite, I., and Robison, C.W. 2007. Satellite-Based Energy Balance for Mapping Evapotranspiration with Internalized Calibration (METRIC)—Applications. Journal of Irrigation and Drainage Engineering, **133**(4): 395-406. doi:10.1061/(asce)0733-9437(2007)133:4(395).

Anderson, C.A., and Vivoni, E.R. 2016. Impact of land surface states within the flux footprint on daytime land-atmosphere coupling in two semiarid ecosystems of the Southwestern U.S. Journal of the American Water Resources Association, **52**: 4785-4800. doi:10.1111/j.1752-1688.1969.tb04897.x.

Anderson, M.C., Norman, J.M., Kustas, W.P., Li, F., Prueger, J.H., and Mecikalski, J.R. 2005. Effects of vegetation clumping on two-source model estimates of surface energy fluxes from an agricultural landscape during SMACEX. Journal of Hydrometeorology, **6**(6): 892-909. doi:10.1175/JHM465.1.

Baldocchi, D., Falge, E., Gu, L., Olson, R., Hollinger, D., Running, S., Anthoni, P., Bernhofer, C., Davis, K., Evans, R., Fuentes, J., Goldstein, A., Katul, G., Law, B., Lee, X., Malhi, Y., Meyers, T., Munger, W., Oechel, W., Paw, U.K.T., Pilegaard, K., Schmid, H.P., Valentini, R., Verma, S., Vesala, T., Wilson, K., and Wofsy, S. 2001. FLUXNET: A New Tool to Study the Temporal and Spatial Variability of Ecosystem-Scale Carbon Dioxide, Water Vapor, and Energy Flux Densities. Bulletin of the American Meteorological Society, **82**(11): 2415-2434. doi:10.1175/1520-0477(2001)082<2415:FANTTS>2.3.CO;2.

Barcza, Z., Kern, A., Haszpra, L., and Kljun, N. 2009. Spatial representativeness of tall tower eddy covariance measurements using remote sensing and footprint analysis. Agricultural and Forest Meteorology, **149**(5): 795-807. doi:10.1016/j.agrformet.2008.10.021.

Bastiaanssen, W.G.M., Meneti, M., Feddes, R.A., and Holtslag, A.A.M. 1998a. A remote sensing surface energy balance algorithm for land (SEBAL) Part 1: Formulation. J. Hydrol., **212-213**(JANUARY): 198-212. doi:http://dx.doi.org/10.1016/S0022-1694(98)00254-6.

Bastiaanssen, W.G.M., Pelgrum, H., Wang, J., Ma, Y., and Moreno, J.F. 1998b. A remote sensing surface energy balance algorithm for land (SEBAL).: Part 2: Validation. Journal of Hydrology, **212**: 213-229.

Brenner, C., Thiem, C.E., Wizemann, H.D., Bernhardt, M., and Schulz, K. 2017. Estimating spatially distributed turbulent heat fluxes from high-resolution thermal imagery acquired with a UAV system. International Journal of Remote Sensing, **38**(8-10): 3003-3026. Taylor & Francis. doi:10.1080/01431161.2017.1280202.

Brutsaert, W., Hsu, A.Y., and Schmugge, T.J. 1993. Parameterization of surface heat fluxes above forest with satellite thermal sensing and boundary layer soundings. Journal of Applied Meteorology, **32**(5): 909-917.

Burba, G. 2013. Eddy Covariance Method-for Scientific, Industrial, Agricultural, and Regulatory Applications. *In* Book. LI-COR Biosciences, 4647 Superior Street, Lincoln, Nebraska, USA.

Clifford, P., Richardson, S., and Hemon, D. 1989. Assessing the Significance of the Correlation between Two Spatial Processes Author (s): Peter Clifford , Sylvia Richardson and Denis Hemon Published by : International Biometric Society Stable URL : https://www.jstor.org/stable/2532039 REFERENCES Linked. Biometrics, **45**(1): 123-134.

Colaizzi, P.D., Evett, S.R., Howell, T.A., Li, F., Kustas, W.P., and Anderson, M.C. 2012a. Radiation model for row crops: I. Geometric view factors and parameter optimization. Agronomy Journal, **104**(2): 225-240. doi:10.2134/agronj2011.0082.

Colaizzi, P.D., Schwartz, R.C., Evett, S.R., Howell, T.A., Gowda, P.H., and Tolk, J.A. 2012b. Radiation model for row crops: II. model evaluation. Agronomy Journal, **104**(2): 241-255. doi:10.2134/agronj2011.0083.

Dale, M.R.T., and Fortin, M. 2002. Spatial autocorrelation and statistical tests in ecology. Ecoscience, **9**(2): 162-167.

Deems, J., and Painter, T.H. 2006. Lidar measurement of snow depth: accuracy and error sources.

In Proceedings of the International Snow Science Workshop.

Dutilleul, P. 1993. Modifying the t Test for Assessing the Correlation Between Two Spatial Processes. Biometrics, **49**(1): 305. doi:10.2307/2532625.

Ellis, J.G., Acton, D.F., Moss, H.C., Acton, C.J., Ballantyne, A.K., Shields, J.A., Stonehouse, H.B., Janzen, W.K., and Radford, F.G. 1970. The Soils of the Rosetown Map Area. : 172.

Engel, J.L., and Weinstein, O. 1983. The Thematic Mapper-An Overview. IEEE Transactions on Geoscience and Remote Sensing, **GE-21**(3): 258-265.

Eugster, W., and Merbold, L. 2015. Eddy covariance for quantifying trace gas fluxes from soils. Soil, **1**(1): 187-205. doi:10.5194/soil-1-187-2015.

Foken, T. 2008. The energy balance closure problem: An overview. Ecological Applications, **18**(6): 1351-1367. doi:10.1890/06-0922.1.

Foken, T. 2016. Micrometeorology. *In* 2nd edition. Springer Berlin Heidelberg, Berlin.

Gelybó, G., Barcza, Z., Kern, A., and Kljun, N. 2013. Effect of spatial heterogeneity on the validation of remote sensing based GPP estimations. Agricultural and Forest Meteorology, **174-175**: 43-53. Elsevier B.V. doi:10.1016/j.agrformet.2013.02.003.

Göckede, M., Markkanen, T., Hasager, C.B., and Foken, T. 2006. Update of a footprint-based approach for the characterisation of complex measurement sites. Boundary-Layer Meteorology, **118**(3): 635-655. doi:10.1007/s10546-005-6435-3.

Government of Canada. 2021. Almanac Averages and Extremes. Available from https://climate.weather.gc.ca/climate_data/almanac_selection_e.html. [accessed 28 January 2022].

Griebel, A., Bennett, L.T., Metzen, D., Cleverly, J., Burba, G., and Arndt, S.K. 2016. Effects of inhomogeneities within the flux footprint on the interpretation of seasonal, annual, and interannual ecosystem carbon exchange. Agricultural and Forest Meteorology, **221**: 50-60. Elsevier B.V. doi:10.1016/j.agrformet.2016.02.002.

ten Harkel, J., Bartholomeus, H., and Kooistra, L. 2020. Biomass and crop height estimation of different crops using UAV-based LiDAR. Remote Sensing, **12**(17). doi:10.3390/RS12010017.

Heidbach, K., Schmid, H.P., and Mauder, M. 2017. Experimental evaluation of flux footprint models. Agricultural and Forest Meteorology, **246**(October 2016): 142-153. Elsevier. doi:10.1016/j.agrformet.2017.06.008.

Hersbach, H., Bell, B., Berrisford, P., Biavati, G., Horányi, A., Muñoz Sabater, J., Nicolas, J., Peubey, C., Radu, R., Rozum, I., Schepers, D., Simmons, A., Soci, D., Dee, D., and Thépaut, J.-N. 2018. ERA5 hourly data on single levels from 1979 to present.

Hoffmann, H., Nieto, H., Jensen, R., Guzinski, R., Zarco-Tejada, P., and Friborg, T. 2016. Estimating evaporation with thermal UAV data and two-source energy balance models. Hydrology and Earth System Sciences, **20**(2): 697-713. doi:10.5194/hess-20-697-2016.

Horst, T.W., and Weil, J.C. 1992. Footprint estimation for scalar flux measurements in the atmospheric surface layer. Boundary-Layer Meteorology, **59**(3): 279-296. doi:10.1007/BF00119817.

Hutjes, R.W.A., Vellinga, O.S., Gioli, B., and Miglietta, F. 2010. Dis-aggregation of airborne flux measurements using footprint analysis. Agricultural and Forest Meteorology, **150**(7-8): 966-983. Elsevier B.V. doi:10.1016/j.agrformet.2010.03.004.

Isenburg, M. 2021. LAStools - efficient LiDAR processing software.

Jensen, J.R. 2015. Introductory digital image processing - A remote sensing perspective. *In* 4th ed. Pearson Education Inc., Glenview, Illinois.

Joy, S.L., and Chávez, J.L. 2021. Correction of eddy covariance based crop ET considering the heat flux source area. Atmosphere, **12**(2). doi:10.3390/atmos12020281.

Kelly, J., Kljun, N., Eklundh, L., Klemedtsson, L., Liljebladh, B., Olsson, P.O., Weslien, P., and Xie, X. 2021. Modelling and upscaling ecosystem respiration using thermal cameras and UAVs: Application to a peatland during and after a hot drought. Agricultural and Forest Meteorology, **300**(December 2020): 108330. Elsevier B.V. doi:10.1016/j.agrformet.2021.108330.

Kelly, J., Kljun, N., Olsson, P.O., Mihai, L., Liljeblad, B., Weslien, P., Klemedtsson, L., and Eklundh, L. 2019. Challenges and best practices for deriving temperature data from an uncalibrated UAV thermal infrared camera. Remote Sensing, **11**(5). doi:10.3390/rs11050567.

Kim, J., Guo, Q., Baldocchi, D.D., Leclerc, M.Y., Xu, L., and Schmid, H.P. 2006. Upscaling fluxes from tower to landscape: Overlaying flux footprints on high-resolution (IKONOS) images of vegetation cover. Agricultural and Forest Meteorology, **136**(3-4): 132-146. doi:10.1016/j.agrformet.2004.11.015.

Kirby, S., Dobosy, R., Williamson, D., and Dumas, E. 2008. An aircraft-based data analysis method for discerning individual fluxes in a heterogeneous agricultural landscape.

Agricultural and Forest Meteorology, **148**(3): 481-489. doi:10.1016/j.agrformet.2007.10.011.

Klaassen, W., Van Breugel, P.B., Moors, E.J., and Nieveen, J.P. 2002. Increased heat fluxes near a forest edge. Theoretical and Applied Climatology, **72**(3-4): 231-243. doi:10.1007/s00704-002-0682-8.

Kljun, N., Calanca, P., Rotach, M.W., and Schmid, H.P. 2004a. A simple parameterisation for flux footprint predictions. Boundary-Layer Meteorology, **112**(3): 503-523. doi:10.1023/B:BOUN.0000030653.71031.96.

Kljun, N., Calanca, P., Rotach, M.W., and Schmid, H.P. 2015. A simple two-dimensional parameterisation for Flux Footprint Prediction (FFP). Geoscientific Model Development, **8**(11): 3695-3713. doi:10.5194/gmd-8-3695-2015.

Kljun, N., Kastner-Klein, P., Fedorovich, E., and Rotach, M.W. 2004b. Evaluation of Lagrangian footprint model using data from wind tunnel convective boundary layer. Agricultural and Forest Meteorology, **127**(3-4): 189-201. doi:10.1016/j.agrformet.2004.07.013.

Kljun, N., Rotach, M.W., and Schmid, H.P. 2002. A three-dimensional backward Lagrangian footprint model for a wide range of boundary-layer stratifications. Boundary-Layer Meteorology, **103**(2): 205-226. doi:10.1023/A:1014556300021.

Korhonen, L., Korpela, I., Heiskanen, J., and Maltamo, M. 2011. Airborne discrete-return LIDAR data in the estimation of vertical canopy cover, angular canopy closure and leaf area index. Remote Sensing of Environment, **115**(4): 1065-1080. Elsevier Inc. doi:10.1016/j.rse.2010.12.011.

Kustas, W., and Anderson, M. 2009. Advances in thermal infrared remote sensing for land surface modeling. Agricultural and Forest Meteorology, **149**(12): 2071-2081. doi:10.1016/j.agrformet.2009.05.016.

Kustas, W.P., Anderson, M.C., Norman, J.M., and Li, F. 2007. Utility of radiometric-aerodynamic temperature relations for heat flux estimation. Boundary-Layer Meteorology, **122**(1): 167-187. doi:10.1007/s10546-006-9093-1.

Kustas, W.P., and Norman, J.M. 1999. Evaluation of soil and vegetation heat flux predictions using a simple two-source model with radiometric temperatures for partial canopy cover. Agricultural and Forest Meteorology, **94**(1): 13-29. doi:10.1016/S0168-1923(99)00005-2.

Leberl, F., Irschara, A., Pock, T., Meixner, P., Gruber, M., Scholz, S., and Wiechert, A. 2010. Point Clouds : Lidar versus 3D Vision. Photogrammetric Engineering & Remote Sensing, **76**(10):

1123-1134.

Leclerc, M.Y., Foken, T., Savage, M.J., and Göckede, M. 2014. Footprints in micrometeorology and ecology. *In* Footprints in Micrometeorology and Ecology. Springer-Verlag Berlin Heidelberg.

Levy, P., Drewer, J., Jammet, M., Leeson, S., Friborg, T., Skiba, U., and Oijen, M. van. 2020. Inference of spatial heterogeneity in surface fluxes from eddy covariance data: A case study from a subarctic mire ecosystem. Agricultural and Forest Meteorology, **280**(October 2019). Elsevier. doi:10.1016/j.agrformet.2019.107783.

Luo, S., Wang, C., Xi, X., and Pan, F. 2014. Estimating FPAR of maize canopy using airborne discrete-return LiDAR data. Optics Express, **22**(5): 5106. doi:10.1364/oe.22.005106.

Maesano, M., Khoury, S., Nakhle, F., Firrincieli, A., Gay, A., Tauro, F., and Harfouche, A. 2020. UAV-based LiDAR for high-throughput determination of plant height and above-ground biomass of the bioenergy grass arundo donax. Remote Sensing, **12**(20): 1-20. doi:10.3390/rs12203464.

Markkanen, T., Rannik, Ü., Marcolla, B., Cescatti, A., and Vesala, T. 2003. Footprints and fetches for fluxes over forest canopies with varying structure and density. Boundary-Layer Meteorology, **106**(3): 437-459. doi:10.1023/A:1021261606719.

Matsushima, D. 2005. Relations between aerodynamic parameters of heat transfer and thermal-infrared thermometry in the bulk surface formulation. Journal of the Meteorological Society of Japan, **83**(3): 373-389. doi:10.2151/jmsj.83.373.

Metzger, S., Junkermann, W., Mauder, M., Butterbach-Bahl, K., Trancón Y Widemann, B., Neidl, F., Schäfer, K., Wieneke, S., Zheng, X.H., Schmid, H.P., and Foken, T. 2013. Spatially explicit regionalization of airborne flux measurements using environmental response functions. Biogeosciences, **10**(4): 2193-2217. doi:10.5194/bg-10-2193-2013.

Moncrieff, J., Clement, R., Finnigan, J., and Meyers, T. 2004. Averaging, Detrending, and Filtering of Eddy Covariance Time Series. *In* Handbook of Micrometeorology: A Guide for Surface Flux Measurement and Analysis. *Edited by* X. Lee, W. Massman, and B. Law. Springer Netherlands, Dordrecht. pp. 7-31.

Moncrieff, J.B., Massheder, J.M., De Bruin, H., Elbers, J., Friborg, T., Heusinkveld, B., Kabat, P., Scott, S., Soegaard, H., and Verhoef, A. 1997. A system to measure surface fluxes of momentum, sensible heat, water vapour and carbon dioxide. Journal of Hydrology, **188-**

189(1-4): 589-611. doi:10.1016/S0022-1694(96)03194-0.

Moran, M.S. 1990. A satellite-based approach for evaluation of the spatial distribution of evapotranspiration from agricultural lands. University of Arizona, Tucson, USA.

Nassar, A., Torres-rua, A., Hipps, L., Kustas, W., Mckee, M., Stevens, D., Nieto, H., Keller, D., Gowing, I., and Coopmans, C. 2022. Using Remote Sensing to Estimate Scales of Spatial Heterogeneity to Analyze Evapotranspiration Modeling in a Natural Ecosystem. Remote Sensing, **14**(2): 372. doi:https://doi.org/ 10.3390/rs14020372.

Nassar, A., Torres-rua, A., Kustas, W., Alfieri, J., Hipps, L., Prueger, J., Nieto, H., Alsina, M.M., White, W., McKee, L., Coopmans, C., Sanchez, L., and Dokoozlian, N. 2021. Assessing daily evapotranspiration methodologies from one-time-of-day suas and ec information in the grapex project. Remote Sensing, **13**(15). doi:10.3390/rs13152887.

Nie, S., Wang, C., Dong, P., Xi, X., Luo, S., and Zhou, H. 2016. Estimating Leaf Area Index of Maize Using Airborne Discrete-Return LiDAR Data. IEEE Journal of Selected Topics in Applied Earth Observations and Remote Sensing, **9**(7): 3259-3266. IEEE. doi:10.1109/JSTARS.2016.2554619.

Nieto, H., Kustas, W.P., Torres-Rúa, A., Alfieri, J.G., Gao, F., Anderson, M.C., White, W.A., Song, L., Alsina, M. del M., Prueger, J.H., McKee, M., Elarab, M., and McKee, L.G. 2019. Evaluation of TSEB turbulent fluxes using different methods for the retrieval of soil and canopy component temperatures from UAV thermal and multispectral imagery. Irrigation Science, **37**(3): 389-406. Springer Berlin Heidelberg. doi:10.1007/s00271-018-0585-9.

Nilson, T. 1971. A theoretical analysis of the frequency of gaps in plant stands. Agricultural Meteorology, **8**(C): 25-38. doi:10.1016/0002-1571(71)90092-6.

Niu, H., Hollenbeck, D., Zhao, T., Wang, D., and Chen, Y. 2020. Evapotranspiration estimation with small uavs in precision agriculture. Sensors (Switzerland), **20**(22): 1-28. doi:10.3390/s20226427.

Nocco, M.A., Zipper, S.C., Booth, E.G., Cummings, C.R., Loheide, S.P., and Kucharik, C.J. 2019. Combining evapotranspiration and soil apparent electrical conductivity mapping to identify potential precision irrigation benefits. Remote Sensing, **11**(21). doi:10.3390/rs11212460.

Norman, J.M., and Becker, F. 1995. Terminology in thermal infrared remote sensing of natural surfaces. Agricultural and Forest Meteorology, **77**(3-4): 153-166. doi:10.1016/0168-1923(95)02259-Z.

Norman, J.M., Kustas, W.P., and Humes, K.S. 1995. Source approach for estimating soil and vegetation energy fluxes in observations of directional radiometric surface temperature. Agricultural and Forest Meteorology, **77**(3-4): 263-293. doi:10.1016/0168-1923(95)02265-Y.

Ohana-Levi, N., Knipper, K., Kustas, W.P., Anderson, M.C., Netzer, Y., Gao, F., Alsina, M. del M., Sanchez, L.A., and Karnieli, A. 2020. Using satellite thermal-based evapotranspiration time series for defining management zones and spatial association to local attributes in a Vineyard. Remote Sensing, **12**(15). doi:10.3390/RS12152436.

Park, S., Ryu, D., Fuentes, S., Chung, H., O'Connell, M., and Kim, J. 2021. Mapping very-high-resolution evapotranspiration from unmanned aerial vehicle (UAV) imagery. ISPRS International Journal of Geo-Information, **10**(4). doi:10.3390/ijgi10040211.

Paul, G., Gowda, P.H., Vara Prasad, P. V., Howell, T.A., Aiken, R.M., and Neale, C.M.U. 2014. Investigating the influence of roughness length for heat transport (zoh) on the performance of SEBAL in semi-arid irrigated and dryland agricultural systems. Journal of Hydrology, **509**: 231-244. Elsevier B.V. doi:10.1016/j.jhydrol.2013.11.040.

Peng, W. 2015. A method for the quantification of spatial fluxes and associated uncertainty over heterogeneous agricultural landscape. University of Alabama.

Raupach, M.R. 1994. Simplified expressions for vegetation roughness length and zero-plane displacement as functions of canopy height and area index. Boundary-Layer Meteorology, **71**(1-2): 211-216. doi:10.1007/BF00709229.

Reuss-Schmidt, K., Levy, P., Oechel, W., Tweedie, C., Wilson, C., and Zona, D. 2019. Understanding spatial variability of methane fluxes in Arctic wetlands through footprint modelling. Environmental Research Letters, **14**(12). IOP Publishing. doi:10.1088/1748-9326/ab4d32.

Richardson, J.J., Moskal, L.M., and Kim, S.H. 2009. Modeling approaches to estimate effective leaf area index from aerial discrete-return LIDAR. Agricultural and Forest Meteorology, **149**(6-7): 1152-1160. doi:10.1016/j.agrformet.2009.02.007.

Roussel, J.-R., and Auty, D. 2021. lidR: Airborne LiDAR Data Manipulation and Visualization for Forestry Applications.

Sagan, V., Maimaitijiang, M., Sidike, P., Eblimit, K., Peterson, K.T., Hartling, S., Esposito, F., Khanal, K., Newcomb, M., Pauli, D., Ward, R., Fritschi, F., Shakoor, N., and Mockler, T. 2019. UAV-based high resolution thermal imaging for vegetation monitoring, and plant phenotyping

using ICI 8640 P, FLIR Vue Pro R 640, and thermomap cameras. Remote Sensing, **11**(3). doi:10.3390/rs11030330.

Santanello, J.A., and Friedl, M.A. 2003. Diurnal covariation in soil heat flux and net radiation. Journal of Applied Meteorology, **42**(6): 851-862. doi:10.1175/1520-0450(2003)042<0851:DCISHF>2.0.CO;2.

Schmid, H.P. 1997. Experimental design for flux measurements: Matching scales of observations and fluxes. Agricultural and Forest Meteorology, **87**(2-3): 179-200. doi:10.1016/S0168-1923(97)00011-7.

Schmid, H.P. 2002. Footprint modeling for vegetation atmosphere exchange studies: A review and perspective. Agricultural and Forest Meteorology, **113**(1-4): 159-183. doi:10.1016/S0168-1923(02)00107-7.

Solberg, S., Næsset, E., Hanssen, K.H., and Christiansen, E. 2006. Mapping defoliation during a severe insect attack on Scots pine using airborne laser scanning. Remote Sensing of Environment, **102**(3-4): 364-376. doi:10.1016/j.rse.2006.03.001.

Song, L., Kustas, W.P., Liu, S., Colaizzi, P.D., Nieto, H., Xu, Z., Ma, Y., Li, M., Xu, T., Agam, N., Tolk, J.A., and Evett, S.R. 2016a. Applications of a thermal-based two-source energy balance model using Priestley-Taylor approach for surface temperature partitioning under advective conditions. Journal of Hydrology, **540**: 574-587. Elsevier B.V. doi:10.1016/j.jhydrol.2016.06.034.

Song, L., Liu, S., Kustas, W.P., Zhou, J., Xu, Z., Xia, T., and Li, M. 2016b. Application of remote sensing-based two-source energy balance model for mapping field surface fluxes with composite and component surface temperatures. Agricultural and Forest Meteorology, **230-231**: 8-19. Elsevier B.V. doi:10.1016/j.agrformet.2016.01.005.

Song, Y., Wang, J., and Shang, J. 2020. Estimating effective leaf area index of winter wheat using simulated observation on unmanned aerial vehicle-based point cloud data. IEEE Journal of Selected Topics in Applied Earth Observations and Remote Sensing, **13**: 2874-2887. doi:10.1109/JSTARS.2020.2995577.

Su, Z., Schmugge, T., Kustas, W.P., and Massman, W.J. 2001. An evaluation of two models for estimation of the roughness height for heat transfer between the land surface and the atmosphere. Journal of Applied Meteorology, **40**(11): 1933-1951. doi:10.1175/1520-0450(2001)040<1933:AEOTMF>2.0.CO;2.

Sutherland, G., Chasmer, L.E., Kljun, N., Devito, K.J., and Petrone, R.M. 2017. Using High Resolution LiDAR Data and a Flux Footprint Parameterization to Scale Evapotranspiration Estimates to Lower Pixel Resolutions. Canadian Journal of Remote Sensing, **43**(2): 215-229. Taylor & Francis. doi:10.1080/07038992.2017.1291338.

Sutherland, G., Chasmer, L.E., Petrone, R.M., Kljun, N., and Devito, K.J. 2014. Evaluating the use of spatially varying versus bulk average 3D vegetation structural inputs to modelled evapotranspiration within heterogeneous land cover types. Ecohydrology, **7**(6): 1545-1559. doi:10.1002/eco.1477.

Taylor, J.A., and Bates, T.R. 2013. A discussion on the significance associated with Pearson's correlation in precision agriculture studies. Precision Agriculture, **14**(5): 558-564. doi:10.1007/s11119-013-9314-9.

Torres-Rua, A. 2017. Vicarious calibration of sUAS microbolometer temperature imagery for estimation of radiometric land surface temperature. Sensors (Switzerland), **17**(7): 5-9. doi:10.3390/s17071499.

Troufleau, D., Lhomme, J.P., Monteny, B., and Vidal, A. 1997. Sensible heat flux and radiometric surface temperature over space Sahelian vegetation. I. An experimental analysis of the kB-1 parameter. Journal of Hydrology, **188-189**(1-4): 815-838. doi:10.1016/S0022-1694(96)03172-1.

Tuovinen, J.P., Aurela, M., Hatakka, J., Räsänen, A., Virtanen, T., Mikola, J., Ivakhov, V., Kondratyev, V., and Laurila, T. 2019. Interpreting eddy covariance data from heterogeneous Siberian tundra: Land-cover-specific methane fluxes and spatial representativeness. Biogeosciences, **16**(2): 255-274. doi:10.5194/bg-16-255-2019.

Twine, T.E., Kustas, W.P., Norman, J.M., Cook, D.R., Houser, P.R., Meyers, T.P., Prueger, J.H., Starks, P.J., and Wesely, M.L. 2000. Correcting eddy-covariance flux underestimates over a grassland. Agricultural and Forest Meteorology, **103**(3): 279-300. doi:10.1016/S0168-1923(00)00123-4.

Vallejos, R., Osorio, F., and Bevilacqua, M. 2020. Spatial Relationships Between Two Georeferenced Variables: with Applications in R. Springer, New York.

Vesala, T., Kljun, N., Rannik, Ü., Rinne, J., Sogachev, A., Markkanen, T., Sabelfeld, K., Foken, T., and Leclerc, M.Y. 2008. Flux and concentration footprint modelling: State of the art. Environmental Pollution, **152**(3): 653-666. doi:10.1016/j.envpol.2007.06.070.

Wagle, P., Gowda, P.H., Neel, J.P.S., Northup, B.K., and Zhou, Y. 2020. Integrating eddy fluxes and remote sensing products in a rotational grazing native tallgrass prairie pasture. Science of the Total Environment, **712**: 136407. Elsevier B.V. doi:10.1016/j.scitotenv.2019.136407.

Webb, E.K., Pearman, G.I., and Leuning, R. 1980. Correction of flux measurements for density effects due to heat and water vapor transfer. Q.J.R. Meteorol. Soc., **106**(447): 85-100.

Widyaningrum, E., Sensing, R., Faculty, G., Agency, G.I., Photos, A., Matching, S.G., and Analyses, C. 2017. Comprehensive comparison of two image-based point clouds from aerial photos with airborne LiDAR for large-scale mapping. The International Archives of Photogrammetry, Remote Sensing and Spatial Information Sciences, **XLII**(September): 18-22.

Wizemann, H.D., Ingwersen, J., Högy, P., Warrach-Sagi, K., Streck, T., and Wulfmeyer, V. 2014. Three year observations of water vapor and energy fluxes over agricultural crops in two regional climates of Southwest Germany. Meteorologische Zeitschrift, **24**(1): 39-59. doi:10.1127/metz/2014/0618.

Xia, T., Kustas, W.P., Anderson, M.C., Alfieri, J.G., Gao, F., McKee, L., Prueger, J.H., Geli, H.M.E., Neale, C.M.U., Sanchez, L., Alsina, M.M., and Wang, Z. 2016. Mapping evapotranspiration with high-resolution aircraft imagery over vineyards using one-and two-source modeling schemes. Hydrology and Earth System Sciences, **20**(4): 1523-1545. doi:10.5194/hess-20-1523-2016.

Xu, F., Wang, W., Wang, J., Xu, Z., Qi, Y., and Wu, Y. 2017. Area-Averaged evapotranspiration over a heterogeneous land surface: Aggregation of multi-point EC flux measurements with a high-resolution land-cover map and footprint analysis. Hydrology and Earth System Sciences, **21**(8): 4037-4051. doi:10.5194/hess-21-4037-2017.

Zipper, S.C., and Loheide II, S.P. 2014. Using evapotranspiration to assess drought sensitivity on a subfield scale with HRMET, a high resolution surface energy balance model. Agricultural and Forest Meteorology, **197**: 91-102. Elsevier B.V. doi:10.1016/j.agrformet.2014.06.009.

Zipper, S.C., and Loheide, S.P. 2014. Using evapotranspiration to assess drought sensitivity on a subfield scale with HRMET, a high resolution surface energy balance model. Agricultural and Forest Meteorology, **197**: 91-102. Elsevier B.V. doi:10.1016/j.agrformet.2014.06.009.

APPENDIX A

A1. Flight logs

Flight logs

Date	Site	Time (CST) [hh:mm:ss]	Flight duration	Sensor	Height $[masl]$	Cloud cover [%]	T $[°C]$	Wind speed $[km \cdot hr^{-1}]$	Wind direction $[° \circlearrowright N]$
2018/07/26	B	11:37:35	00:11:21	L	-	-	-	-	-
2018/07/26	B	12:00:00	00:16:16	T	-	-	-	-	-
2019/06/13	B	10:07:59	00:16:48	L	100	75	22	12.43	178
2019/06/13	B	10:28:34	00:16:49	L	100	75	22	12.13	179
2019/06/13	B	11:40:53	00:15:15	T	-	-	-	-	-
2019/06/13	B	14:06:43	00:43:31	D	95	97	27	7.82	79
2019/06/26	B	09:33:44	00:18:29	L	101	19	16	7.67	258
2019/06/26	B	11:18:44	00:23:05	T	118	44	22	10.53	277
2019/06/26	F	12:24:59	00:22:11	T	120	33	23	8.16	280
2019/06/26	F	12:54:39	00:15:36	L	104	75	20	14.18	247
2019/06/26	F	13:13:57	00:15:24	L	104	75	21	14.14	256
2019/06/26	F	14:18:01	00:26:54	T	97	71	21	12.44	293
2019/06/26	B	15:21:53	00:29:32	T	95	44	21	12.45	279
2019/06/26	B	09:30:00	00:30:00	D	-	-	-	-	-
2019/07/03	B	08:02:47	00:18:42	L	101	75	13	9.16	311
2019/07/03	B	07:23:26	00:32:47	D	98	75	12	11.94	300
2019/07/03	F	08:46:00	00:27:42	D	98	75	14	9.31	302
2019/07/03	F	09:17:41	00:15:25	L	103	75	15	10.04	297
2019/07/03	F	09:37:58	00:15:21	L	104	75	15	10.78	296
2019/07/03	F	11:18:51	00:29:31	D	97	75	17	19.03	289
2019/07/03	B	12:21:13	00:36:16	D	99	75	18	18.48	276
2019/07/03	B	13:56:24	00:36:24	D	97	75	18	20.19	234
2019/07/03	F	15:25:53	00:23:17	D	98	86	14	16.11	340
2019/07/31	B	10:12:34	00:18:49	L	101	39	20	16.54	330
2019/07/31	B	10:35:58	00:39:05	D	97	29	21	14.8	334
2019/07/31	F	12:11:58	00:16:12	L	103	19	22	13.68	330
2019/07/31	B	12:11:58	00:16:12	L	103	19	22	13.68	330
2019/07/31	F	12:32:34	00:16:56	L	104	19	22	12.39	331
2019/07/31	F	12:56:06	00:32:11	D	98	19	23	10.9	332
2019/07/31	B	14:20:30	00:39:59	D	97	27	23	11.63	335
2019/08/30	F	14:57:38	00:15:31	L	104	100	17	11.28	135
2019/08/30	F	15:17:57	00:11:51	L	103	100	17	11.36	138
2019/08/30	F	14:30:00	00:30:00	D	-	-	-	-	-
2020/07/28	B	12:00:00	00:30:00	D	-	-	-	-	-
2020/07/28	F	13:15:00	00:30:00	D	-	-	-	-	-

A2. Soil texture analysis for Barley

University of Saskatchewan
Geotechnical Laboratory

Grain Size Analysis - ASTM D422			
Date:	03-Jan-20		Operator:
Client:			AH
Sample ID:	Barley 0-20 cm		Checked By:
Project:	AWF		
Soil Description:	Sandy loam		
Dispersion Device:	Sodium Hexametaphosphate		

Soil Fraction (%)	Gravel	Coarse Sand	Medium Sand	Fine Sand	Silt	Clay
	> 4.75 mm	2 to 4.75 mm	0.425 to 2 mm	0.075 to 0.425 mm	0.005 to 0.075 mm	<0.005 mm
	0.0	0.1	0.5	78.2	15.7	5.5

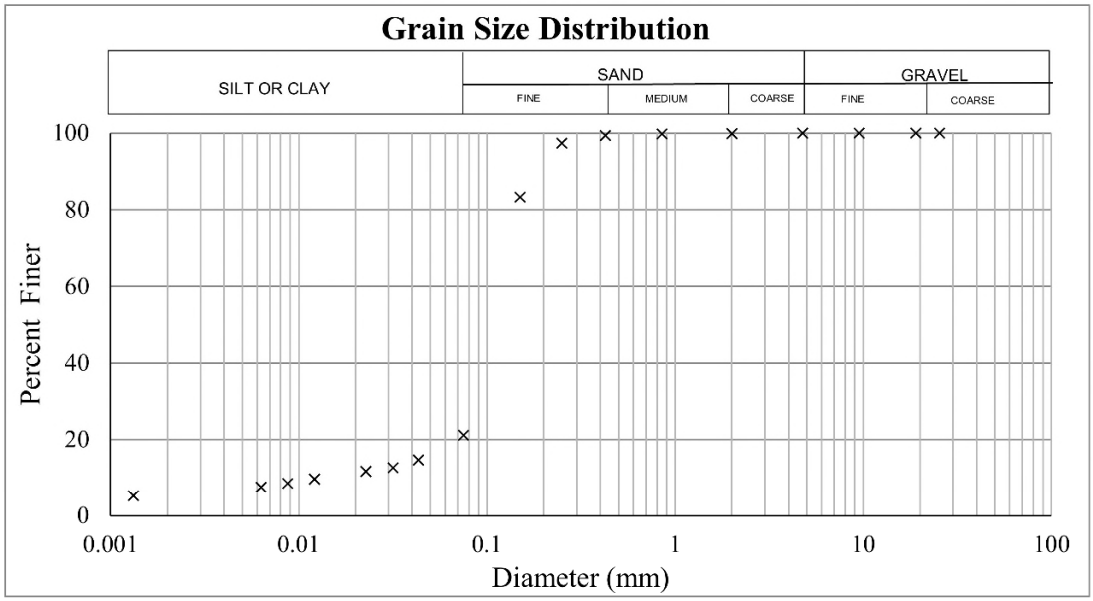

Notes:

Raw specimen seived to isolate 50 g fines for hydrometer. Remaining portion soaked in calgon solution and washed through 75 micron seive. This step was repeated until aggregates were broken and majority of fines washed out. Washed sample was oven dried and put through standard seive set. Large fractions were split into two or more seive stacks to circumvent overloading. The trace amount of organics and litter were left in the sample (most volatilized in oven before weighing).

A3. Soil texture analysis for Forage

University of Saskatchewan
Geotechnical Laboratory

Grain Size Analysis - ASTM D422			
Date:	03-Jan-20		Operator:
Client:			AH
Sample ID:	Forage 0-20 cm		Checked By:
Project:	AWF		

Soil Description:	Sandy-loam
Dispersion Device:	Sodium Hexametaphosphate

Soil Fraction (%)	Gravel	Coarse Sand	Medium Sand	Fine Sand	Silt	Clay
	> 4.75 mm	2 to 4.75 mm	0.425 to 2 mm	0.075 to 0.425 mm	0.005 to 0.075 mm	<0.005 mm
	0.0	0.0	0.8	73.2	19.0	7.0

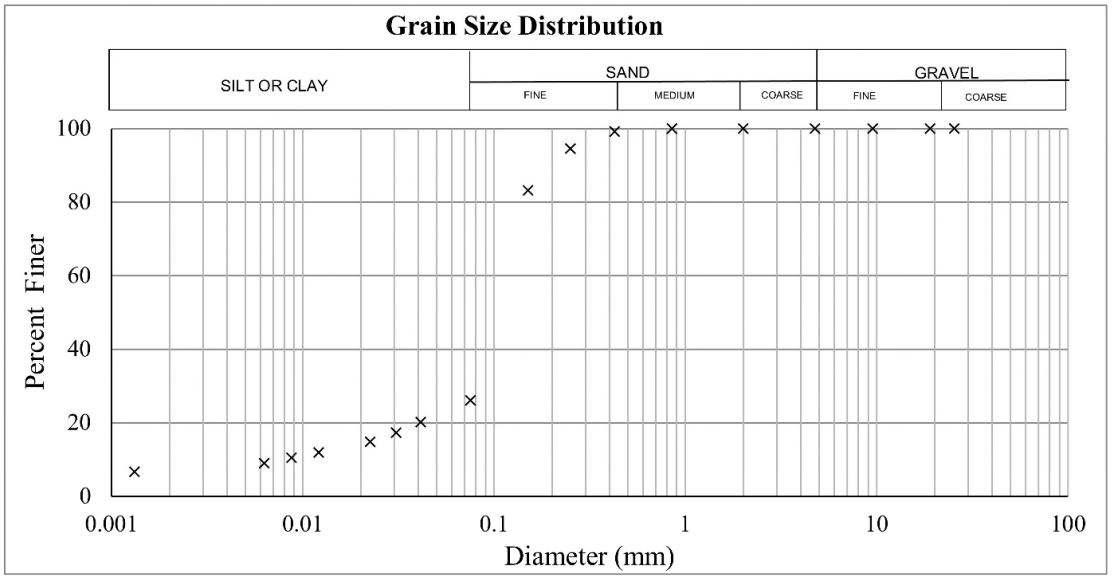

Notes:

Raw specimen seived to isolate 50 g fines for hydrometer. Remaining portion soaked in calgon solution and washed through 75 micron seive. This step was repeated until aggregates were broken and majority of fines washed out. Washed sample was oven dried and put through standard seive set. Large fractions were split into two or more seive stacks to circumvent overloading. The trace amount of organics and litter were left in the sample (most volatilized in oven before weighing).

A4. Thermal camera specifications

Thermal camera specifications

Platform	Handheld	Ebee+ (ThermoMAP)	EbeeX (Duet)
Measurement	Thermal	Thermal	Thermal
Sensor	FLIR T650sc	FLIR Vue Pro	FLIR Vue Pro R
Focal Length	24.6	9 mm	13 mm
Image Size	640 X 580	640 X 512	640 X 512
Spectral range	750-1300 nm	750-1350 nm	750-1350 nm
Central Wavelength	1029	1079 nm	1029 nm
Reported Accuracy	$\pm$ 1 $°C$	$\pm$ 5 $°C$	$\pm$ 5 $°C$
Sensitivity	0.2 $°C$	-	0.04 $°C$

A5. Meteorological summary

Meteorology summary

Image	Outgoing longwave radiation	Incoming shortwave radiation	Air temperature at ~3 $\boldsymbol{magl}$	Surface brightness temperature	Vapour pressure deficit	Wind speed at 3 $\boldsymbol{magl}$	Friction velocity	Relative humidity at 3 $\boldsymbol{magl}$
[yy_ddd_sensor_#]	$[W\ m^{-2}]$	$[W\ m^{-2}]$	$[°C]$	$[°C]$	$[Pa]$	$[m\ s^{-1}]$	$[m\ s^{-1}]$	[%]
18_207_e_1	286	-5	21	24	1592	1.4	0.24	46
19_177_e_1	776	18	18	26	1035	2.2	0.17	62
19_177_e_4	660	18	21	27	1538	2.9	0.29	48
19_177_h_1	850	26	21	29	1690	3.0	0.20	45
19_184_h_1	155	0	12	13	231	2.2	0.18	80
19_184_h_4	973	21	18	24	1251	3.1	0.27	53
19_184_h_5	258	3	17	18	808	2.7	0.30	57
19_212_h_1	631	-9	20	23	1039	2.5	0.34	71
19_212_h_3	818	8	25	29	2062	2.8	0.39	47
19_242_h_1	569	23	17	25	926	2.1	0.23	55
20_210_h_1	726	10	27	30	2220	3.4	0.38	37
19_177_e_2	809	20	20	26	1186	2.5	0.29	54
19_177_e_3	642	13	21	25	1416	2.5	0.31	49
19_184_h_2	521	4	15	17	714	2.3	0.31	66
19_184_h_3	630	10	17	21	1168	2.6	0.37	54
19_184_h_6	434	4	18	19	991	2.0	0.23	58
19_212_h_2	851	19	24	30	1973	2.3	0.33	53
19_242_h_2	149	5	16	18	1003	1.6	0.19	62
20_210_h_2	874	70	30	46	3253	3.6	0.37	29

A6. Sigmoidal gap filling

The f_c gap filling process used equation $[\alpha]$ to fit the f_c data to canopy height. The three coefficients a, b and c represent the upper asymptote, quickness of change, and max q threshold respectively. Since f_c varies from $0-1$, we set the upper asymptote $a=1$. The LAI_e gap filling process used equation $[\alpha]$ also to fit the LAI_e data to canopy height (x is a placeholder for f_c or LAI_e). The three coefficients a, b and c represent the upper asymptote, quickness of change, and max q threshold respectively.

$[\alpha]$ $$x = \frac{a}{1+e^{-b(q-c)}}$$

Canopy gap filling sigmoidal fit

Site	ID	b	c	$\boldsymbol{RMSE}$	Mean bias	$\boldsymbol{R^2_{adj}}$
CLBA	18_207	11.49	0.26	0.41	0.4	0.61
CLBA	19_184	14.02	0.26	0.02	0	0.48
CLBA	19_177	12.50	0.26	0.06	0.05	0.64
CLBA	19_212	8.30	0.28	0.35	0.34	0.53
CLBA	20_210	8.45	0.34	0.29	0.28	0.43

LAI gap filling sigmoidal fit

Site	ID	a	b	c	$\boldsymbol{RMSE}$	Mean bias	$\boldsymbol{R^2_{adj}}$
CLBA	18_207	3.11	17.24	0.33	1.96	1.83	0.54
CLBA	19_184	1.25	19.57	0.18	0.31	0.28	0.67
CLBA	19_177	0.64	26.77	0.13	0.14	0.12	0.57
CLBA	19_212	4.61	12.79	0.40	2.98	2.85	0.52
CLBA	20_210	5.65	15.73	0.44	4.66	4.51	0.26

A7. Modified t-test of trial temperatures and ET_R

Modified t-test of trial temperatures and ET_R

Image	$T_{B,obs}$ comparison	Temperature		ET_R	
		n_{mod}*	r (p<0.01)	n_{mod}*	r (p<0.01)
18_207_e_1	$T_{R,obs}$	86	.986	81	.966
19_177_e_1	$T_{R,obs}$	34	.991	55	.941
19_177_e_4	$T_{R,obs}$	30	.996	50	.957
19_177_e_4	T_B	31	.998	37	.960
19_177_e_4	T_R	31	.997	36	.948
19_177_h_1	$T_{R,obs}$	17	.99	23	.933
19_184_h_1	$T_{R,obs}$	26	.916	39	.959
19_184_h_4	$T_{R,obs}$	71	.996	97	.995
19_184_h_5	$T_{R,obs}$	198	.989	266	.953
19_212_h_1	$T_{R,obs}$	506	.988	484	.997
19_212_h_3	$T_{R,obs}$	478	.992	506	.997
19_212_h_3	T_B	466	.997	484	.997
19_212_h_3	T_R	474	.994	477	.996
20_210_h_1	$T_{R,obs}$	188	.993	190	.998
20_210_h_1	T_B	182	.999	183	.998
20_210_h_1	T_R	186	.997	182	.996
19_177_e_2	$T_{R,obs}$	87	.990	72	.995
19_177_e_3	$T_{R,obs}$	170	.989	105	.994
19_184_h_2	$T_{R,obs}$	20	.981	39	.992
19_184_h_3	$T_{R,obs}$	32	.993	41	.986
19_184_h_6	$T_{R,obs}$	33	.991	39	.986
19_212_h_2	$T_{R,obs}$	45	.998	40	.999
19_242_h_2	$T_{R,obs}$	45	.936	57	.955
20_210_h_2	$T_{R,obs}$	36	.997	47	.997

* effective number of observations reduced from a 10000 random subsample of each raster

APPENDIX B

B1. Piece-wise linear regression fitting

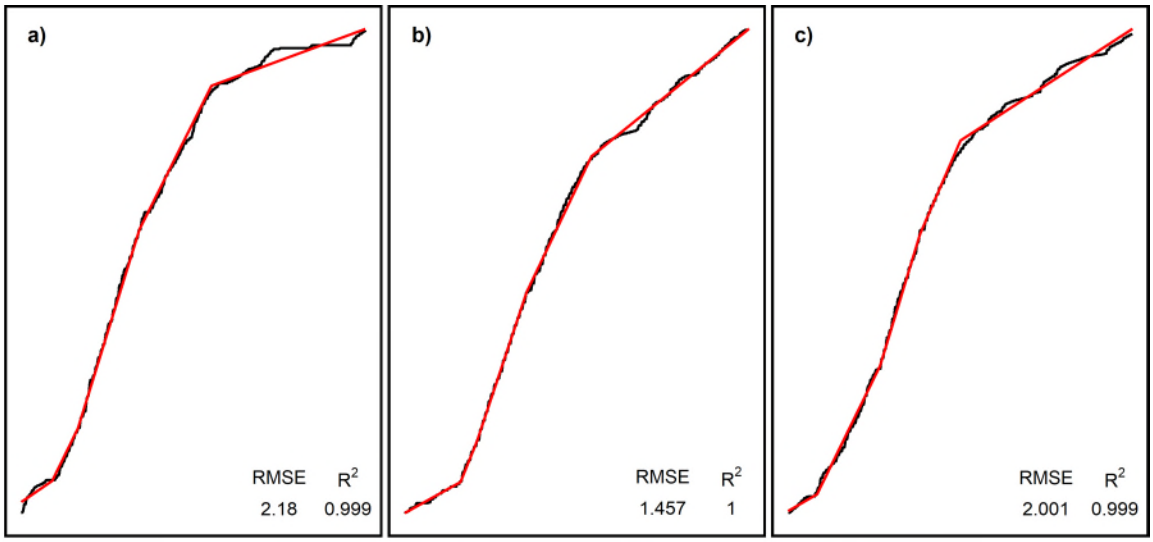

Piece-wise linear regression fitting
a) 2018, b) 2019, and c) 2020

B2. ET period information

ET Period Information

Year	Period	Phenology	Start (CST) [yyyy-MM-dd]	End (CST) [yyyy-MM-dd]	ET_rate [$mm\ d^{-1}$]	GDD (start) [$°C\ d$]	GDD (end) [$°C\ d$]
2018	Pre	Germination - Tillering	2018-06-01	2018-06-12	1.5	10*	206
	Early	Tillering - Stem Elongation	2018-06-12	2018-06-22	2.8	206	395
	Mid	Stem Elongation - Heading	2018-06-22	2018-07-15	4.5	395	804
	Late	Heading - Harvested	2018-07-15	2018-08-10	2.7	804	1319
	Post	Harvested	2018-08-10	2018-09-30	0.6	1319	1506
2019	Pre	Germination - Tillering	2019-06-03	2019-06-23	0.7	26*	322
	Early	Tillering - Stem Elongation	2019-06-23	2019-06-28	3.2	322	424
	Mid	Stem Elongation - Booting	2019-06-28	2019-07-15	3.8	424	721
	Late	Booting - Fruit Development	2019-07-15	2019-08-07	2.6	721	1146
	Post	Fruit Development - Harvested	2019-08-07	2019-09-30	1.1	1146	1865
2020	Pre	Germination - Leaf Development	2020-05-29	2020-06-08	1.0	11*	161
	Early	Leaf Development - Stem Elongation	2020-06-08	2020-07-01	2.6	161	532
	Mid	Stem Elongation - Booting	2020-07-01	2020-07-15	4.6	532	778
	Late	Booting - Fruit Development	2020-07-15	2020-07-30	2.6	778	1077
	Post	Fruit Development - Harvested	2020-07-30	2020-09-30	0.9	1077	1507

* Weather station installed after seeding. Growing Degree Days prior to seeding estimated from a nearby weather station

B3. ET period information

ET Period Information

Image [$yy\_DDD\_p\_\#$]*	Date	Start overlap CST [$hh{:}\,mm{:}\,ss$]	End overlap CST [$hh{:}\,mm{:}\,ss$]	Solar zenith ∠ [°]	ET spatial mean (μ_{ET}) [$W\ m^{-2}$]	ET spatial standard deviation (σ_{ET}) [$W\ m^{-2}$]	ET coefficient of variation (cv_{ET}) [-]
18_207_e_1	July 26, 2018	13:03:00	13:10:00	32.7	0.03	0.31	0.10
19_177_e_1	June 26, 2019	11:24:00	11:33:00	34.9	0.02	0.51	0.04
19_177_h_1	June 26, 2019	15:09:00	15:20:00	38.1	0.02	0.56	0.03
19_177_e_4	June 26, 2019	15:30:00	15:40:00	39.3	0.04	0.54	0.07
19_184_h_1	July 3, 2019	7:41:00	7:54:00	67.4	0.01	0.11	0.13
19_184_h_4	July 3, 2019	12:41:00	12:45:00	29.6	0.13	0.57	0.23
19_184_h_5	July 3, 2019	14:14:00	14:23:00	31.6	0.04	0.09	0.43
19_212_h_1	July 31, 2019	10:48:00	11:00:00	44.0	0.06	0.64	0.09
19_212_h_3	July 31, 2019	14:37:00	14:47:00	37.7	0.09	0.81	0.11
20_210_h_1	July 28, 2020	11:20:00	11:34:00	39.8	0.08	0.76	0.10